Modeling of Carrier Dynamics in Electroabsorption Modulators

Højfeldt, Sune

Publication date:
2002

Document Version
Publisher's PDF, also known as Version of record

Ph.D. thesis

Modeling of carrier dynamics in electroabsorption modulators

Sune Højfeldt

COM
Technical University of Denmark

May 2002

Abstract

This thesis is concerned with modeling of electroabsorption modulators. Electroabsorption modulators are expected to play an important role both in the coming 40-Gbit/s optical communication systems and in next-generation, all-optical communication systems. Understanding the dynamics in electroabsorption modulators will help to support the development of high-speed components tailored for specific functionalities.

We present modeling of all-optical functionalities realized with electroabsorption modulators. Using a model that includes propagation equations, a detailed gain model, and a phenomenological model for the carrier sweep-out dynamics, we investigate all-optical wavelength conversion, all-optical signal regeneration, and all-optical demultiplexing.

A detailed drift-diffusion type model for the sweep-out of photo-excited carriers in electroabsorption modulators is presented. We use the model to calculate absorption spectra and steady-state carrier distributions in different modulator structures. This allows us to investigate a number of important properties of electroabsorption modulators, such as the electroabsorption effect and the saturation properties. We also investigate the influence that carrier recapture has on the device properties, and we discuss the recapture process on a more fundamental level.

The model is also used to investigate in detail the carrier sweep-out process in electroabsorption modulators. We investigate how the intrinsic-region width, the separate-confinement heterobarrier design, the optical power level, the number of wells, and other important design- and external parameters affect the dynamical properties. We characterize the field change across the wells in a multi-quantum-well structure, and we investigate the sweep-out in a structure with shallow wells. Sweep-out upon excitation with highly energetic pulses is investigated, and the influence of carrier recapture on the sweep-out process is modeled and discussed.

From our results we draw a number of conclusions concerning the carrier sweep-out dynamics in electroabsorption modulators, and about the influence that the epitaxial structure design has on the intrinsic dynamical properties.

Resumé

Denne afhandling omhandler modellering af elektroabsorptions-modulatorer. Elektroabsorptions-modulatorer forventes at spille en betydelig rolle i de kommende 40 Gbit/s optiske kommunikations-systemer og i fremtidens rent-optiske kommunikations-systemer. En forståelse af dynamikken i elektroabsorptions-modulatorer vil kunne understøtte udviklingen af højhastigheds-komponenter der er skræddersyede til bestemte formål.

Vi præsenterer modellering af rent-optiske funktionaliteter realiseret ved brug af elektroabsorptions-modulatorer. Ved hjælp af en model som indeholder udbredelsesligninger, en detaljeret model for forstærkning, og en fænomenologisk model for ladningsbærer-udfejning, undersøger vi rent-optisk bølgelængde-konvertering, rent-optisk signal regenerering, og rent-optisk kanal-udkobling.

Vi præsenterer en detaljeret drift-diffusion model for udfejningen af foto-eksiterede ladningsbærere i elektroabsorptions-modulatorer. Vi anvender modellen til at beregne absorptions-spektre og til at modellere ladningsbærer-fordelinger i forskellige strukturer. Beregningerne sætter os i stand til at undersøge en række vigtige egenskaber vedrørende elektroabsorptions-modulatorer, såsom elektroabsorptions-effekten og mætnings-egenskaberne. Vi undersøger også hvilken indflydelse genindfangning af ladningsbærere har på komponent-egenskaberne, og vi diskuterer genindfangningsprocessen på et mere fundamentalt niveau.

Modellen bliver også brugt til at undersøge ladningsbærer-udfejningen i elektroabsorptions-modulatorer i detaljer. Det undersøges hvordan bredden af det intrinsiske område, antallet af brønde, det optiske effekt-niveau, designet af den separate begrænsnings-struktur, og andre design- og eksterne parametre, påvirker dynamikken. Vi karakteriserer felt-ændringen henover brønd-området i en struktur med flere brønde, og vi undersøger udfejningen i en struktur med lave brønde. Udfejning efter eksitation med pulser med høj energi undersøges, og indflydelsen af genindfangning af ladningsbærere på udfejnings-processen modelleres og diskuteres.

Fra vores resultater uddrager vi en række fundamentale konklusioner vedrørende dynamikken omkring udfejning af ladningsbærere i elektroabsorptions-modulatorer, og vi finder en række sammenhænge mellem de intrinsiske dynamiske egenskaber og designet af den epitaksielle struktur.

Acknowledgments

The work presented in this thesis was carried out at Research Center COM and at Mikroelektronik Centret, Technical University of Denmark, in the Optoelectronics group headed by Jørn M. Hvam.

The work was supervised by Associate Professor Jesper Mørk and Assistant Professor Svend Bischoff. The patience of my main advisor, Jesper Mørk, has been crucial for the realization of the results. The decision to base one's research contribution on an extensive numerical model, which, as it turned out, requires the bulk part of a three-year PhD study to realize, can at times make for a quite unnerving experience. Jesper has shown no need to pester me in the long process of developing both model and code, but has instead conveyed a quiet belief that the thing would materialize. I have appreciated this many a time. The fact that Jesper always has provided the most knowledgable and meticulous input to my work and to discussions we have had about various physics issues has been equally appreciated.

I also owe many thanks to Svend Bischoff for always providing good and to-the-point input, even when he was less involved in the work.

All my colleagues at Research Center COM and at Mikroelektronik Centret are greatly appreciated for creating a pleasant and fun working environment. In particular, collaborating with friends and fellow students Francis Romstad and Leif K. Oxenløwe has been a real pleasure.

I would also like to thank my girlfriend, Lise, for putting up with me through the last many months, during which I have turned our place upside down and transformed it into a combined office and physics library.

Last but not least, I wish thank my family for their ongoing support through my many years of studying.

The work was supported by Danish Technical Research Council through the SCOOP framework.

Copenhagen, May 2002
Sune Højfeldt

Contents

List of Publications

[1] S. Højfeldt, S. Bischoff, and J. Mørk, "All-optical wavelength conversion and signal regeneration using an electroabsorption modulator," in *Tech. Dig. LEOS'99*, 1999.

[2] S. Højfeldt, S. Bischoff, and J. Mørk, "All-optical demultiplexing using an electroabsorption modulator," in *Tech. Dig. CLEO 2000*, 2000, pp. 342–3.

[3] S. Højfeldt, S. Bischoff, and J. Mørk, "All-Optical Wavelength Conversion and Signal Regeneration Using an Electroabsorption Modulator," *J. Lightwave Technol.*, vol. 18, no. 8, pp. 1121–7, 2000.

[4] Jesper Mørk, Svend Bischoff, and Sune Højfeldt, "Limits to speed of semiconductor devices for all-optical processing," in *Tech. Dig. UEO 2001*, 2001.

[5] Svend Bischoff, Sune Højfeldt, and Jesper Mørk, "Modeling of semiconductor devices for high-speed all-optical signal processing," *Trends in Optics and Photonics*, vol. 49, pp. 140–146, 2001.

[6] S. Højfeldt, S. Bischoff and J. Mørk, "Modeling of carrier transport in multi-quantum-well p-i-n modulators," *Proc. of NSM'01*, 2001.

[7] S. Højfeldt and J. Mørk, "Modeling of carrier transport in multi-quantum-well p-i-n modulators," *Subm. to Physica Scripta*, 2001.

[8] Jesper Mørk, Kresten Yvind, Leif Oxenløwe, Peter M.W. Skovgaard, Francis Romstad, Svend Bischoff, Sune Højfeldt, Andrea Tersigni, Lotte Christiansen, Abbas Nik, Filip Öhman, Jørn M. Hvam, Jesper Hanberg, Karsten Hoppe, and Martin Løbel, "SCOOP – Semiconductor COmponents for Optical signal Processing," *DOPS*, 2001.

[9] L.K. Oxenløwe, E. Hilliger, A. Tersigni, A.M. Nik, S. Højfeldt, F. Romstad, K. Yvind, P.M.W. Skovgaard, K. Hoppe, and J. Hanberg, "All-optical Demultiplexing and Wavelength Conversion in an Electroabsorption Modulator," in *Proc. ECOC'01*, Madrid, Spain, 2001, pp. 604–605.

Chapter 1

Introduction

Today, the Internet has an important place in many aspects of our lives. A means of communicating, of selling and purchasing goods, of presenting businesses and causes, of bringing people together, the Internet has changed society significantly within the last few years. The not so distant future will bring applications that are much more sophisticated than those available today. Videophoning will be as common as telephoning is today. Software applications that today run locally on people's personal computers will instead run on remote servers and be provided as services over the Internet. The future bandwidth will allow the trip to the local Blockbuster video store to be replaced by a few clicks on the mouse and a few seconds of waiting.

These are just a few examples of the possibilities that future optical communication systems will open up. Already today the speed at which new applications emerge requires a high-paced evolution of the optical communication systems around the world.

A decade ago, one fiber carried a bit-stream at one wavelength at a time. Increasing the information flow on the fiber was accomplished by increasing the bit-rate of the signal. In recent years, the information flow on fibers has been increased by using several bit-streams at different wavelengths simultaneously. Today, the conglomerate bit-rate on fibers is increased by increasing *both* the bit-rate per wavelength and the number of wavelengths.

The current development is taking the single-channel rate from 10 Gbit/s to 40 Gbit/s. This move is not a simple one. Semiconductor lasers, for instance, can be directly modulated at 10 Gbit/s, but at 40 Gbit/s, direct

modulation produces pulses that are useless for transmission. A "popular" way to produce pulses at 40 Gbit/s involves a semiconductor laser that puts out a continuous-wave signal, and an electroabsorption modulator that modulates the laser light into pulses. Typically, the light source is a distributed feedback laser (DFB), and the device is therefore often referred to as DFB-EAM. Today, basically all DFB-EAMs are monolithically integrated, that is, made out of a single physical crystal. A number of other problems arise when going from 10 Gbit/s to 40 Gbit/s. These problems must be dealt with before 40 Gbit/s systems can become a reality.

At the same time, there is little doubt that next-generation optical communication systems will make extensive use of all-optical signal processing to replace much of the electrical signal processing required in present optical communication systems. All-optical processing operates directly on the optical signal, and much of the conversion back and forth between the electrical domain and the optical domain can be bypassed. As the number of wavelengths per fiber continues to grow, all-optical signal processing will therefore become increasingly advantageous compared to electrical signal processing.

To support both the immediate move to 40 Gbit/s, but also in anticipation of the move towards optical communication systems that employ all-optical technology, a number of diverse components have been invented that can perform the functions required in such systems. Apart from the more basic components — such as lasers, amplifiers, multiplexers, and detectors, which are in use in current systems — more advanced components are emerging. These include wavelength converters, signal regenerators, add-and-drop components, and advanced routing components, among others.

Component makers are right now taking the safe way, focusing on the move to 40 Gbit/s and letting the all-optical technology mature in the research laboratories for yet some time. Hence, the move to 40 Gbit/s systems will probably happen in much the same way that systems were taken from 2.5 Gbit/s to 10 Gbit/s: The individual functionalities are performed in basically the same way that they were at the lower channel rate, but with higher-speed components. In some cases, integrated components will replace stand-alone components. As an example, the directly modulated 10 Gbit/s laser would be replaced by the DFB-EAM device that we mentioned previously. Eventually, when the 40 Gbit/s technology has matured, the integration of components into devices with large functionality will be the next step, and all-optical systems will become the next focus point for the evolution of optical communication systems.

One of the components that are expected to be important in future optical communication systems is the electroabsorption modulator. The electroabsorption modulator is based on the electroabsorption effect, described in Chapter 2. Already, lasers are integrated with electroabsorption modulators in the DFB-EAM. Electroabsorption modulators are also being widely used in the research laboratories to perform a number of all-optical functionalities of interest in relation to next-generation optical communication systems. Being very versatile and at the same time relatively simple, much effort has gone and goes into designing, fabricating, and testing such devices.

Design tools are of increasing interest to the telecom industry, and a number of design tools have emerged within the last few years, for instance for designing transmission systems. Within the components technology area, most detailed tools address the design of lasers and amplifiers. Recently, tools for designing more exotic things, such as photonic bandgap components, have also emerged. However, to our knowledge there are no commercially available tools for designing electroabsorption modulators. A design phase can eliminate some of the production cycles required to develop and sophisticate devices. The fabrication of prototype devices is typically a costly affair, and the introduction of one or more design phases into the development process can be a way of reducing development costs.

Modeling of electroabsorption modulators is the subject of the present thesis. The first part of the thesis describes modeling of the electroabsorption modulator as a functional component used to perform certain all-optical functionalities, namely wavelength conversion, signal regeneration, and demultiplexing. The modeling of these functionalities is performed using a simple model in which the modulator's absorption recovery and saturation properties are described phenomenologically.

The second part of the thesis concerns a detailed model for the carrier sweep-out dynamics in electroabsorption modulators. The model, which we have dubbed *PinSim*, describes the spatial and temporal distribution of photo-excited carriers in electroabsorption modulators, and the influence of those carriers on the device absorption. As the epitaxial structure is its only required input, the simulator can be used to design, on the epitaxial level, modulators optimized with respect to some desired property.

Chapter 2 introduces the electroabsorption modulator. The principle behind it and some of its applications in optical communication systems are described. A brief review of the development of quantum-well electroabsorp-

tion modulators will also be presented. Finally, we discuss the types of results that a good electroabsorption modulator simulation tool must be able to provide to be useful, and we discuss the types of physical models that must go into such a simulator in order for these results to be obtainable.

Chapter 3 concerns modeling of the electroabsorption modulator as a functional component. Using a simple model which takes propagation effects into account, we investigate all-optical wavelength conversion, all-optical signal regeneration, and all-optical demultiplexing.

Chapter 4 describes our detailed model for the absorption dynamics in electroabsorption modulators, PinSim. The model is intended to be a tool for gaining better understanding of the sweep-out process in electroabsorption modulators, and for optimizing modulators with respect to some desired functionality.

In Chapter 5, we use PinSim to investigate steady-state properties of electroabsorption modulators. Absorption spectra are calculated and compared to measured absorption spectra. The dependence of the absorption coefficient on the optical excitation power is investigated, and banddiagrams for different power levels are discussed. The influence on the dynamics from the band line-up, from the design of the separate-confinement heterostructure, and from carrier recapture is also discussed.

Chapter 6 presents modeling of the absorption recovery in various structures. PinSim is used to determine how various parameters influence the dynamics. Parameters that are investigated include the number of wells, the position of the wells, the well depths, the separate-confinement heterostructure design, and a number of other important design parameters. The influence of the optical power level on the recovery is also discussed, as is the issue of carrier recapture in electroabsorption modulators.

Chapter 7 concludes the work with a brief review of the results. We discuss the future for a detailed electroabsorption modulator model such as PinSim, and make suggestions for next-step applications of the model.

Chapter 2

The electroabsorption modulator

As the name indicates, electroabsorption modulators are based on the electroabsorption effect. Electroabsorption effects were first reported in 1958, by Franz [1] and Keldysh [2], who described how the application of an electric field to a bulk semiconductor crystal red-shifts the absorption edge. This is the so-called *Franz-Keldysh effect*. At non-zero fields, the probability for an electron to tunnel from the valence band to the conduction band via absorption of a photon with an energy below the material bandgap energy is greater than zero. Figure 2.1 shows schematically an electron state and a hole state in a bulk semiconductor crystal for some non-zero field. In the presence of the field, the energy separation $E_{\mathrm{e-h}}$ between the electron and hole states shown in the figure is lower than the bandgap energy, E_{g}.

There is also an electroabsorption effect in quantum-well structures. In such structures, the absorption edge is determined by the quantized states in the wells, and by the binding energy of the exciton. When an electric field is applied in the direction perpendicular to the quantum-well layers, the well-state energies are reduced, whereby the energy of the effective band gap is lowered. This is referred to as the *quantum-confined Stark effect* [3, 4]. Figure 2.2 shows, on the left, the electron and hole ground states at zero field; on the right, the corresponding states are shown for a non-zero field. The illustration shows how the energy separation between the two states, $E_{\mathrm{e-h}}$ for zero field and $E'_{\mathrm{e-h}}$ for the non-zero field, is reduced when the field

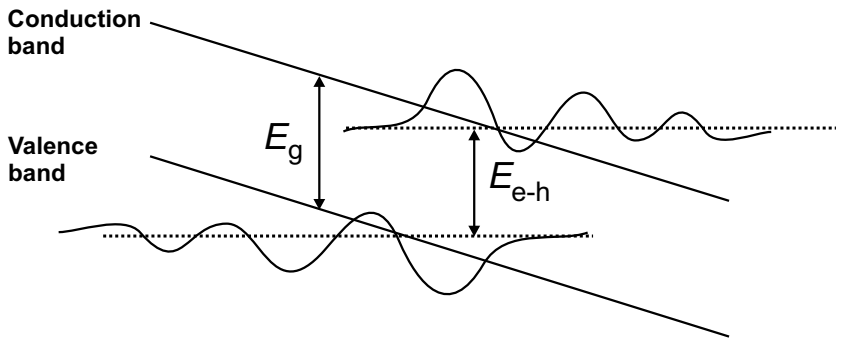

Figure 2.1: The application of an electric field to a bulk semiconductor crystal causes a lowering of the eigenstate energies. Consequently, the absorption edge moves to lower energies, down below the bandgap energy.

is applied. The binding energy of the exciton changes only little with field, and the main contribution to the quantum-confined Stark effect is therefore due to the field-induced change in the energies of the confined states [4, 5]. The quantum-confined Stark effect is interesting because the absorption near the band gap in quantum-well structures can change significantly faster with field than the absorption near the band gap in comparable bulk structures [6]. Modulators with quantum wells can therefore be driven with smaller modulation voltages than bulk modulators. Smaller modulation voltages translate into higher operation speeds, given that the operation speed is limited by the electrical driver circuit and not by the intrinsic carrier transport properties of the two types of devices.

The Franz-Keldysh effect and the quantum-confined Stark effect are fundamentally related [5]. However, the absorption edge in a bulk structure stems from transitions between extended states, whereas the absorption edge in a quantum-well structure is due to transitions between localized states. Furthermore, the exciton binding energy is greater for a quantum well than for bulk, giving an excitonic absorption contribution in the quantum-well structure that persists to much higher fields [4].

The field can also be applied parallel to the quantum well layers. In this case, the electroabsorption effect is qualitatively similar to that in bulk, that is, to the Franz-Keldysh effect. However, the exciton persists to higher fields than in bulk, although not to as high fields as with a perpendicular field [4].

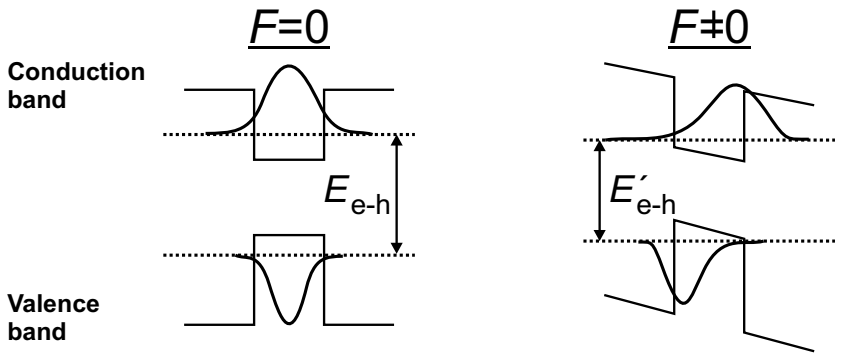

Figure 2.2: Schematic illustration of the electroabsorption effect in a quantum well. *Left*: The electron and hole wavefunctions and energies when the electric field, F, is zero. *Right*: Wavefunctions and energies at non-zero field.

The development of electroabsorption modulators

With the advent of sophisticated crystal growth methods, the electroabsorption modulator has become an interesting component, especially for the telecom industry. One of the first reports on modulation based on the electroabsorption effect is from 1964 [7], and in 1976, electroabsorption-based waveguide devices were first discussed [8].

The quantum-confined Stark effect, that is, the change in absorption induced by a field perpendicular to the layers of a quantum-well structure, was first reported in 1984 [9]. At that time, high-quality quantum-well structures could be realized due to developments within the crystal growth technology [10], and multi-quantum-well electroabsorption modulators quickly came to overshadow bulk electroabsorption modulators. Bulk material has the nice property that the material absorption is intrinsically polarization independent. However, the larger electroabsorption effect in quantum-well structures and the many extra degrees of freedom that material alloying of ternary and quaternary materials offers, have been responsible for the much larger interest in quantum-well modulators compared to bulk modulators. Investigations also showed that larger electroabsorption effects could be reached in quaternary materials than in ternary materials [11], underlining the advantage of using quantum-well structures and complex material alloying.

Early on, AlGaAs was the material of choice because in that material an

excitonic resonance could be seen in bulk material even at room temperature. In GaAs/AlGaAs *quantum-well structures*, the exciton resonance can be very strong even at room temperature [4]. Soon after, clear room-temperature excitonic resonances were seen also in GaInAs/AlInAs quantum-well structures, making available a material system with a completely different operation wavelength, around 1.6 μm, compared to the 850-nm range that characterizes the AlGaAs system [12]. The GaInAs/AlInAs material system is also characterized by a different band line-up than that in the GaAs/AlGaAs system [12]. In 1985, the waveguide geometry was used for the first time in quantum-confined Stark effect devices [13]. Up until then, modulators had been illuminated from the top. In the waveguide geometry, light propagates in bound modes in a direction parallel to the quantum well layers, and the interaction length can therefore be much longer with this geometry, in principle as long as desired [13].

Other material systems, such as GaSb/AlGaSb [14], GaInAsP/InP (quaternary) [15], GaInAs/InP [16, 17], and AlGaInAs/AlInAs (quaternary) [18] were tried out. It was found that strain could be used as a means of enhancing the electroabsorption effect [19] (the quaternary InGaAlAs system is used in [19]). At the same time, the first monolithically integrated distributed feedback laser/electroabsorption modulator (DFB-EAM) devices were fabricated [20-22]. The pulse extinction ratios were below 3 dB, and the switching times were close to 300 ps. The modulator parts were based on InGaAsP/InP wells.

The absorption in electroabsorption modulators can be reduced through optical excitation of carriers. Before 1990, it was known that part of the absorption change was caused by band-filling, and it was believed that this was the main contribution to the absorption reduction, at least at very low fields. In 1990, it was demonstrated for the first time that a significant part of the absorption reduction in multi-quantum-well structures induced by optical excitation is due to photo-excited carriers screening the field across the wells [23]. This effect is one of the pillars for a number of the functions that electroabsorption modulators can perform.

In the following years, the development of electroabsorption modulators went fast. Modulation speeds reached and surpassed 10 Gbit/s, both in standalone devices [24-26] and in integrated DFB-EAM devices [27]. Strain came to be used extensively to make devices with low polarization-dependent losses [28-30].

The further developments focused on improving the performance of the devices, increasing operation speeds, lowering the polarization-dependent

losses, lowering drive-voltages, lowering insertion losses, and increasing saturation powers [31-41]. Optimization was done through experiment, with focus in the early 1990's on the electrical bandwidth, but shifting quickly towards actual high-speed applications.

Today, the most commonly-used material system for making quantum-well electroabsorption modulators is, by far, the InGaAsP system. This system, having approximately a 50:50 splitting between the conduction-band offset and the valence-band offset, gives both the best electron-hole wavefunction overlap, and the fastest hole escape. InGaAlAs-based devices have undesirably deep hole wells when the band offset ratio is optimized to give a large overlap between the electron and hole wavefunctions [42].

Applications of electroabsorption modulators

This section mainly concerns quantum-well devices, but a few results obtained with bulk devices will also be mentioned.

Pulse modulation with electroabsorption modulators started in 1984 with a 2.8-ns modulation speed [9], followed shortly after by a record-setting 131-ps modulation speed [43]. In 1992, transform-limited, 14-ps wide pulses were produced using an InGaAsP electroabsorption modulator [44] (bulk device). Other applications of the electroabsorption modulator saw the light of day: 2R regeneration, optical demultiplexing, optical switching, and noise reduction, all at 10 Gbit/s, were demonstrated [24, 26]. The development of these and other applications, besides pulse generation, did not progress much in the following five or so years.

The following year, 7-ps transform-limited pulses were produced using a multi-quantum-well device [45]. Pulses generated with electroabsorption modulators typically have a relatively low chirp. Furthermore, as mentioned above, electroabsorption modulators have low drive voltages, and they can be made to have low polarization-dependent losses. A comparable device, the Lithium Niobate ($LiNbO_3$) modulator, is intrinsically polarization-dependent; the input light should be TM polarized because this polarization is modulated three times stronger than TE polarized light. A low polarization-dependent loss is mainly important for inline applications. Dealing with the polarization-dependence of the $LiNbO_3$ modulator by introducing a TE polarization filter in front of the device is an undesirable solution. $LiNbO_3$ modulators also tend to require higher drive voltages than do electroabsorption modulators. On the advantage side, $LiNbO_3$ modulators cause very little chirping.

Also around 1992, monolithically integrated DFB-EAM devices started to perform at higher bit rates. The 7-ps pulses mentioned above were produced with such a device (one that incorporated strain). A bandwidth of 40 GHz was achieved in 1992, although for a high drive voltage of 5 V [46]. In the following couple of years, drive voltages were reduced significantly as capacitance issues were overcome, mainly by reducing device sizes [47]. In 1995, these developments led to the first integrated DFB-EAM pulse generator operating at 40 Gbit/s [40]. The mid-to-late 1990's brought improved operation, that is, lower drive voltages and higher bandwidths. The issue of electrical limitations became more pressing and has ever since been an important issue with respect to both integrated DFB-EAM devices and stand-alone modulators.

The late 1990's saw a veritable surge in the number of device applications, and new applications have kept coming ever since. Recent applications are essentially sophisticated combinations of the basic applications described above. They have almost entirely addressed optical time-domain multiplexing (OTDM) systems (which are systems based on return-to-zero pulses) and all-optical OTDM transmission systems. All-optical functions are performed with electroabsorption modulators through bleaching of the absorption by optical excitation. The most pursued functionalities today are, in arbitrary order, clock recovery and demultiplexing [48-57], wavelength conversion [58-60, 51, 57], and signal regeneration [61-65].

Modeling of electroabsorption modulators

A significant amount of modeling of specific electroabsorption modulator properties, such as the absorption spectrum, have been presented [66-70]. A few publications on steady-state field and carrier distributions in *bulk* electroabsorption modulators have also been presented [71-74]. With respect to quantum-well structures, quite a few publications have been concerned specifically with the time it takes carriers to escape from the quantum wells. More or less sophisticated models for the carrier escape times from quantum wells have been developed to reproduce measured absorption recovery times. The models have been relatively simple, in that they have taken the absorption recovery time to be synonymous with well escape times [75-80]. Furthermore, the results have mainly concerned structures with one or a few wells. There is some drift-diffusion type modeling of quantum-well photo-detectors, which in some respects are similar to electroabsorption modulators. But also in this

case, the work has concerned steady-state properties, and only a few of the essential transport mechanisms have been considered [81-83].

With respect to actual design of modulators, there are a number of papers on optimization of the overlap between the optical field and the well region [84], on electrical small-signal bandwidth optimization [85-87], and on steady-state optimization of various figures of merit, such as extinction ratio divided by applied bias modulation amplitude, or bandwidth divided by drive voltage [88, 36]. Another approach to device optimization is based on experimental results: A number of components are fabricated and compared, and a structural "interpolation" is applied to pull the device properties in the desired direction [47, 89].

Comprehensive, detailed simulation tools for modeling of the carrier sweep-out dynamics in electroabsorption modulators are almost non-existent. This is somewhat surprising, as the electroabsorption modulator in many ways is similar to the semiconductor laser, for which a substantial number of modeling tools exist. Actually, a reverse-biased semiconductor laser *is* an electroabsorption modulator. Various laser models are presented in [90-94].

A comprehensive model for electroabsorption modulators should provide structure-dependent information about the properties that are important for high-performance operation. A good device has:

- A high extinction ratio (i.e., on-off ratio)
- A low drive voltage (for electrical pulse generation)
- A low insertion loss, meaning that the absorption in the on-state (the low-absorption state) is low
- A high operation speed
- A low chirp (chirping causes pulse-broadening during transmission in fibers)
- A wide wavelength-range of operation
- Low polarization-dependent losses

It is clear that a comprehensive model is required to describe these properties. The model must be able to calculate, simultaneously,

- The absorption spectrum

- The intrinsic dynamical properties
- The optical waveguiding properties

Obviously, a large number of basic, physical models are required to describe these properties.

The group of Voges has put a significant effort into making a detailed quantum-well electroabsorption modulator drift-diffusion type model [95, 96]. Their model includes, in a self-consistent way, a detailed description of the absorption. Only a few results, which have focused on steady-state properties, have been published so far. As an example, a field-induced blue shift of the absorption from an asymmetric quantum well has been investigated in detail [96]. Recently, the group has published a paper that presents dynamical calculations of changes in absorption induced by the application of a modulated voltage [97]. To our knowledge, the paper by Voges *et al.* is the only published work on modeling of electroabsorption modulators that is based on a comprehensive simulation tool.

Comprehensive modeling of dynamical, optically induced absorption changes in electroabsorption modulators have not, to our knowledge, been presented. The present work addresses this area. There are many different parameters that one can change in an electroabsorption modulator structure: The number of wells, the well depths, the width of the intrinsic region, and so on. Being able to model the absorption recovery for a specific device structure is useful both because it provides a basic understanding of the sweep-out process, and because it enables us to adjust parameters to improve device performance. The main part of this thesis is concerned with detailed modeling of the influence of different parameters on the dynamical properties of electroabsorption modulators.

Chapter 3

Modeling of all-optical signal processing

Optical communication systems are rapidly moving towards a new level of sophistication. As more bandwidth is required, the channel rate and the number of channels are being increased. This adds complexity to the systems, and the conventional approach to signal processing, where each wavelength channel is processed electrically, becomes impractical. Introducing components that are able to perform signal processing in the optical domain will reduce the complexity significantly.

Today, only amplification is performed all-optically in commercial systems, using either erbium-doped fiber amplifiers or Raman amplifiers. These are pumped optically and can provide gain in a large spectral region around 1550 nm; the Raman amplifier can also provide gain away from the Conventional Band. Research efforts are bringing other all-optical functionalities — such as wavelength conversion, multiplexing and demultiplexing, and routing — ever closer to maturity.

Recent achievements of all-optical functionalities using electroabsorption modulators include all-optical wavelength conversion up to 60 Gbit/s [58, 60, 64] and signal regeneration up to 40 Gbit/s [61-64]. Such achievements have thoroughly established the usefulness of the electroabsorption modulator as an integrated component for optical signal-processing. Furthermore, the electroabsorption modulator has a large wavelength range of operation, as exemplified by [26] where an on-off ratio of 20 dB is obtained from 1.53

μm to 1.57 μm.

The electroabsorption modulator is not the only viable component for realizing all-optical functions, and a number of alternative approaches are being pursued in parallel. Demultiplexing, for instance, has been realized by a number of other approaches, including SOA-based interferometric schemes [98, 99]. Each method and device type has its advantages and drawbacks, and to develop the fastest, most flexible, most reliable, and most cost-efficient components, these advantages and drawbacks must be investigated.

In this chapter, three all-optical functions performed using an electroabsorption modulator are modeled. They are: Wavelength conversion, regeneration, and demultiplexing. All-optical functionalities are realized with electroabsorption modulators through cross-absorption modulation, which relies on the electroabsorption modulator's saturable absorption characteristic, as well as on the field-induced absorption changes that photo-excited carriers in the modulator give rise to.

3.1 Description of the propagation model

Our model for the absorption dynamics in reverse-biased quantum-well absorbers is based on a large-signal model that was originally developed for studying colliding-pulse mode-locked lasers [100]. The model includes a detailed gain model derived using the density matrix formalism [101]. It also incorporates a sweep-out mechanism to simulate the power-dependent dynamical properties in electroabsorption modulators. Finally, it contains propagation equations that allow us investigate system-related issues.

The expressions for the densities of electrons and holes in the quantum wells are:

$$\frac{\mathrm{d}N(z,t)}{\mathrm{d}t} = \alpha\left(N,P\right) v_g \Gamma S(z,t) - \frac{N(z,t)}{\tau_{\mathrm{so}}(N)} \tag{3.1}$$

$$\frac{\mathrm{d}P(z,t)}{\mathrm{d}t} = \alpha\left(N,P\right) v_g \Gamma S(z,t) - \frac{P(z,t)}{\tau_{\mathrm{so}}(P)} \tag{3.2}$$

where z is the direction of propagation, t is the time variable, N is the density of electrons in the wells, P is the density of holes in the wells, α is the absorption coefficient, v_g is the group velocity for the optical mode, S is the photon density in the mode, Γ is the confinement factor, and τ_{so} is the

sweep-out time. Below, we return to the model of $\tau_{\rm so}$. The sweep-out time represents the entire sweep-out process, including escape from wells, bulk transport away from the wells, and transport across separate-confinement heterostructures. The absorption coefficient is calculated as function of the well carrier densities, and takes into account both spectral-hole burning and carrier heating. Because we do not describe the field behavior in the device, electroabsorption effects are not included. This means that the absorption changes included here are those induced by band filling only. The equation for the optical field in terms of the photon density is [102]

$$\frac{\partial S(z,t)}{\partial z} + \frac{1}{v_g}\frac{\partial S(z,t)}{\partial t} = -\left(\Gamma\alpha\left(N,P\right) + \alpha_{\rm int}\right) S(z,t) \tag{3.3}$$

where $\alpha_{\rm int}$ is the internal loss coefficient. We found that two-photon absorption had an insignificant effect on our results, and we have therefore not included this term in the equations above.

A simple carrier-density-dependent sweep-out time is used to describe, on a phenomenological level, the retardation of the sweep-out at higher power levels. In the literature, sweep-out times on the order of some tens of picoseconds have been reported for InGaAsP and AlGaAs multi-quantum-well structures, even at moderate reverse biases, around ~ -5 V [76, 103]. Elsewhere, absorbers have displayed even faster recovery times [61, 104]. We have implemented a simple model in which the sweep-out time varies with the carrier density, from 8 ps at low densities to 25 ps at transparency, based on the results in [58]. The mechanism that leads to increased sweep-out times at higher carrier densities is screening of the field across the well region by photo-excited carriers, see e.g. [23, 76, 103]. Investigations of the detailed sweep-out dynamics in electroabsorption modulators will be presented in Chapter 6. The sweep-out model used in this chapter is much simpler. It is assumed that the sweep-out rate is proportional to the field, E, across the wells, or equivalently: The sweep-out time is proportional to the inverse of the field:

$$\tau_{\rm so}(N) = \frac{k_1}{E(N)} \tag{3.4}$$

This behavior is qualitatively correct both for the escape from the wells and for the transport away from the wells. When carriers are excited, the field is

screened such that

$$E(N) = E_0 - \Delta E(N) \tag{3.5}$$
$$= E_0 - k_2 N \tag{3.6}$$

Here, E_0 is the electric field at zero carrier density, and k_2 is a variable that physically relates the field change to the carrier density change. One can picture the holes being on one side of the wells (the p-contact side) and the electrons being on the other side of the wells (the n-contact side). Such a distribution results in a uniform field across the well region, and the size of the field *change* is proportional to the density of carriers, according to Poisson's equation (Eq. (4.5) in Chapter 4).

We assume that the sweep-out time is $\tau_0 = \tau_{\rm so}(N = 0) = 8$ ps when there are no screening carriers, and $\tau_{\rm tr} = \tau_{\rm so}(N = N_{\rm tr}) = 25$ ps when the carrier density in the device equals the transparency density, $N_{\rm tr}$. Using the expressions above we find the following expression for the carrier-density-dependent sweep-out time:

$$\tau_{\rm so}(N) = \frac{\tau_0 \tau_{\rm tr}}{\tau_{\rm tr}\left(1 - \frac{N}{N_{\rm tr}}\right) + \tau_0 \frac{N}{N_{\rm tr}}} \tag{3.7}$$

We assume that the same time characterizes the sweep-out of electrons and the sweep-out of holes. This means that $N = P$ in all equations above (we have ignored recombination). Figure 3.1 shows $\tau_{\rm so}(N)$. As mentioned, we use $\tau_0 = 8$ ps and $\tau_{\rm tr} = 25$ ps. Figure 3.1 also shows the sweep-out time as function of carrier density when $\tau_0 = 2$ ps and $\tau_{\rm tr} = 25$ ps. Our model has the property that the screening sets in at higher densities, whereas the sweep-out time increases little at low densities.

3.2 The absorption nonlinearity in electroabsorption modulators

In this chapter, we consider an InGaAsP modulator device with five quantum wells excited optically by TE polarized light. Figure 3.2 shows schematically the wavelength conversion scheme, which is the subject of Sec. 3.3. A control signal at wavelength λ_1 containing a bit-sequence, and a CW signal at λ_2 are launched into the electroabsorption modulator. At the output end of the elec-

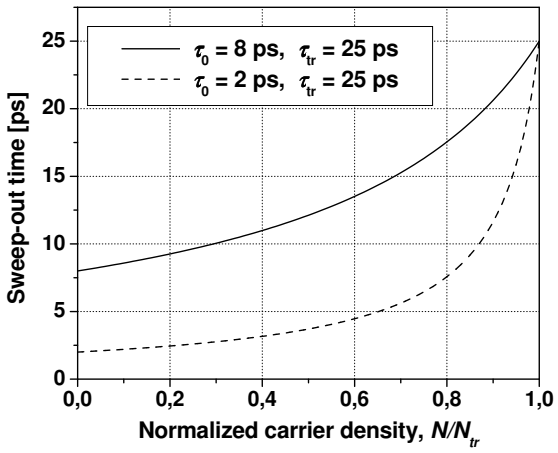

Figure 3.1: The sweep-out time as function of carrier density for two different sets of low-density and high-density sweep-out times, τ_0 and $\tau_{\rm tr}$.

troabsorption modulator, the bit-sequence represented by the control signal has been transferred to the CW signal through cross-absorption modulation. A reverse DC bias is applied to adjust the band edge as well as for ensuring a fast sweep-out of the photo-excited carriers.

Figure 3.3 shows the calculated output energy of a pulse transmitted through the device, as function of the input pulse energy, for various wave-

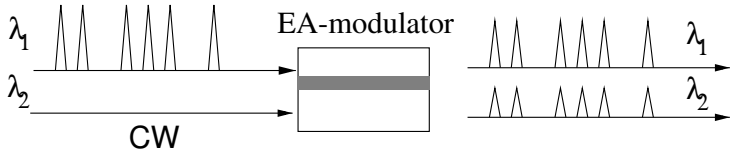

Figure 3.2: Illustration of the wavelength conversion scheme. A data signal at wavelength λ_1 and a CW signal at λ_2 are injected into an electroabsorption modulator from the same end (*co-propagation scheme*). Through cross-absorption modulation the information from the control signal at λ_1 is transferred to the CW signal at λ_2.

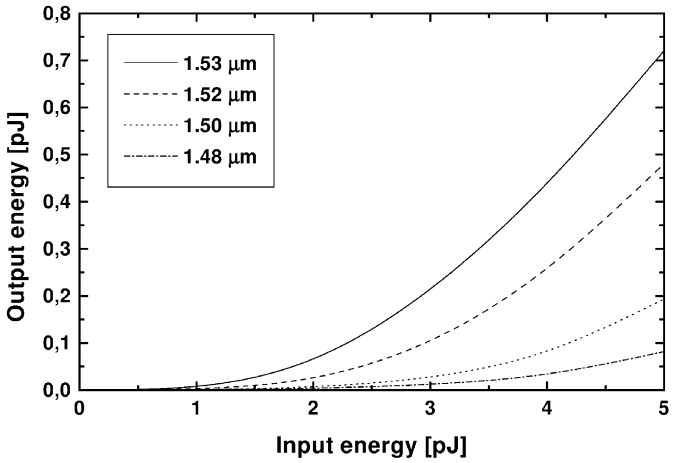

Figure 3.3: The graph shows the output pulse energy as function of input pulse energy. The pulses propagate through a 150 μm long device. The results are shown for four different wavelengths, and illustrate the nonlinear absorption property of the electroabsorption modulator.

lengths. Only pulses (at λ_1) are sent through the device in this calculation. For small pulse energies, the absorption corresponds to essentially empty bands. Thus, the absorption due to promotion of carriers to the conduction band is high, and the output energy is much smaller than the input energy. When the pulse energy is increased the absorption is bleached (i.e, reduced) due to phase-space filling in the bands, and tends towards the internal loss. The internal loss is made up of losses in the active region, such as free-carrier absorption, absorption in the cladding, and scattering losses [105]. We use a value 40 cm^{-1} for the internal loss. The results are quite insensitive to the exact value of the internal loss because the overall absorption is dominated by the stimulated absorption.

Figure 3.3 also indicates another important issue, namely that the output energy is severely reduced when the wavelength is decreased due to the increased absorption. The energy required to bleach the absorption thus increases, and switching thus requires increasingly more energetic pulses as the wavelength in decreased.

If one relies entirely on the change in absorption obtained through phase-

space filling, it is not desirable to have λ_2 (the CW signal wavelength) at longer wavelengths, close to the band edge. This is because the change in absorption here is relatively small, due to the relatively low density of states there. On the other hand, operating far into the band is also not desirable, for the reasons described above. Hence, a compromise must be made to obtain both a reasonable output power (which favors longer wavelengths), and an efficient modulation of the carrier density (favoring shorter wavelengths). By the same token, the controlling signal, at λ_1, should not be too close to the band edge, or its overall influence on the carrier density will be small and its influence on the absorption at the CW wavelength λ_2 will be correspondingly small. If one wishes to regenerate the signal at λ_1, this wavelength should again not be too far into the band, again due to output power considerations.

3.3 Wavelength conversion in electroabsorption modulators

In our simulations we have mainly considered the *co-propagation scheme*, in which the two signals enter the device from the same end as shown in Fig. 3.2.

In the following we use the model to investigate wavelength conversion and signal regeneration at 10, 20, and 40 Gbit/s. The sweep-out time is a function of the local carrier density by Eq. (3.7). Thus the absorption recovery time decreases throughout the component because absorption decreases the light intensity with length. The influence of device length and power level will be investigated. In all the results presented the pulse full width at half maximum (FWHM) is set to 8 ps.

Wavelength conversion and signal regeneration at 10 Gbit/s

To demonstrate the wavelength conversion and signal regeneration capability of the electroabsorption modulator, we propagate various bit patterns consisting of 8 ps wide return-to-zero (RZ) pulses with an extinction ratio (ER) of 10 dB (peak-to-floor) through the device. The 10-dB extinction ratio is introduced by adding a constant background to the bit-sequence at the wavelength λ_1. The background allows us to simulate the presence of unwanted signals. This could for instance be an OTDM[1] channel that was not perfectly

[1] OTDM: *Optical time-division multiplexing*

cleared during a signal drop (i.e., signal demultiplexing and clearing), or it could be spontaneous emission added by e.g. signal generators and amplifiers (and other active components) previously encountered in the system.

The bit-patterns used were chosen such that the worst possible eye was obtained. The eyes therefore do not represent statistical results. Instead, we look at the size of the eye opening, which means that we estimate the worst-case ER.

Figure 3.4 shows a simulation where a 10-dBm CW signal ("CW" in Fig. 3.4) at $\lambda_2 = 1520$ nm and an 11.5-dBm (average pulse power) bit-stream signal ("signal" in Fig. 3.4) at $\lambda_1 = 1510$ nm are launched into the electroabsorption modulator from the same end (co-propagation scheme, shown in Fig. 3.2). Note that the quoted average pulse power includes the contribution from the background, which is relatively more important at low bit-rates,

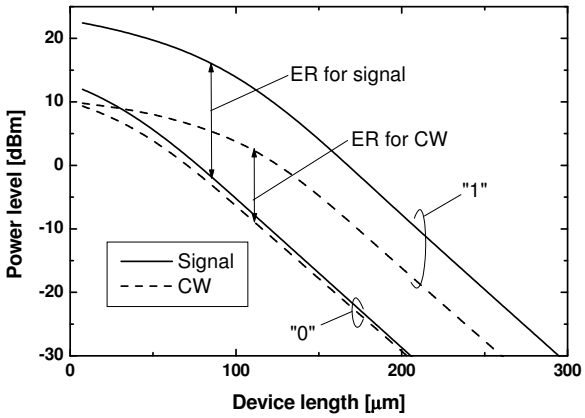

Figure 3.4: Power levels for space and mark as function of length for then control signal ("signal") and the CW signal ("CW"). The bit-rate is 10 Gbit/s. The input power of the control signal was 11.5 dBm, while the power in the CW signal was 10 dBm. The ER was extracted from worst-case eye-diagrams.

where the duty-cycle is low. In practice, the two signals would be separated at the output of the device using a spectral filter. The figure shows the power levels for mark (1-bit) and space (0-bit) as function of device length. For increasing device length, the ER increases both for the control signal and for the converted signal (the latter with an ER of 0 dB at the input), demon-

strating the wavelength conversion and signal regeneration capabilities of the device. When the control signal power level becomes too low to significantly influence the absorption (through band filling), the ER levels out. In the following we will refer to the length in which the ER increases as the *effective length*. The power level, however, keeps decreasing due to the internal loss and stimulated absorption.

Figure 3.4 clearly shows that the improvement in ER, which takes place for both signals, comes about due to the non-linear saturation properties: The energy in a space decreases more rapidly than the energy in a mark due to the higher absorption for smaller input pulse energies. To ensure a certain power level at the output, the length of the device must be kept below a certain value, the size of which of course depends on the input power levels.

Pulse energy dependence

The obtainable ER depends on the input power level of the control signal. Figure 3.5 shows the ER of a converted 10 Gbit/s signal as a function of device length for various average control pulse energies. Corresponding for example to an average power of 11.5 dBm (average pulse energy of 2.8 pJ), an ER of $\approx$12 dB can be obtained on the converted signal. Fig. 3.5 also shows that the ER obtained below, say 150 μm, for the highest input power level shown (11.2 pJ average pulse energy) is smaller than that obtained using a range of lower input power levels. This is because the saturation of the absorption in the first part of the device suppresses efficient carrier density modulation. This indicates that for a given device length there is an optimum input power level giving the highest ER at the output. This is demonstrated in Fig. 3.6, where the extinction ratio at the output of a 110 μm long device is shown as a function of the average control pulse energy. A maximum ER at the output is found in this case around an average pulse energy of 4 pJ. For a longer device the maximum ER increases and occurs at a higher input energy. This can be seen from Fig. 3.5.

Wavelength conversion up to 40 Gbit/s

To investigate the wavelength conversion capability at higher bit-rates, we modeled the propagation of 10, 20 and 40 Gbit/s pulse-trains through the electroabsorption modulator. Again, we chose the pulse-trains to ensure the worst possible eye-distortion. The background signal introduced earlier in

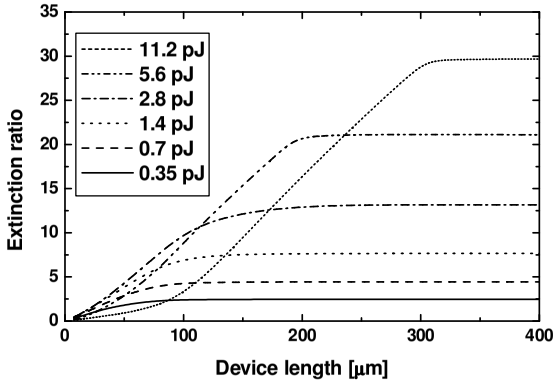

Figure 3.5: Extinction ratio of a converted 10 Gbit/s signal as function of length with average control pulse energy as a parameter. The ER was extracted from worst-case eye-diagrams. The CW power level was $P_{cw} = 10$ dBm.

this section is included in the calculation, resulting in the before-mentioned input extinction ratio of 10 dB. We assumed that there is no jitter on the input signals. This is course an idealization, and any noise on the input signals (amplitude or timing jitter) will reduce the eye-opening of both the converted and the control signal. However, these are small effects compared to the distortions due to patterning, that we would find *even without noise*. Noise on the input will tend to smear out the rather discrete levels found in the figures.

Eye-diagrams for converted signals, for different device lengths are shown in Fig. 3.7 and Fig. 3.8. The input power levels for the 10, 20 and 40 Gbit/s control signals in Fig. 3.7 were 13, 16, and 19 dBm, respectively, and 16, 19, and 22 dBm, respectively, in Fig. 3.8. The eyes are shown for 125 and 200 μm long devices.

In Fig. 3.7, the quality of the eye for the 10 Gbit/s signal hardly improves from 125 to 200 μm, because the remaining power level at $L = 125$ μm is too small to influence significantly the absorption (see also Fig. 3.4). Note that the width of the pulses making up the converted signal decreases slightly with length. For the 20 Gbit/s signal, the eye-quality in Fig. 3.7 also improves only little as the length of the electroabsorption modulator is increased from 125

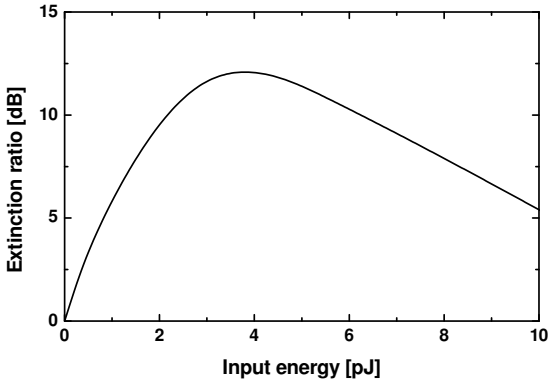

Figure 3.6: Extinction ratio for the converted signal as function of average input energy of the control signal for a 110 μm long device. The bit-rate was 10 Gbit/s. The ER was extracted from worst-case eye-diagrams.

to 200 μm, although some amplitude variation now appears in the marks. This variation comes about because the time-slot per bit is too short to allow the absorption to recover from on bit to the next. Finally, in the 40 Gbit/s case the converted signal eye for the 125 μm long device shows a large range of both the space and the mark (only the mark levels can be clearly distinguished in the diagrams), resulting again because the absorption does not recover completely from one time-slot to the next. As expected, the distortion is more severe at 40 Gbit/s than at 20 Gbit/s. The distortion seen in the eye agrees well with the experimental results in [58].

In Fig. 3.8 the power level for the control signal at each individual bit-rate is twice as large as that in Fig. 3.7. At 10 Gbit/s this results in a better ER at both 125 μm and 200 μm. This is the eye-diagram manifestation of the dependence shown in Fig. 3.5 in terms of the ER, namely that a moderately higher power level can result in a better ER at the output. At 20 Gbit/s there is some distortion, again because the absorption has not completely recovered from one bit to the next. The distortion here is greater than in Fig. 3.7 due to the higher power level compared to that in Fig. 3.7. The distortion especially at $L = 200$ μm is larger than in the corresponding eye in Fig. 3.7. The reason is that the higher power level for the control signal

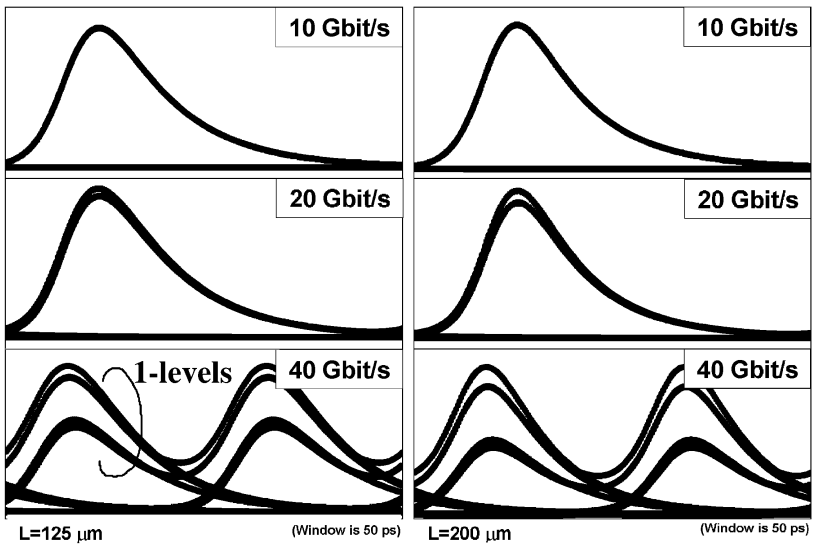

Figure 3.7: Converted 10, 20 and 40 Gbit/s signal at the output of a 125 μm long device (*left*) and a 200 μm long device (*right*). The CW power was 10 dBm and the signal power is 11 dBm at 10 Gbit/s, 16 dBm at 20 Gbit/s, and 19 dBm at 40 Gbit/s. We explicitly point out that the levels indicated in the left figure (and similar levels in the following figures) are all marks. The temporal window is 50 ps for all bit-rates.

in Fig. 3.8 gives a longer effective length. The longer sweep-out time further increases the effective length, altogether resulting in a better ER. For the 40 Gbit/s case, the distortion encountered in Fig. 3.7, where the mark is broadened, is at first slightly suppressed because each pulse saturates the absorber more. However, the background is also higher, again on account of the higher power level). At $L = 125$ μm, the overall result is a lower ER at the higher power level. At $L = 200$ μm the ER is about the same as for the lower power level, but the mark variation is higher. From a detection point-of-view this will result in a higher bit error rate.

Another interesting and important feature is seen when comparing for instance the 10 Gbit/s converted signal in Fig. 3.7 with that in Fig. 3.8: The converted signal at the output of a 125 μm long device is broader in Fig. 3.8 than in Fig. 3.7. However, at $L = 200$ μm, the situation is reversed.

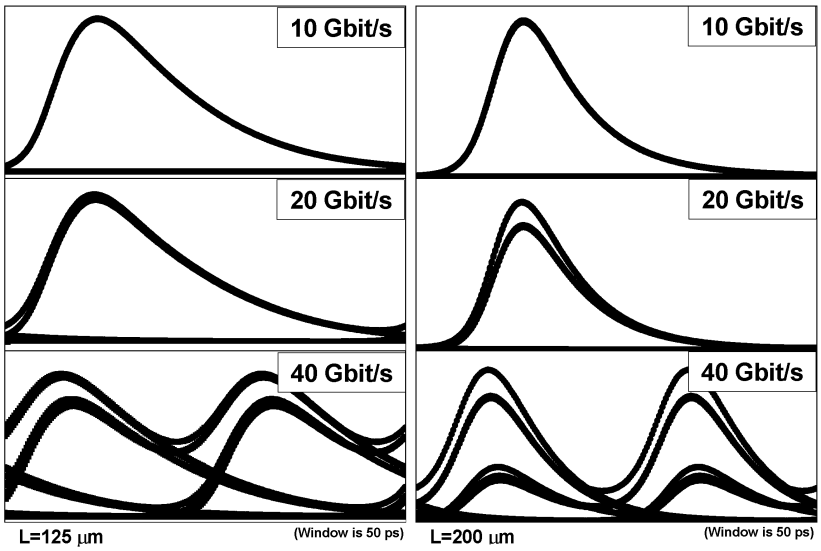

Figure 3.8: Similar to Fig. 3.7, but the power level for control signal is 16 dBm at 10 Gbit/s, 19 dBm at 20 Gbit/s, and 22 dBm at 40 Gbit/s. The temporal window is again 50 ps for all bit-rates.

In general, this is due to the fact that the conversion happens over a longer distance for the more energetic signal. Initially the higher power level will give broader converted pulses due to a longer sweep-out time, but eventually (with length) the higher power levels give more narrow pulses due to the longer conversion length.

To summarize, the converted signal at 10 Gbit/s is improved for both the 125-μm device and the 200-μm device by doubling the power level. At 20 Gbit/s doubling the power gives a slightly worse ER for the shorter device, but an improvement for the 200-μm device, and the width of the converted pulses is more narrow, but at the expense of a greater broader converted mark. For the 40 Gbit/s case doubling higher power level initially helps to suppress amplitude variations, but also lifts the background. For the longer device, the converted signal shows about the same extinction ratio for the two power levels, but just as for the 20-Gbit/s case this happens at the expense of more amplitude variation in the mark, and even more so at 40 Gbit/s than at 20 Gbit/s.

Note that the converted pulses thus generated are somewhat broader than the control pulses. This is a general property of this type of conversion scheme. It is especially the trailing edge of the converted pulses which is longer than that of the control pulse because the sweep-out dynamics "keeps the device open", giving the converted pulses an asymmetric pulse shape. This asymmetry increases for longer sweep-out times, again demonstrating the importance of keeping the sweep-out time short.

Co- and counter-propagation schemes

So far we have considered the co-propagation scheme where the control and CW signals are launched into the same end of the device as shown in Figure 3.2. However, the wavelength conversion can also be performed by launching the two signals into the device from opposite ends (*counter-propagation* scheme). The latter method allows for conversion to the same wavelength, and bypasses the need for spectral filtering at the output of the device.

Figure 3.9 shows the extinction ratio of a converted 40-Gbit/s signal obtained for various control signal power levels and $P_{cw} = 11$ dBm. The figure shows that the difference between the extinction ratio of the converted signals obtained with the two schemes increases with the control signal power level. This is expected for our device where the control pulses are wider than the transit time through the device. The difference between the two schemes is mainly caused by the slowing of the absorption recovery that results from the higher carrier densities induced in the co-propagation scheme, where the signals are injected into the same end of the device. The result is a less efficient overall absorption modulation.

We also performed the calculation with $P_{cw} = -1$ dBm, but found less than 0.4 dB difference between the two schemes for the signal power levels shown in Fig. 3.9, which is expected based on the explanation given above.

Figure 3.10 shows the extinction ratio of a converted 10 Gbit/s signal as function of length for the two different schemes with $P_{cw} = 15$ dBm and an average control pulse power $P_{sig} = 8$ dBm. As expected, both level out as the power decreases to a level where it no longer affects the absorption. However, the counter-propagation scheme has a better overall performance in this case. This is mainly to show that the counter-propagation may be superior to the co-propagation scheme. For pulses shorter than the transit time through the device the conclusion is the opposite. In this case, the overlap between the control pulses and the CW signal favors the co-propagation scheme.

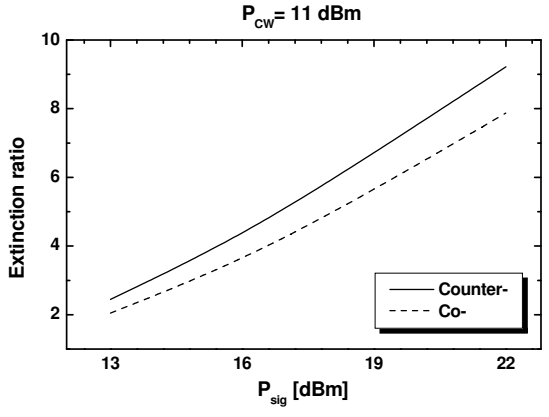

Figure 3.9: The output ER of the converted signal as function of the input control signal power level. The input power level of the CW light is 11 dBm. The bit-rate is 40 Gbit/s. The device length is 200 μm.

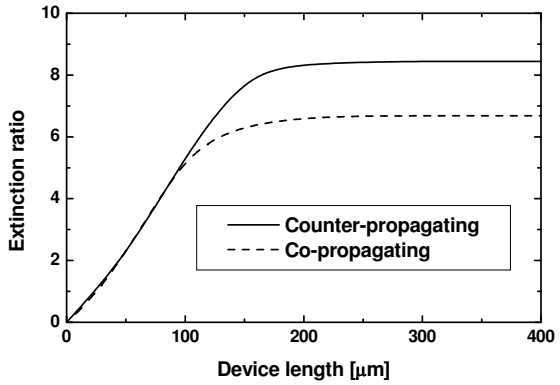

Figure 3.10: Extinction ratio of converted 10 Gbit/s signal as function of device length for co- and counter propagation schemes. The CW power is 15 dBm, and the control signal average pulse power is 1.25 pJ.

3.4 Signal regeneration

The nonlinearity used for performing wavelength conversion of course also increases the ER of the control signal itself.

Bit-rate (Gbit/s)	Power (dBm)	ER (dB) $L = 125$ μm	ER (dB) $L = 200$ μm
20	16	21.0	21.7
	19	23.4	29.5
40	19	14.7 (17.7)	15.3 (17.9)
	22	14.8 (20.9)	17.3 (23.3)

Table 3.1: ER of the control signal at the output of an electroabsorption modulator for bit-rates of 20 and 40 Gbit/s. The ER is shown for a 125 μm and a 200 μm long device and for two different average input powers. The initial ER is 10 dB. Numbers in brackets show the results obtained using a carrier-density-independent sweep-out time of 8 ps. This is discussed in a later section.

It has been shown that an incoming signal with a reminiscent pulse in the time-slot can be cleaned up [62]. We show in the following that the *constant* background introduced previously, with a power level 10 dB below the mark peak power, can be suppressed substantially. We infer that (reminiscent) *pulses* with peak powers 10 dB below the level of the actual mark can be suppressed to a similar degree. Such pulses could be present in a time-slot after a channel has been imperfectly dropped, and another added in its place.

Figures 3.11 and 3.12 show the eyes for the control signal at the input and at the output of the device. Note that we are still looking at the results of a wavelength conversion, but focusing on the control signal instead of the converted signal. The figures show features very similar to those found in the eye-diagrams for the converted signals (Figs. 3.7–3.8). However, the control signal is "born" with a 10-dB extinction ratio, and hence the difference between the spaces and the marks at the output is much greater than for the converted signal. Not surprising, the mark variations are almost identical to those of the converted signals. Note that there is a small compression of the pulses because the front of each pulse experiences a larger absorption than the rest of the pulse due to the finite sweep-out time.

One can see from Figs. 3.11–3.12 only that there is an improvement in the extinction ratios but not the actual values. The corresponding extinction ratios are therefore shown in Table 3.1. Quite a large improvement in the extinction ratio (10 dB at the input) is obtained at both 10 and 20 Gbit/s.

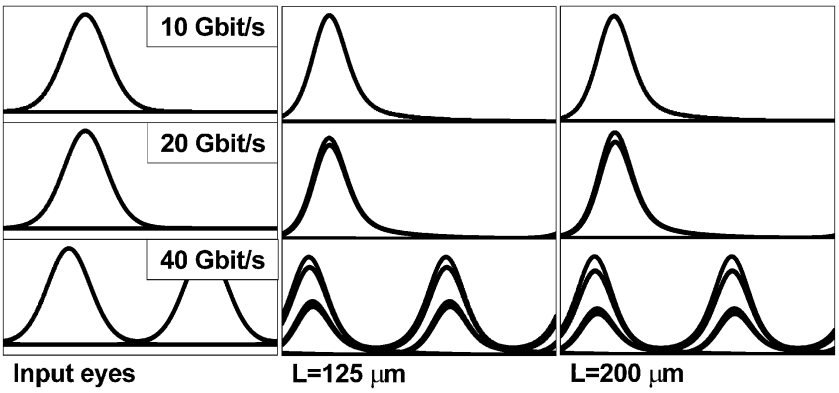

Figure 3.11: Eye-diagrams for the control signal at the output of a 125 μm long electroabsorption modulator (*middle*) and at the output of a 200 μm long device (*right*). The input control signal is also shown (*left*). The eyes are shown for 10, 20 and 40 Gbit/s signals. The CW power was 10 dBm and the signal power is 13 dBm at 10 Gbit/s, 16 dBm at 20 Gbit/s, and 19 dBm at 40 Gbit/s. The temporal window is 50 ps for all bit-rates.

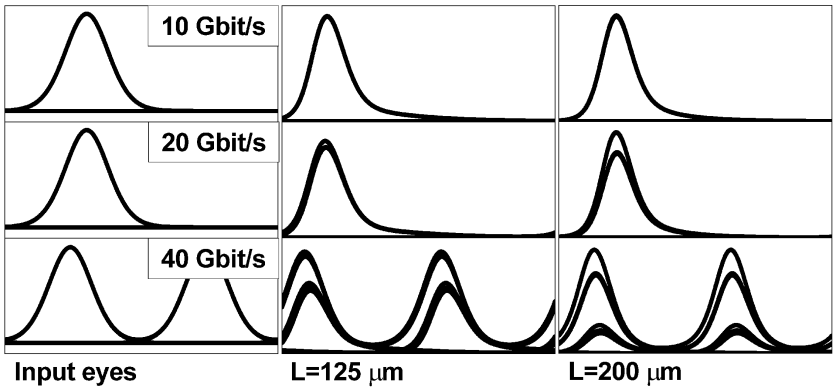

Figure 3.12: Similar to Fig. 3.11, but the power level for control signal is 16 dBm at 10 Gbit/s, 19 dBm at 20 Gbit/s, and 22 dBm at 40 Gbit/s. The temporal window is again 50 ps for all bit-rates.

As an example, a 20-Gbit/s control signal with an average pulse power of 16 dBm propagated through a 125 μm long device is improved ≈ 11 dB from 10 dB to 21 dB. If the power level is lower, the improvement will be smaller because the effective length is reduced. The improvement for the 40 Gbit/s is moderate because the absorption far from recovers from one bit to the next, as described at length in the discussion of the wavelength conversion results.

The regenerative capability could potentially used by integrating the electroabsorption modulator with for instance a Mach-Zehnder interferometer used for wavelength conversion or drop functionalities. Interferometric switches based on cross-phase modulation typically produce a finite background in the case of wavelength conversion, or small extraneous pulses in the case of drop functionality. These effects occur due to imperfect phase matching during the gain recovery in the phase-inducing semiconductor optical amplifiers. These effects could be suppressed by integrating the interferometer with an electroabsorption modulator. The power level at the output of the interferometer is quite large because the semiconductor optical amplifiers involved are operated in the gain region, thus matching well the conditions outlined above for producing improvements.

3.5 Demultiplexing

Another functionality that can be realized using the electroabsorption modulator is demultiplexing. This has been demonstrated by electrically modulating the device [49]. Recently, all-optical wavelength demultiplexing has also been realized [104, 55].

In this section demultiplexing of a 10-Gbit/s channel out of an 80-Gbit/s signal using the electroabsorption modulator is modeled. The influence of device length and control pulse power level is analyzed.

Figure 3.13 shows the demultiplexing configuration. An incoming OTDM 80-Gbit/s-signal at 1510 nm (8 channels, 10 Gbit/s each) and a 10-Gbit/s control signal at 1520 nm are launched into an electroabsorption modulator (bandgap at 1550 nm). Through cross-absorption saturation, the control signal gates the desired channel. To investigate the demultiplexing capability of the electroabsorption modulator, we propagate various 80-Gbit/s bit-patterns through the device together with a 10-Gbit/s control signal. Both consist of 3-ps wide pulses. The incoming signal has an extinction ratio of 10 dB (peak-to-floor), introduced to simulate noise in the signal as also done

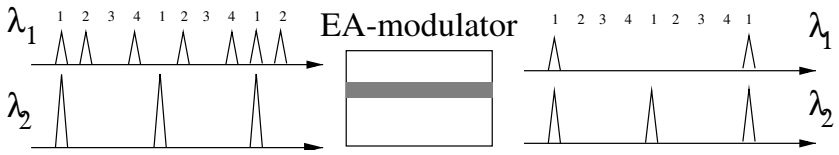

Figure 3.13: The demultiplexing configuration: Here an incoming signal at λ_1 and a local control signal at λ_2 are launched into an electroabsorption modulator. At the output, the signal aligned with the control signal is demultiplexed, the other three channels are rejected.

when wavelength conversion and signal regeneration were investigated earlier in this chapter. In this section, however, the control signal has an extinction ratio of 20 dB. The patterns chosen result in worst-case scenarios. The sweep-out time is assumed to be 8 ps, independent of the carrier density.

Figure 3.14 shows the eye-diagrams as function of device length. The figure shows that at $L = 85$ μm, the channels to be rejected are still quite strong. At $L = 125$ μm, the rejected channels are suppressed ~ 9 dB. In the eye for both the 85-μm and the 125-μm long devices a rejected mark is responsible for one of the strong remaining pulses.

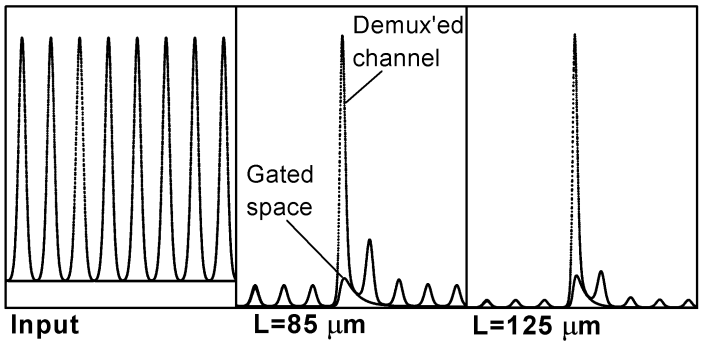

Figure 3.14: Eye-diagrams of all 8 OTDM channels at the output as function of device length. At the input, all channels are equal, but into the device, other channels than the demultiplexed are rejected. The time window is 100 ps. The control pulse energy was 14 dBm, and the average OTDM pulse power was 7 dBm

Figure 3.15 shows the level-of-rejection as function of device length for different control pulse powers.[2] As expected, higher control pulse power gives better rejection of neighboring channels as the effective length increases. Although the figure does not show this explicitly, it is clear that by increasing the power in the control signal the level-of-rejection can be increased further.

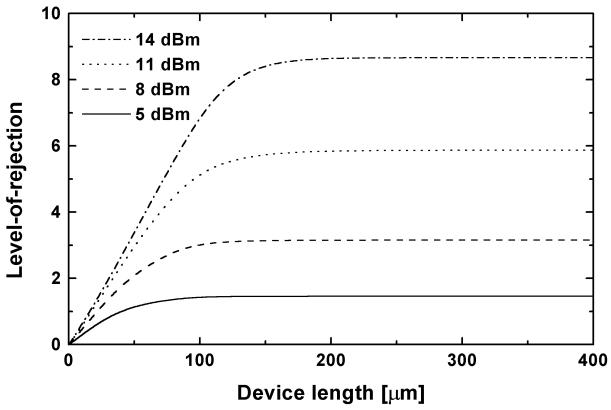

Figure 3.15: Level-of-rejection as function of length with average control pulse power as parameter. The level-of-rejection, determined by one of the rejected channels or by the gated space (whichever gives the worst eye), levels out when the control pulses become too weak to saturate the device, but the signal levels keep decreasing. Bit-patterns were chosen to obtain the greatest possible impairment.

For each power level, the level-of-rejection increases up to a certain device length. Above this length, the optical power can no longer significantly affect the absorption, but the output power keeps decreasing. In general this length thus identifies an optimum length.

Using a control signal with only a 10-dB extinction ratio instead of 20 dB, a power level of 21 dBm is required to obtain the same maximum extinction ratio that was obtained with a 14 dBm control signal having a 20-dB extinction ratio (Fig. 3.15). However, it requires a longer device, 210 μm long, before this extinction ratio is reached.

[2] The *level-of-rejection* is defined as the ratio between the peak of a gated mark and the peak of either a gated space or a rejected mark, whichever is greater.

For simple demultiplexing, the device is simple and useful, but it cannot compete with e.g. the Mach-Zehnder interferometer in drop-functionality because there is no signal improvement. Instead, the device is short, which makes it an interesting component in integrated devices. Due to its short length it may still be advantageous compared to the somewhat larger Mach-Zehnder interferometer, which is also significantly more complicated to operate. A drawback of the electroabsorption modulator is its large absorption. In this respect it cannot compete with the Mach-Zehnder interferometer.

3.6 The importance of reducing the sweep-out time

To demonstrate the effect that field screening, caused by photo-excited carriers, have on the results, we compare in Fig. 3.16 the signal regeneration at 40 Gbit/s for two different cases: In the first case the sweep-out time is the same function of the carrier density as we have used so far. In the second case the sweep-out time is 8 ps independently of the carrier density. Figure 3.16 shows that the faster sweep-out time results in a substantial reduction in the excursions of the marks. Table 3.1 shows in brackets the corresponding extinction ratios that result. Besides the reduced mark variation, also the extinction ratios are improved significantly. This means that in this type of signal regeneration scheme it is important to keep the sweep-out time low also at higher carrier densities. The same conclusions are valid for the wavelength conversion functionality.

3.7 Summary

We have modeled various all-optical functions performed with an electroabsorption modulator: Wavelength conversion, signal regeneration, and demultiplexing. The all-optical functionality of the electroabsorption modulator is based on the saturable absorption characteristic of this component.

For wavelength conversion and signal regeneration, a critical dependence of the conversion efficiency on device length and input power levels was demonstrated and explained. It was demonstrated that the extinction ratio of the converted signal saturates with length at a level which increases with the control pulse input power level. The device length required to reach

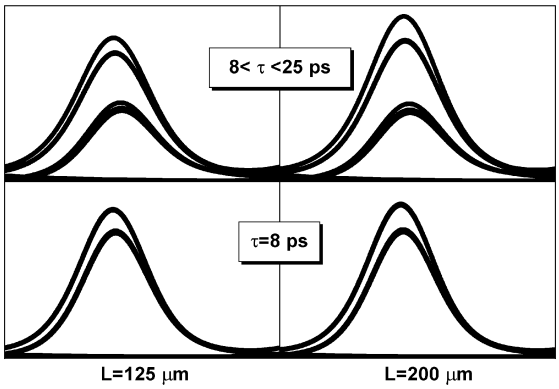

Figure 3.16: Comparison of eye-diagrams for the control signal at the output of an electroabsorption modulator with two different functional dependences of the sweep-out time, τ, on the carrier density. There is a significant reduction in the mark excursions when the sweep-out time is reduced. The results are shown for two different device lengths. The bit-rate is 40 Gbit/s, and the power levels were $P_{cw} = 10$ dBm and the average control power level was $P_{sig} = 19$ dBm. The temporal window is 25 ps in all cases.

this maximum extinction ratio depends on same power level. We showed that for a fixed device length there is an optimum control pulse power level that gives the best output extinction ratio for the converted signal.

We modeled a device with a sweep-out time between 8 ps and 25 ps. For this device, we showed that the performance at up to 20 Gbit/s is quite good for both wavelength conversion and signal regeneration. Operation at 40 Gbit/s, however, is significantly impaired by serious patterning due to incomplete absorption recovery between bits. To obtain a better performance, it is necessary to bring down the sweep-out time. In particular, it is important to reduce the power sensitivity of the sweep-out time. A better extinction ratio and smaller mark (and space) excursions were obtained when the sweep-out time was decreased.

It was demonstrated that there can be a difference in performance between the co- and counter-propagation schemes. A case was shown for which the counter-propagation gives the higher extinction ratio. The difference is due to a less efficient carrier modulation in the co-propagation scheme. In

our simulations, there was no qualitative differences in the shape of the eye-diagrams for the two schemes for the parameters we investigated.

For demultiplexing, similar dependencies were identified, and the electroabsorption modulator is clearly a viable device for performing all-optical demultiplexing. The level-of-rejection can be similar to but not much higher than the extinction ratio of the input OTDM signal because the gating hardly discriminates the space from the mark, thus preserving the input extinction ratio in the demultiplexed channel. It was demonstrated that with a carrier sweep-out time of 8 ps, it is possible to demultiplex a 10-Gbit/s channel out of an 80-Gbit/s OTDM signal.

Chapter 4

Drift-diffusion model for carrier sweep-out

The previous chapter concerned all-optical system functionalities performed using the electroabsorption modulator. The applied model included propagation effects and a simple carrier-density-dependent model to simulate the power-dependent absorption recovery in electroabsorption modulators. The sweep-out model has obvious flaws, one of them being that it only depends on the carrier density. The model also treats all wells alike, as if there were just one well. Although this may be a good approximation at low carrier densities, it most likely is not at higher densities. As for the absorption model, it included only the contribution to the absorption change that comes from band filling. Because we did not describe the field behavior, electroabsorption effects could not be included. The contributions to the total absorption change from band filling and from the quantum-confined Stark effect are similar, and thus this is an acceptable approximation for qualitative calculations.

The present chapter describes a detailed model for the absorption dynamics in electroabsorption modulators. In this model, the carrier sweep-out takes place through a number of steps, each of which is characterized by complicated transport and scattering processes. The absorption dynamics depends on a number of factors, and although a simple model like the one used in Chapter 3 can describe the absorption recovery on a qualitative level, it sheds no light on the detailed processes that govern the sweep-out of carriers, such as carrier escape out of the individual wells, and the dynamical screening in-

duced by carriers moving towards the contacts. The present model, which has been dubbed *PinSim*, helps us understand better the actual absorption dynamics, and to uncover how it is influenced by various parameters. Examples of such parameters include well depths, the band offsets, the heterobarrier structure, the width of the intrinsic region, and the excitation power level. The list is of course not exhaustive.

The intrinsic carrier transport in electroabsorption modulators is of great concern since it determines the upper limit for a modulator's operation speed. However, the electrical properties of the modulator are just as important. In reality, an electroabsorption modulator will be part of an electrical circuit. In electrical circuits, the impedance of the individual circuit elements determine the electrical power losses and reflections in the circuit. Reflections may cause damage to the electrical driver, and losses will reduce the electrical power at the modulator. Thus, for high-speed operation, both the reflections and the losses must be low. The focus in the present work is on the intrinsic transport properties. In the end of this chapter, we discuss how our simulator may be used to investigate also the electrical properties of devices.

PinSim requires as input only the epitaxial structure of a device and can therefore be used as a tool for designing modulators on the epitaxial level. One may be interested in a fast modulator, or in a modulator that has a low switching power. These properties can be investigated as function of the epitaxial structure with the present model.

4.1 A brief introduction to the model

When an optical field excites a multi-quantum-well electroabsorption modulator, carriers are excited into the wells, and from there, they escape through various scattering processes. Once out of the wells, the electric field that exists across the well region will force the carriers towards the device contacts. On their way, they will be affected by other scattering processes.

From a simulation point of view, it would be nice if we could include the details of the various scattering processes. From a calculation point of view, however, doing so is a tremendous undertaking. It requires us to solve the time-dependent Schrödinger equation with the various forces represented by extensive (and very complicated) scattering matrices. Even relatively "simple" many-body problems are computationally very intensive to solve. Simplified descriptions that capture the essence of the various processes must be

introduced if we want to model the carrier sweep-out in electroabsorption modulators.

PinSim is a drift-diffusion type model. Drift-diffusion models are very commonly used for modeling of lasers. Our model is semi-classical, in that it describes the absorption and the well carrier-populations using quantum mechanics, but describes all other processes using classical equations. For the various processes involved in the sweep-out of carriers, simple models exist that capture the physics but bypass involved quantum-mechanical descriptions. As an example, high-field carrier transport in a semiconductor is well represented by field-dependent, experimentally determined carrier velocities, and a simple expression for this behavior is used in the simulator.

In the following, we describe the physical picture of the carrier sweep-out on which our model is based. Overall, the picture, instead of being a large scattering problem, is composed of a number of individual particle transport mechanisms. To give an overview of these various transport mechanisms, we describe the fate of a carrier, hole or electron, after it is excited by an optical field.

The density of optically excited carriers depends on the absorption coefficient. The absorption spectrum is calculated by finding the bound states in the electron and hole wells, and then take into account that carriers populate these states to some degree. The absorption is calculated dynamically to take into account that the densities of carriers in the wells vary, and that the field across the wells is affected by the photo-excited carriers.

To ease the description of the model, we will be referring to Fig. 4.1, which shows schematically the energy landscape in a typical p-i-n electroabsorption modulator structure. The figure illustrates the carrier transport and -transition processes that are included in the model. The p-doped region is labeled “p”, the intrinsic (that is, undoped) region is labeled “i”, and the n-doped region is labeled “n”. Carrier generation by optical excitation is indicated by label (G), and carrier recombination is labeled by (R).

When a carrier is excited into a well, it is considered to be localized there until it escapes. The escape from the well (process 1 in Fig. 4.1) proceeds with a rate that depends on a number of dynamical parameters (to which we return later in the chapter), and thus this rate may vary during carrier sweep-out. Carriers above the well (above in an energy sense) may be captured into the well (2). Like the escape rate, the capture rate depends on a number of parameters, and the capture rate may therefore also be subject to change

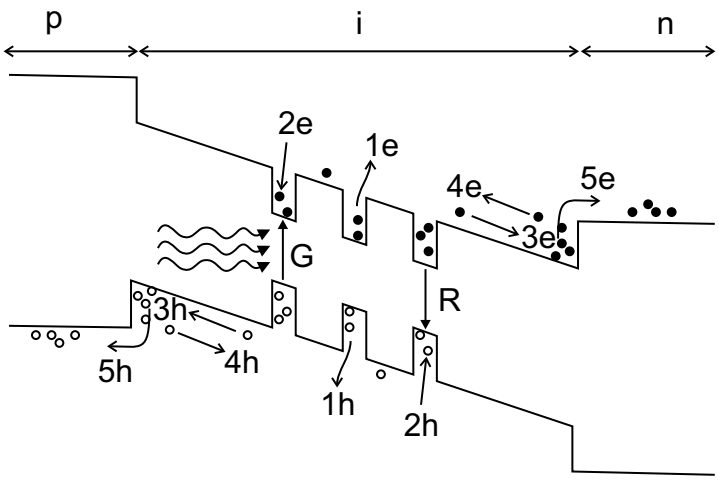

Figure 4.1: Schematic illustration of a semiconductor electroabsorption modulator and the transport mechanisms that are used in PinSim to describe the carrier sweep-out dynamics.

during carrier sweep-out. When a carrier is excited to the continuum above the well, it will be affected by the local electric field. This field is a result of the overall distribution of carriers and of the applied bias. The carrier drifts (3) with a velocity which depends on the local field. Diffusion (4) is a transport process driven by variations in the carrier density. Figure 4.1 indicates that diffusion causes carriers to move toward a higher potential. Although this is the most common situation, diffusion may of course instead contribute a particle current towards a lower potential; the direction of the diffusion current depends on the direction of the carrier density gradient.

If the carrier comes close to a well, there is a probability for it to be recaptured (2). After having passed all the wells, the carrier will move out to the contact, still driven by drift and diffusion. On the way, it may encounter a heterojunction, the energy barrier of which must be overcome (process 5) before the carrier can reach the contact.

The rest of this chapter will present the individual models that are used to describe the sweep-out.

4.2 The drift-diffusion equations

As mentioned above, our model is a drift-diffusion model. This type of model is extremely useful for describing transport in lasers, photodiodes, absorbers, and other similar semiconductor devices. Derived from a linearized Boltzmann equation, the drift-diffusion equations contain a number of driving terms [106, 107]. In our work there are two such terms. One is the so-called *drift* term, which describes carrier motion driven by an electric field. The other term is the *diffusion* term, which describes motion of carriers driven by a gradient in the carrier density. The drift-diffusion equations are central to the present model. In one dimension they are:

$$J_n = e\mu_n nE + eD_n \frac{\mathrm{d}n}{\mathrm{d}x} \qquad \text{(electrons)} \tag{4.1}$$

$$J_p = e\mu_p pE - eD_p \frac{\mathrm{d}p}{\mathrm{d}x} \qquad \text{(holes)} \tag{4.2}$$

The first term in each equation is the drift term, the second term is the diffusion term. The variables that enter are the density of electrons in bulk states in the conduction band, n, the density of holes in bulk states in the valence band, p, the mobilities for electron and holes, μ_ν ($\nu = n, p$), the diffusion constants, D_ν ($\nu = n, p$), and the electric field, E, which is related to the electrostatic potential, ϕ, through

$$E = -\frac{\mathrm{d}\phi}{\mathrm{d}x} \tag{4.3}$$

Equations (4.1)–(4.2) assume that the mass is stepwise constant. If the mass varies continuously then there will be a change in the density of states, and the drift-diffusion equations will contain additional terms. A thorough account of the derivation of such additional terms may be found in [107]. They are not required for the structures that we focus on.

For the diffusion coefficients in Eq. (4.1) and (4.2), we use the *Einstein relations*

$$D_\nu = \frac{kT}{e}\mu_\nu, \quad \nu = n, p \tag{4.4}$$

They result from the derivation of the drift-diffusion equations, assuming thermal equilibrium. The equations are usually taken to valid also away from equilibrium. We adopt this approximation here. Finally, we mention

that equations (4.4) are derived for non-degenerate carrier densities. Lacking information about their dependence on the carrier density, we take them to be valid for all carrier concentrations. Values of $\mu_\nu E$ may be found in Fig. B.1.

4.3 Poisson's equation

The distribution of carriers is related to the electric field through Poisson's equation,

$$-\frac{\mathrm{d}}{\mathrm{d}x}\left(\epsilon(x)\frac{\mathrm{d}}{\mathrm{d}x}\phi\right) = \rho(x), \tag{4.5}$$

which is derived from Maxwell's equations. In Eq. (4.5), ρ is the charge density and ϵ is the permittivity. In a heterostructure, ϵ will vary from one layer to the next. To not obscure things by introducing local variations in the field from changes in the permittivity across the structure, we will assume that ϵ is constant throughout all layers. A value of $\epsilon = 3.6^2\epsilon_0$ will be assumed; ϵ_0 is the vacuum permittivity. This is an acceptable approximation, as the permittivity only changes about 10 % in $\mathrm{In}_{1-x}\mathrm{Ga}_x\mathrm{As}_y\mathrm{P}_{1-y}$, from $y = 0$ to $y = 1$ [108] along the lattice-matched $(y, x(y))$-graph, where

$$x(y) = \frac{0.1896y}{0.4183 - 0.0132y} \tag{4.6}$$

The charge density ρ consists of contributions from free carriers, ionized dopants, and from carriers in the quantum wells:

$$\rho = e(p - n + N_D^+ - N_A^- + p_{\mathrm{QW}} - n_{\mathrm{QW}}) \tag{4.7}$$

in which n_{QW} and p_{QW} are the charge distributions of electrons and holes, respectively, in quantum well states. The densities of ionized donor and acceptor sites are N_D^+ and N_A^-, respectively; e is the electron charge. The density of ionized donor sites is [109]

$$N_{\mathrm{D}}^-(x) = \frac{N_D(x)}{1 + \exp(-\frac{E_c(x) - E_{\mathrm{D}} - \phi(x) - E_{\mathrm{fc}}(x)}{k_{\mathrm{B}}T})} \tag{4.8}$$

where E_{D} is the ionization energy of the donor level in question, and E_{fc} is the electron Fermi level. The density of ionized acceptor sites is

$$N_{\mathrm{A}}^{-}(x) = \frac{N_A(x)}{1 + \exp(\frac{E_v(x)+E_{\mathrm{A}}-\phi(x)-E_{\mathrm{fv}}(x)}{k_{\mathrm{B}}T})} \tag{4.9}$$

where E_{A} is the ionization energy of the acceptor level, and E_{fv} is the hole Fermi level. Taking $N_{\mathrm{A}}^{-}(x) = N_A(x)$ and $N_{\mathrm{D}}^{-}(x) = N_D(x)$ is a good approximation at room temperature, but we use the equations above. The p-doping element in our structures is Zn, and the n-doping element is Si. In InGaAsP the donor ionization energy is $E_{\mathrm{D}} \sim 5$ meV (Sn, Ge, Si, Te, and S doping), and the acceptor ionization energy is $E_{\mathrm{A}} \sim 30 - 38$ meV for Zn doping (Cd: $\sim 30 - 60$ meV, Be: ~ 40 meV, and Mg: ~ 35 meV) [108].

4.4 Continuity equations

The continuity equations for electrons and holes are derived from Maxwell's equations. They state that charge is conserved.

4.4.1 The bulk continuity equations

The current density, J, in a bulk crystal is made up of two contributions: the electron current density, J_n, and the hole current density, J_p:

$$J = J_n + J_p \tag{4.10}$$

Assuming that the density of non-mobile charges (ionized donors and acceptors, and carriers in wells) is time-independent, Maxwell's equations give

$$\nabla \cdot (J_n + J_p) + e\frac{\partial}{\partial t}(p - n) = 0 \tag{4.11}$$

This equation can be split up into an electron equation and a hole equation:

$$\frac{\partial J_n}{\partial x} - e\frac{\partial n}{\partial t} = \quad e(R - G) \tag{4.12}$$

$$\frac{\partial J_p}{\partial x} + e\frac{\partial p}{\partial t} = -e(R - G) \tag{4.13}$$

or

$$\frac{\partial n}{\partial t} = \frac{1}{e}\frac{\partial J_n}{\partial x} - (R - G) \tag{4.14}$$

$$-\frac{\partial p}{\partial t} = \frac{1}{e}\frac{\partial J_p}{\partial x} + (R - G) \tag{4.15}$$

The expressions for J_n and J_p are given by the drift-diffusion equations from Sec. 4.2. R and G are that recombination and generation rates, respectively. In our model the generation rate in the bulk is taken to be zero, that is, $G = 0$.

Near quantum wells, carriers may be exchanged between the bulk states and the well states. $J^{\mathrm{3D}}_{c,\mathrm{QW}}$ is the electron current density from bulk states into the electron wells, and $J^{\mathrm{3D}}_{v,\mathrm{QW}}$ is the hole current density from bulk states into the hole wells. These terms are included into the bulk continuity equations:

$$\frac{\partial n}{\partial t} = \frac{1}{e}\left(\frac{\partial J_n}{\partial x} + J^{\mathrm{3D}}_{c,\mathrm{QW}}\right) - R \tag{4.16}$$

$$-\frac{\partial p}{\partial t} = \frac{1}{e}\left(\frac{\partial J_p}{\partial x} + J^{\mathrm{3D}}_{v,\mathrm{QW}}\right) + R \tag{4.17}$$

$J^{\mathrm{3D}}_{c,\mathrm{QW}}$ and $J^{\mathrm{3D}}_{v,\mathrm{QW}}$ are given by

$$J^{\mathrm{3D}}_{\nu,\mathrm{QW}}(x) = \begin{cases} \dfrac{J^k_{\nu,\mathrm{QW}}}{L^k_{\mathrm{QW}}} & x^k_1 < x < x^k_2 \\ 0 & \text{otherwise} \end{cases}, \quad \nu = c, v \tag{4.18}$$

The well width, L^k_{QW}, and the coordinates, x^k_1 and x^k_2, for the k-th well are defined in Fig. 4.2. The two-dimensional current densities $J^k_{\nu,\mathrm{QW}}$ ($\nu = c, v$) are calculated for each well individually. We return to these terms below, in Sec. 4.4.3.

4.4.2 The quantum-well continuity equations

The continuity equations for the quantum wells are similar to those for bulk material. The change in the well carrier densities with time is accounted for by optical excitation and recombination, and by exchange of carriers between well states and bulk states. For electrons and holes, respectively, in well k:

$$\frac{\partial n^k_{\mathrm{2D}}}{\partial t} = -\frac{1}{e}J^k_{c,\mathrm{QW}} - R^k_{\mathrm{2D}} + G^k_{\mathrm{2D}} \tag{4.19}$$

$$\frac{\partial p^k_{\mathrm{2D}}}{\partial t} = \frac{1}{e}J^k_{v,\mathrm{QW}} - R^k_{\mathrm{2D}} + G^k_{\mathrm{2D}} \tag{4.20}$$

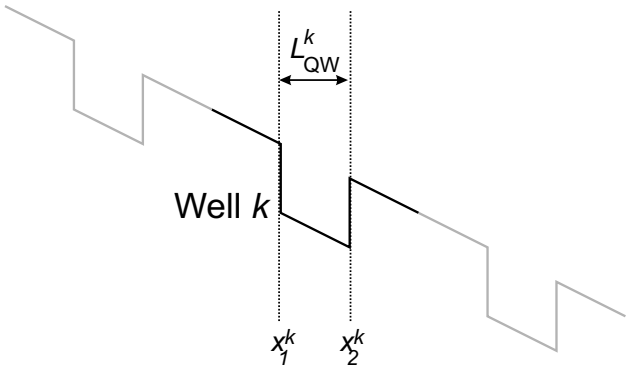

Figure 4.2: Definitions of well width, L^k_{QW}, and the start and end coordinates, x^k_1 and x^k_2, for the k-th well.

Here, n^k_{2D} and p^k_{2D} are, respectively, the electron and hole densities in well k, $J^k_{\nu,\mathrm{QW}}$ are the current densities of electrons ($\nu = c$) and holes ($\nu = v$) between the well states and the bulk states for well k; expressions for these terms may be found in Sec. 4.4.3 below. These terms also appear in the bulk continuity equations (4.16) and (4.17) through the expression in (4.18). R^k_{2D} is the recombination rate for carriers in well k. This term is discussed in Sec. 4.7.2. G^k_{2D} is the generation rate of optically excited carriers in well k and is discussed in Sec. 4.7.1.

4.4.3 Current density between well states and bulk states

The net current density out of a well is determined by a number of processes and parameters. In the simplest model, a constant escape time determines the current density out of the well, and capture is ignored. The escape time in this simple model could be determined experimentally, as in [76], or by using a model for the transport of carriers out of the wells, as in [110].

In general, there may be both an escape current and a capture current, as shown in Fig. 4.3. An important issue with respect to the transport between well and barrier states is: To what degree does capture play a role? We return to a more thorough discussion of this issue in Chapter 5 and Chapter 6. For now, the basic model used in our simulator to describe escape and capture

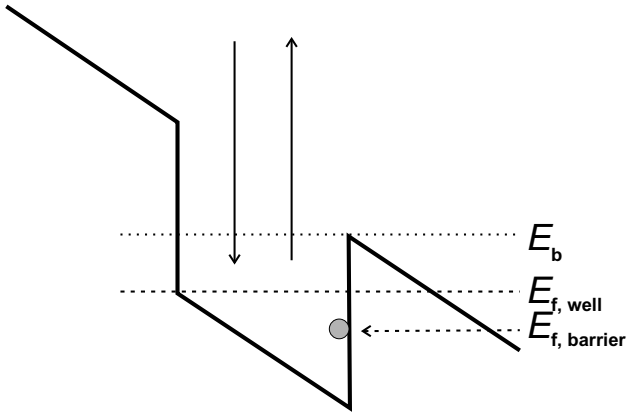

Figure 4.3: Capture to and escape from a quantum-well. The parameters are E_b, the barrier energy; $E_\mathrm{f,well}$, the Fermi level in the well; and $E_\mathrm{f,barrier}$, the Fermi level in the barrier. The grey circle indicates both the barrier Fermi level and the position at which it is measured. The text explains how the current in and out of the well can be related to these parameters.

is presented.

The thermionic model

Based on conventional thermionic emission theory, Schneider *et al.* developed a thermionic emission model to describe the escape of carriers from a quantum well [110]. Thermionic emission is described in more detail in Sec. 4.5. Referring to Fig. 4.3, carriers with energies exceeding the barrier energy E_b will escape from the well and assume a velocity which is related to the carrier's kinetic energy. In the following, the focus is on the electron current density for exemplification. The expressions for the heavy and light hole current densities (and derived parameters) parallel the electron expressions. The expression derived in [110] for the electron current density out of a well is

$$J_{e,\mathrm{QW}}^{\mathrm{out}} = -en^* \left(\frac{k_\mathrm{B}T}{2\pi m_{e,\|}}\right)^{1/2} \exp\left(-\frac{E_\mathrm{b}-E_1}{k_\mathrm{B}T}\right) \tag{4.21}$$

In this expression, $m_{e,\|}$ is the in-plane mass of electrons in the well (see Appendix A), n^* is the carrier density, and E_1 is the lowest-lying quasi-bound state in the well. We use $n^* = n_\mathrm{2D}/L_\mathrm{QW}$ where L_QW is the well width

(cf. Fig. 4.2). Calculated assuming a thermal distribution of carriers, this expression relies on fast carrier-carrier and carrier-phonon scattering. We also note that the expression is derived assuming that only the lowest well state is populated.

Defining the escape time $\tau_{\mathrm{e,2D}}$ through

$$J_{e,\mathrm{QW}}^{\mathrm{out}} = \frac{n_{\mathrm{2D}}}{\tau_{e,\mathrm{2D}}} \tag{4.22}$$

we find

$$\tau_{e,\mathrm{2D}} = \left(\frac{2\pi m_{e,\|} L_{\mathrm{QW}}^2}{k_{\mathrm{B}}T}\right)^{1/2} \exp\left[\frac{E_{\mathrm{b}} - E_1}{k_{\mathrm{B}}T}\right] \tag{4.23}$$

Note that the escape time increases with the in-plane mass. Inserting expression (A.14) for the well density n_{2D}, the current density out of the well is

$$J_{e,\mathrm{QW}}^{\mathrm{out}} = -\frac{e(k_{\mathrm{B}}T/\pi)^{3/2}(m_{e,\|}/2)^{1/2}}{\hbar^2 L_{\mathrm{QW}}} \exp\left(\frac{E_{\mathrm{fe,2D}} - E_{\mathrm{b}}}{k_{\mathrm{B}}T}\right) \tag{4.24}$$

Note that Eq. (A.14) assumes a Boltzmann distribution of carriers.

Carriers may also be captured into the well, that is, scatter from bulk states to well states. This is of course a critical process in quantum-well lasers, where captured carriers provide the gain necessary for lasing to occur. We denote the capture current density by $J_{e,\mathrm{QW}}^{\mathrm{in}}$. In thermal equilibrium, the net current density out of the well,

$$J_{e,\mathrm{QW}} = J_{e,\mathrm{QW}}^{\mathrm{out}} - J_{e,\mathrm{QW}}^{\mathrm{in}} \tag{4.25}$$

is zero. By assuming that the capture rate is proportional to the carrier density in the bulk states, and that the bulk population is non-degenerate, we get the following expression for the capture current density, valid near quasi-equilibrium with no optical excitation:

$$J_{e,\mathrm{QW}}^{\mathrm{in}} = \frac{e(k_{\mathrm{B}}T/\pi)^{3/2}(m_{e,\|}/2)^{1/2}}{\hbar^2 L_{\mathrm{QW}}} \exp\left(\frac{E_{\mathrm{fe,3D}} - E_{\mathrm{b}}}{k_{\mathrm{B}}T}\right) \tag{4.26}$$

A capture time $\tau_{e,\mathrm{3D}}$ can then be found through

$$J_{e,\mathrm{QW}}^{\mathrm{in}} = \frac{n_{\mathrm{3D}}}{\tau_{e,\mathrm{3D}}} L_{\mathrm{QW}} \tag{4.27}$$

Above, we assumed that carriers escape from the well if their energy is above E_{b}, which therefore marks the lowest quasi-continuum energy. The appropriate barrier Fermi level, $E_{\mathrm{fe,3D}}$, is therefore that at the low-energy side of the well, as indicated by the grey circle in Fig. 4.3. Using Eq. (4.25) and the expressions (4.22) and (4.27), we find

$$\frac{n_{\mathrm{2D}}}{\tau_{e,\mathrm{2D}}} = \frac{n_{\mathrm{3D}}}{\tau_{e,\mathrm{3D}}} L_{\mathrm{QW}} \tag{4.28}$$

It is important to note that Eq. (4.26) is derived by assuming that the well population is in equilibrium with the bulk population. Therefore the carrier densities in Eq. (4.28) are really the thermal equilibrium values for the carrier densities with no optical excitation. Well away from equilibrium, Eq. (4.28) is possibly not valid. As mentioned, we return to a more detailed discussion of this issue in chapters 5 and 6. To prepare for this discussion, two terms are defined here that will be used in the following chapters:

Thermionic recapture We use *thermionic recapture* (or *thermionic capture*) to refer to a situation where relation (4.28) is valid also away from equilibrium (note that the densities in (4.28) are the equilibrium densities).

No recapture The term *no recapture* will be used to refer to a situation where the capture term $J^{\mathrm{in}}_{e,\mathrm{QW}}$ in Eq. (4.25) is zero. Thus the net current density out of the well equals the escape current density.

The expressions above for the escape and capture currents are subject to a few further comments. Firstly, the thermionic emission expression for the escape, given in Eq. (4.21), does not take into account the finite scattering time from the sub-band in which carriers are excited, to the quasi-continuum states. Secondly, the same expression does not take into account thermionic emission from excited states in the well. Finally, only escape through thermionic emission is currently included in our simulator. There is also a contribution to the escape current from tunneling of carriers through the well barrier. (Tunneling is described in Sec. 4.5.) Models have been developed that take into account both thermionic emission from excited states and tunneling [79, 80]. However, the contribution from the ground state thermionic emission is typically a good approximation to the total escape rate (see e.g. [79]).

4.5 Current across heterojunctions

A heterojunction is an interface between two different materials, in our case two semiconductors. If the band discontinuity, the *heterobarrier*, is large compared to the thermal energy, carriers on one side will have kinetic energies much below those on the other side. This will cause carriers to pile up at the heterobarrier. Figure 4.4 shows the conduction-band potential near a heterojunction. The current across the barrier from Side 1 to Side 2 is found from the general expression [110][3]

$$J_{1\to 2} = e\int_{-\infty}^{\infty} T(E)v(E)\frac{\mathrm{d}n}{\mathrm{d}E}dE \tag{4.30}$$

in which T is the probability that a carrier with energy E is transmitted across the interface, $v(E)$ is the energy-dependent carrier velocity, and $\mathrm{d}n/\mathrm{d}E$ is the density of states. There is also a current in the opposite direction, with an expression formally identical to Eq. (4.30).

The transmission across the heterobarrier is usually thought of as being made up of two contributions: *Thermionic emission* and *Fowler-Nordheim tunneling*. Both contributions, which are illustrated in Fig. 4.4, are calculated using Eq. (4.30). Thermionic emission is the current of carriers *over* the barrier, whereas Fowler-Nordheim tunneling is the current of carriers *through* the barrier.

4.5.1 Thermionic emission

Wu and Yang [111] generalized the thermionic emission theory known from metals [109] to semiconductors. Thermionic emission is a thermally activated transport mechanism by which carriers with "high energies" cross an energy barrier. (What "high energies" means is defined in Eq. (4.31) below.)

[3] Actually, the more general expression is [111]:

$$J_{1\to 2} = \frac{2e}{(2\pi)^3}\iiint \frac{1}{\hbar}\left(\frac{\partial E}{\partial k_x}\right)\mathrm{d}k_x\,\mathrm{d}k_y\,\mathrm{d}k_z T(E,k_y,k_z)f_1(E(\vec{k}))\left\{1-f_2(E(\vec{k}))\right\} \tag{4.29}$$

In Eq. (4.29), E is the total energy, T is the quantum-mechanical transmission coefficient, and f_i are the distribution functions on the two sides of the junction. Equation (4.30) results when the energy dispersion is assumed to be quadratic and the effective masses isotropic.

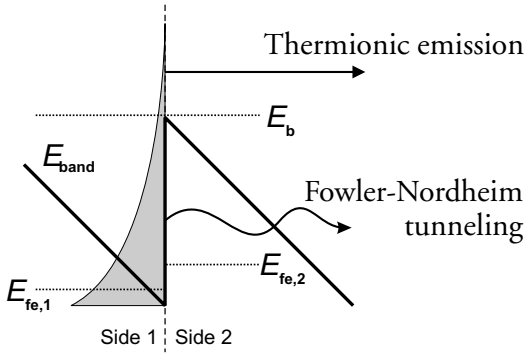

Figure 4.4: Various mechanisms for transport across a heterobarrier. The grey area illustrates a thermal carrier distribution. The mechanisms are: *Thermionic emission*, where thermal carriers with high energies cross the barrier; and *Fowler-Nordheim tunneling*, where thermal carriers having energies lower than the barrier energy cross the barrier by tunneling through it. $E_{\mathrm{fe,i}}$ are the (electron) Fermi levels on the two sides of the junction, and E_b is the barrier energy. E_{band} is the band edge.

The expressions given below for the net current densities across a heterojunction are found by using a classical approximation for the transmission coefficient T in Eq. (4.30):

$$T(E) = \begin{cases} 1 & \text{if } E \geq E_b \\ 0 & \text{if } E < E_b \end{cases} \tag{4.31}$$

According to this approximation a carrier will pass the barrier if and only if its energy is higher than the barrier energy, E_b (see Fig. 4.4). The carrier velocity used in Eq. (4.30) is calculated using a free-carrier expression with a mass that equals the effective mass of that carrier (see Sec. A.0.3).

Electron current

The current density for electrons is given by

$$\begin{aligned} J_{e,\mathrm{th}} &= -\frac{e\eta(m_{\mathrm{e},1}, m_{\mathrm{e},2})(k_{\mathrm{B}}T)^2}{2\pi^2\hbar^3} \\ &\quad \cdot \left[\exp\left(-\frac{E_{\mathrm{b,e}} - E_{\mathrm{fe},1}}{k_{\mathrm{B}}T}\right) - \exp\left(-\frac{E_{\mathrm{b,e}} - E_{\mathrm{fe},2}}{k_{\mathrm{B}}T}\right)\right] \end{aligned} \tag{4.32}$$

Here, $E_{\mathrm{fe},i}$ are the Fermi levels on the two sides of the junction (see Fig. 4.4), $E_{\mathrm{b,e}}$ is the barrier energy for electrons, and $m_{\mathrm{e},1}$ and $m_{\mathrm{e},2}$ are the electron masses on Side 1 and Side 2, respectively. The function η is defined by [112]:

$$\eta(m_1, m_2) = \frac{2}{\frac{1}{m_1} + \frac{1}{m_2}} \tag{4.33}$$

Hole current

The thermionic emission current for holes must be calculated separately for the two hole types because the light and heavy hole masses are different. In case there is strain in the structure (that is, away from the $(y, x(y))$-graph with $x(y)$ given by Eq. (4.6)), the two hole bands will be offset from one another. This offset must be taken into account through the barrier energies. The expression for the hole current density is

$$J_{h,\mathrm{th}} = \sum_{i=\mathrm{hh,lh}} \frac{\eta_i (k_{\mathrm{B}}T)^2}{2\pi^2\hbar^3} \left[\exp\left(\frac{E_{\mathrm{b},i} - E_{\mathrm{fv},1}}{k_{\mathrm{B}}T} \right) - \exp\left(\frac{E_{\mathrm{b},i} - E_{\mathrm{fv},2}}{k_{\mathrm{B}}T} \right) \right] \tag{4.34}$$

$E_{\mathrm{fv,i}}$ are the Fermi levels on the two sides for hole type i, $E_{\mathrm{b},i}$ is the barrier height for hole type i, and η_i is found from Eq. (4.33) using the masses of hole type i from the two sides of the junction.

We will assume that light holes and heavy holes have a common Fermi level (see Sec. A.0.1). Since the heavy hole mass is a factor $\sim$ 4–10 times greater than the light hole mass, the thermionic emission current due to heavy holes will dominate in an unstrained structure.

4.5.2 Fowler-Nordheim tunneling

Fowler-Nordheim tunneling, sometimes also referred to as field-induced tunneling, denotes transport of carriers through a triangular barrier. Such barriers exist at heterojunctions that are located within the intrinsic region. Fowler-Nordheim tunneling is illustrated in Fig. 4.4.

The probability for carrier tunneling increases as the field near the junction increases because the (nearly triangular) barrier through which the carriers must tunnel becomes thinner. Fowler-Nordheim tunneling can give a significant contribution to the current across the barrier. If the temperature is low, the main contribution to transport across the barrier will come from tunneling.

The Fowler-Nordheim tunneling current density is calculated using the classical approximation [113-115]

$$J_{\mathrm{FN}} = BF^2 \exp\left(\frac{-C}{F}\right) \tag{4.35}$$

where B and C are defined as

$$B = \frac{e^3}{16\pi^2\hbar}\frac{m}{m_b} \quad , \quad C = \frac{4}{3}\frac{\sqrt{2m}}{e\hbar}\Delta E_b^{3/2} \tag{4.36}$$

In those expressions, ΔE_b is the energy discontinuity at the junction, F is the field at the high-energy side of the junction, m_b is the mass in the barrier, and m is the mass on the side from which carriers tunnel through the barrier. The derivation of this approximation is lengthy. More details may be found in [116].

4.6 Bound and quasi-bound states

Compared to the situation in a laser, the calculation of the absorption spectrum in a modulator structure is complicated by the presence of a non-zero field. The potential across a well in a conventional quantum-well laser structure is shown in Fig. 4.5 (*solid line*). It is stepwise flat and includes a region of lower energy, the "well". States with energies below the barrier energy are bound, their lifetimes are infinite, and their eigenenergies are separated by a finite amount from the eigenenergies of all other eigenstates.

In a typical modulator there is a high field across a wide region that includes the wells. In this case, only quasi-bound states exist in the wells; there are no real bound states. Thus a carrier in the well will eventually tunnel out. Equivalently, there is a non-zero probability of finding a carrier, which is in one of those states, "far" away from the well. Associated with the non-zero tunneling probability is a finite lifetime (as discussed in [117]).

4.6.1 Two field regimes

Before discussing the approach used in the simulator to calculate the well states, we wish to discuss two different field regimes, the low-field regime and the high-field regime, and the problem of accounting properly for the well states in the high-field regime.

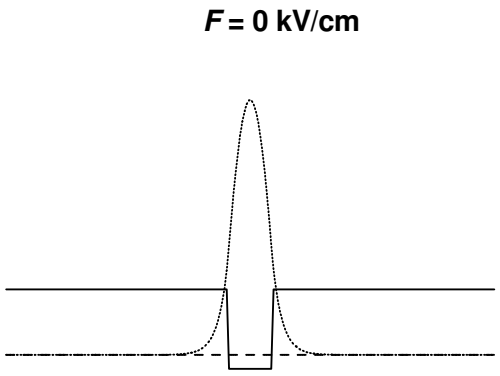

Figure 4.5: The *solid line* shows the potential at field $F = 0$ kV/cm. The *short-dashed line* shows the wavefunction for the first bound state in the well, calculated using the simulator, and the *dashed line* shows the corresponding eigenenergy.

The low-field regime

In the low-field regime, the field F across the well is low enough that[4]

$$eF\kappa_c^{-1} < E_b - E_1^{(0)} \tag{4.37}$$

κ_c is the wavevector in the barrier, E_b is the barrier energy, and $E_1^{(0)}$ is the energy of the lowest bound state at zero field [118]. This is shown schematically in Fig. 4.6. Relation (4.37) states that the potential drop within the extent of the low-energy-side tail of the wavefunction for the lowest bound state is small compared to the confinement energy of the state at zero field, which is given by $E_b - E_1^{(0)}$. In short, the state hardly experiences changes in the potential outside the well.

Figure 4.7 shows the well from Fig. 4.5, but now with a field F=42 kV/cm across it. The corresponding wavefunction is strictly speaking not bound, but because it nearly goes to zero within both barriers, the situation is very similar to that in Fig. 4.5. Because of the high degree of confinement, formalized

[4]The relation is a qualitative condition; there is not a sharp line between the low- and high-field regimes.

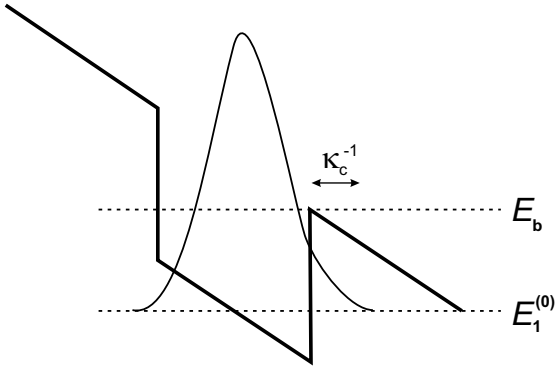

Figure 4.6: Illustration of the low-field regime, defined by the relation (4.37). The field is low enough that the lowest lying bound state does not 'feel' other changes in the potential than those inside the well.

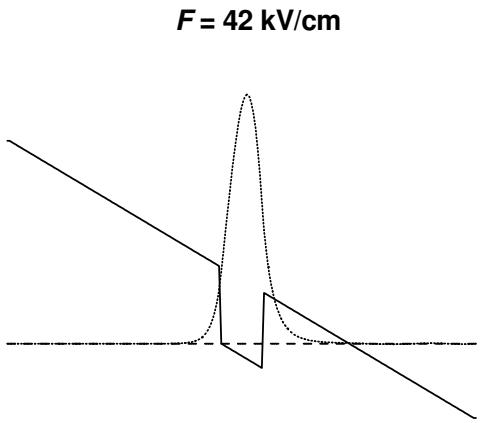

Figure 4.7: The *solid line* shows the potential at field $F = 42$ kV/cm. The *short-dashed line* shows the calculated wavefunction, and the *dashed line* shows the corresponding eigenenergy. As the wavefunction is well confined to the well (cf. Fig. 4.5), the state may still be considered 'bound' at this field, although strictly speaking it is only quasi-bound. Note that the wavefunction is slightly skewed towards the low-energy side.

by Eq. (4.37), the life-time of the state is long and, as in the zero-field situation, the well and barrier states are well separated in energy and their properties are vastly different. The well states are almost entirely confined to the well, as illustrated in Fig. 4.7, whereas all other states are extended in nature. These other states are well approximated by *Airy functions*.[5] This distinction between well states and bulk states means that the concept of separate 2D and 3D states is valid, and the low-field regime can be characterized by the existence of a well-defined density of states for the well. For a given carrier density in the well, it is possible to find the Fermi level for those carriers, together with their spatial distribution.

With well-defined and distinguishable 2D and 3D states, a number of models exist that describe the transport between the well and the bulk states. These models describe transport mechanisms such as thermionic emission (described earlier in this chapter) and phonon-assisted tunneling [91, 119, 110, 75, 79, 80].

The high-field regime

The distinction between the low-field regime and the high-field regime is not a well-defined one. However, around a field F defined by[4]

$$eF\kappa_c^{-1} = E_b - E_1^{(0)} \tag{4.38}$$

the distinction between the well and barrier states starts to be washed out. The field is now so high that the *at zero field lowest-lying well state* no longer is confined to the well, as the barrier is too thin to contain it. This is shown schematically in Fig. 4.8 and by a calculation in Fig. 4.9. Figure 4.9 shows the same well as in Fig. 4.5 and Fig. 4.7, but now subject to field $F = 61$ kV/cm. The wavefunction penetrates the low-energy-side barrier, and a significant part of the wavefunction is outside the well. At higher fields, this is even more pronounced. The situation is fundamentally different from that in Fig. 4.5 and Fig. 4.7. The distinction between well and bulk states can no longer be made, as the qualitative nature of all states is the same, namely, they are extended. Some states may have a larger probability concentration near the well than other states, but still, no clear physical distinction can be made.

This lack of distinction introduces a host of problems in relation to our model. The physical models that are applicable in the low-field regime — they

[5] The Airy functions are solutions to the Schrödinger equation in a constant, non-zero field [5]. The presence of the well perturbs these functions slightly.

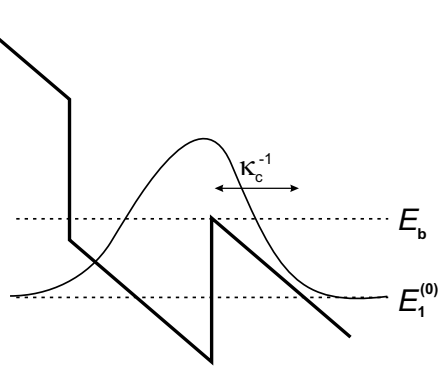

Figure 4.8: Illustration of the high-field regime, defined by the relation (4.38). The field is now so high that the at zero field lowest lying bound state now penetrates the low-energy-side barrier, and therefore no longer can be considered bound.

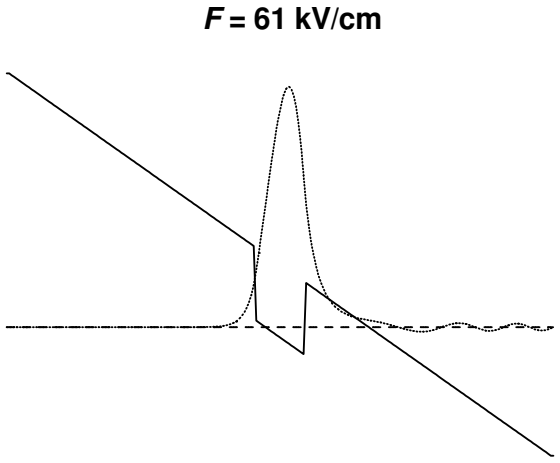

Figure 4.9: The *solid line* shows the potential at field $F = 61$ kV/cm. The *short-dashed line* shows the calculated wavefunction, and the *dashed line* shows the corresponding eigenenergy (*dashed*). The field is now so high that a significant part of the wavefunction is outside the well.

are mentioned above in our discussion of that regime — are not immediately useful in the high-field regime. It is of course possible to find the escape rate by applying a more general description of the scattering processes. Such a description may be found for instance in [93]. However, as discussed in the beginning of Sec. 4.1, it is extremely involved and numerically very intensive, and its interpretation is difficult to tie together with our rather classical description in which carriers have definite positions.

There is no *general* description of transport of carriers out of the wells short of the full quantum-mechanical description. In the following section, we therefore describe how we approximate the wavefunctions in the high-field regime in order to be able to apply the models known from the low-field regime.

4.6.2 Our well concept

In the common picture of optical excitation in electroabsorption modulators, carriers are excited into confined well states from which they then escape. Thus, the picture assumes that for each well there is a set of localized states that are separated from the bulk states. This distinction allows us to find a separate Fermi level *for each well*, which means that we will be in a position to use the methods described above for calculating the escape of carriers out of each well, and to calculate the spatial distribution of the carriers in the wells. We use this picture in the present work. Wanting to consider the wells individually, we divide the well region into individual cells in the manner illustrated in Fig. 4.10. The potential is put to infinity at the interfaces between wells, and the bound(!) states for each of these special potentials are found. This approach has been used extensively in modeling of absorption spectra and escape times from quantum wells in an electric field [4, 120, 121]. A comparison between a similar approach and an analytical approach is presented in [122]. The approach is also well known from laser simulators, also when a field is present [91, 93]. The more confined the states are, the better will the approximation we make by dividing the wells in this way be. This implies that the approximation is better at lower fields.

In PinSim, eigenstates ψ_n and eigenenergies ε_n are found by solving the single-particle Schrödinger equation in the envelope approximation:

$$\left[-\frac{\hbar^2}{2}\frac{\mathrm{d}}{\mathrm{d}x}\left(\frac{1}{m_\perp(x)}\frac{\mathrm{d}}{\mathrm{d}x}\right)+V(x)\right]\psi_n(x)=\varepsilon_n\psi_n(x) \tag{4.39}$$

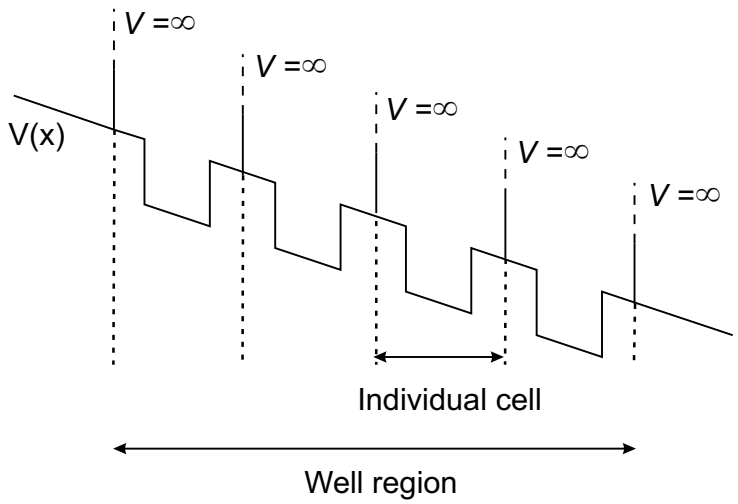

Figure 4.10: Illustration of the well region. The dashed lines illustrate how the wells are separated into individual cells in the calculation of bound states. At these dashed lines, the potential is put to infinity.

for each well using for the potential V the special potential described above. In Eq. (4.39), $m_\perp$ is the mass in the growth direction (see Sec. A.0.3), and $\hbar$ is Planck's constant. The exchange-correlation potential (which gives rise to bandgap renormalization) and Coulomb interaction (which gives excitonic states) are not included.

The states found using this method are technically all bound because they are eigenstates with respect to the special potential functions described above. This means that coupling between wells, which is the basis for Wannier-Stark modulators [123], but also influences strongly the absorption in electroabsorption modulator structures with shallow wells and/or narrow barriers, cannot immediately be calculated with this model.

Although it is necessary to divide the well region into individual wells when we solve the combined Poisson equation/continuity equations/Schrödinger equation problem, PinSim can also be used to calculate separately the absorption spectra. This is done by using the potential for the entire well region instead of dividing it as described above. Examples of such calculations are reported in Chapter 5.

Equation (4.39) is used for all the bands. This means that coupling be-

tween the various bands, which is mostly important for the valence bands, is not taken into account. To include this coupling one could resort to $\boldsymbol{k} \cdot \boldsymbol{p}$ theory, which is discussed for non-zero fields in [124, 125]. A general description of the $\boldsymbol{k} \cdot \boldsymbol{p}$ method may be found in [126, 127]. The coupling between the bands results in changes in the density of states. These changes, which may be substantial, are used extensively in the design of modern lasers to increase the differential gain, to suppress TE versus TM mode competition, and to lower the transparency density [128], among other purposes.

Generalizing the well concept to the high-field regime

When the confinement energies for the well states are high, the eigenstates that we find by dividing the wells into individual cells as illustrated in Fig. 4.10 will be good approximations to those which would be obtained had we used the undivided well-region potential. This conclusion derives from the discussion in Sec. 4.6.1. When the field comes near that defined by Eq. (4.38), the approximation starts to fail, and becomes progressively worse as the field is increased. We need a way of finding the well states, which allows a consistent treatment independent of how "bound" the states are. The only approach that retains the single-well picture (discussed on page 57) is the individual-cell approach. Thus, we will use this approach to calculate the well states without regard to the size of the electric field. This approximation must of course be kept in mind when Eq. (4.37) is violated. In effect, the individual-cell approach circumvents the problems in the high-field regime by approximating the real states with states that are bound to the well. The individual-cell calculation will introduce a separation between 2D and 3D states that allows us to apply, for all fields, the physical interpretation and the models discussed in Sec. 4.6.1.

These issues are rarely discussed when calculated carrier escape times are presented in the literature (e.g. [78, 79]), despite that the approaches in essence have been equal to our approach and thus subject to the same considerations. Lefebvre *et al.* improved in [80] the approach to calculating escape times presented in previous papers [78, 79], by improving the calculation of the density of states [129]. The correspondence between measurements and calculations in Lefebvre *et al.*'s report is astounding, with an almost exact quantitative correspondence between calculations and measurements within the range of concern in the paper, from 10 kV/cm up to 100 kV/cm. In the entire range from 40 kV/cm to 80 kV/cm, the discrepancy is within only

a few percent. This is a large improvement over the calculations presented in [78, 79]. However, Lefebvre *et al.*'s calculations did not include excitonic-state absorption and did not take into account valence band mixing, both of which modify the density of states. A simple effective mass was used for the sub-band dispersion, which was assumed to be quadratic. Finally, a hard line between 2D and 3D carriers was drawn when the escape times were calculated, and the description therefore retains some of the problems we described above. Since no sensitivity analysis was presented, it is difficult to see whether the improved density-of-states calculation alone is responsible for the very impressive quantitative correspondence, or if only the qualitative correspondence is improved and the quantitative correspondence presented in the paper is more of a coincidence. However, there is little doubt that the method presented by Lefebvre *et al.* provides improvements over previous, simpler approaches.

We mention the papers by Lefebvre *et al.* [80, 129] to point out that methods with improved physical content regarding the 2D-to-3D transition at higher fields exist. It is certainly worthwhile to investigate these methods and to consider implementing them in a simulator such as ours.

4.7 Absorption and recombination

The absorption spectrum obviously has a very central place in the discussion of absorptive modulators. The light transmission through an electroabsorption modulator is modulated by inducing changes in the absorption coefficient, either electrically or optically.

4.7.1 Absorption

The absorption spectrum is calculated using the states found as described in Sec. 4.6. The *modal* absorption spectrum for each well is calculated as a sum of contributions from transitions between hole states and electron states. For well k,

$$\alpha^{(k)}_{\text{modal}}(\hbar\omega) = \sum_{i,j} \alpha^{(k)}_{ij}(\hbar\omega)\,\Theta(\hbar\omega - (E^{(i)}_c - E^{(j)}_v)) \tag{4.40}$$

The term "modal" is used because this is the absorption coefficient that an optical mode will experience. The indices denote electron state i, with

eigenenergy $E_c^{(i)}$, and hole state j, with eigenenergy $E_v^{(j)}$. Θ is the Heaviside function.[6] In the equation above, the well index k only appears on the absorption coefficients, not on the other constituent parameters. However, those parameters may vary from one well to the next. The eigenenergies above, for instance, may vary because of field variations across the well region. We continue to use the notation of leaving out the well index on parameters other than the absorption coefficient, up until Eq. (4.48).

The contribution α_{ij} from the transition from hole state j to electron state i is, assuming parabolic sub-bands [128, 130]:

$$\alpha_{ij}^{(k)}(\hbar\omega) = \frac{1}{\hbar\omega}\frac{\pi e^2\hbar}{\epsilon_0 c m_0^2 n} M^2 \frac{m_r}{2\pi\hbar^2} \frac{|\langle F_i|A|G_j\rangle|^2}{|\langle A|A\rangle|}(1 - f_c - f_v) \tag{4.41}$$

F_i is the normalized electron wavefunction, G_j is the normalized hole wavefunction, $A\hat{\boldsymbol{e}}$ is the vector potential for the optical field ($\hat{\boldsymbol{e}}$ is a unit vector), and M^2 is the square of the momentum matrix element.[7] The last term in the expression accounts for the occupation probability of carriers in the conduction band, f_c, and in the hole band, f_v:

$$f_c = \frac{1}{1 + \exp(\frac{E_c - E_{\mathrm{fc}}}{k_{\mathrm{B}}T})} \qquad f_v = \frac{1}{1 + \exp(\frac{E_v - E_{\mathrm{fv}}}{k_{\mathrm{B}}T})} \tag{4.43}$$

E_{fc} and E_{fv} are the well Fermi levels for electrons and holes, respectively. Furthermore,

$$E_c = E_c^{(i)} + \frac{m_r}{m_{\mathrm{e},\|}}\left[\hbar\omega - \left(E_c^{(i)} - E_v^{(j)}\right)\right] \tag{4.44}$$

$$E_v = E_v^{(j)} + \frac{m_r}{m_{\mathrm{th},\|}}\left[\hbar\omega - \left(E_c^{(i)} - E_v^{(j)}\right)\right] \tag{4.45}$$

[6] The Heaviside function is defined as:

$$\Theta(x) = \begin{cases} 0 & x \le 0 \\ 1 & x > 0 \end{cases}$$

[7] The square of the momentum matrix element is given in terms of the Bloch function parts of the Bloch waves that are solutions to the Schrödinger equation in the periodic crystal potential. If $u_{c,i}$ is the Bloch function part of the eigenstate i and $u_{v,j}$ is the Bloch function part of the eigenstate j (referring to the states mentioned in the text), then

$$M^2 = |\langle u_{c,i}|\hat{\boldsymbol{e}}\cdot\boldsymbol{p}|u_{v,j}\rangle|^2 \tag{4.42}$$

where $\boldsymbol{p}$ is the momentum operator.

More details may be found in textbooks on the subject, such as [128].

The mass, m_r, for the reduced density of states is

$$m_r = \left(\frac{1}{m_{\mathrm{e},\|}} + \frac{1}{m_{t\mathrm{h},\|}} \right)^{-1} \tag{4.46}$$

where $m_{e,\|}$ is the in-plane electron mass, and $m_{t\mathrm{h},\|}$ is the in-plane hole mass, either light (t =l) or heavy hole (t =h), depending on the hole type of eigenstate j above. The light and heavy holes are assumed to have the same Fermi level (see Sec. A.0.2).

The absorption coefficient for a well depends on the field across the well through the quantum-confined Stark effect. Because we calculate the absorption coefficient for each well dynamically, taking into account the instantaneous field across it, this effect is included.

Excitonic absorption

Excitonic absorption is not included in the absorption spectrum, which means that what we are calculating is really the so-called *quantum-confined Franz-Keldysh effect*, as defined in [5]. The quantum-confined Franz-Keldysh effect is the electroabsorption effect that would result if there were no excitons. This is of course a purely theoretical conception because excitons always are present. If the contribution to the absorption from excitonic states is small, the quantum-confined Franz-Keldysh effect will approximate the quantum-confined Stark effect well. Since the excitonic absorption increases the field-induced absorption change (the absorption edge is steeper in the presence of excitons), leaving out this contribution results in an underestimation of the absorption change. Our absorption calculations and absorption change calculations are therefore conservative.

In our model, excitonic absorption would have to be included in a parameterized form. It is not difficult to include this contribution, but doing so would have contributed to a clouding of the underlying dynamics, and we leave it out for the calculations in this work.

The parameterization of the excitonic absorption was introduced by Elliot [131]. As an example, Stevens *et al.* applied this theory in to model absorption spectra [120]. Sugawara *et al.* gave a nice summary as well as an interesting theoretical and experimental study of excitonic absorption [132]. Campi *et al.* have generalized the Elliot's theory [133].

Material absorption

The absorption calculated by Eq. (4.40) is the absorption coefficient that an optical field with vector potential $A\hat{\boldsymbol{e}}$ will experience.

We will assume that A is constant across the entire well region. In this case, Eq. (4.40), the single-well *modal* absorption, can be written as

$$\alpha^{(k)}_{\text{modal}}(\hbar\omega) = \Gamma^{(k)}\alpha^{(k)}_{\text{mat}}(\hbar\omega), \tag{4.47}$$

where

$$\alpha^{(k)}_{\text{mat}}(\hbar\omega) = \sum_{i,j} \frac{1}{L^k_{\text{QW}}}\frac{1}{\hbar\omega}\frac{\pi e^2\hbar}{\epsilon_0 c m_0^2 n} M^2 \frac{m_r}{2\pi\hbar^2} |\langle F_i|G_j\rangle|^2 (1 - f_c - f_v) \cdot \Theta(\hbar\omega - (E^{(i)}_c - E^{(j)}_v)) \tag{4.48}$$

is the so-called *material absorption*, and

$$\Gamma^{(k)} = \frac{A^2_{\text{well}} L^k_{\text{QW}}}{|\langle A|A\rangle|} \tag{4.49}$$

is the so-called *confinement factor*. The material absorption describes the actual absorption coefficient of the material. For an optical mode, not all of the field overlaps the absorbing region; the confinement factor is equal to the fraction of the mode that does. In eqs. (4.48)–(4.49), A_{well} is the magnitude of the vector potential in the well region. We will mostly be reporting *material* absorption coefficients when we present our results in the following chapters.

Relation between intensity and power level

In our calculations, we use the intensity at the wells to characterize the power level. In an experiment, an optical spot with some intensity profile is focused onto the device. In the following, we will find a relation between these two power levels. To derive this relation, we use the spot shown in Fig. 4.11 to represent the light spot used in the experiment. The spot in Fig. 4.11 is uniform in the plane of the quantum wells. The width of the spot in this direction is w. In reality, the spot is approximately round and has a Gaussian intensity profile. We use the uniform approximation in the y-direction to simplify the power calculation below. In the growth direction

(x), we use the profile of the waveguide mode (see e.g. [105]). The intensity, defined within the mode area shown in Fig. 4.11, is

$$I(x,y) = \phi_m(x) \cdot I_w(y) \tag{4.50}$$

I_w is the power per length in the y-direction and $\phi_m(x)$ is the mode profile in the growth direction. It is normalized such that $\phi_m|_{\text{well region}} = 1\ \text{m}^{-1}$ (as mentioned, the field is assumed to be uniform across the well region). From Eq. (4.50) the power level can be found as

$$P = \iint I(x,y)\,\mathrm{d}(x,y) = I_w w \frac{\int \phi_m(x)\,\mathrm{d}x}{\int\limits_{\text{well}} \phi_m(x)\,\mathrm{d}x} \int_{\text{well}} \phi_m(x)\,\mathrm{d}x \tag{4.51}$$

$$= I_w w \frac{L_{\text{QW}}^k}{\Gamma^{(k)}} \cdot 1\,\text{m}^{-1} \tag{4.52}$$

$$= I_{\text{peak}} \frac{w \cdot L_{\text{QW}}^k}{\Gamma^{(k)}} \tag{4.53}$$

These expressions require some explaining. The limits denoted 'well' signify a single well, not the entire well region. The unit of I_w is W/m and for ϕ_m it is m^{-1}. Because we have assumed that ϕ_m is constant across the wells, the last

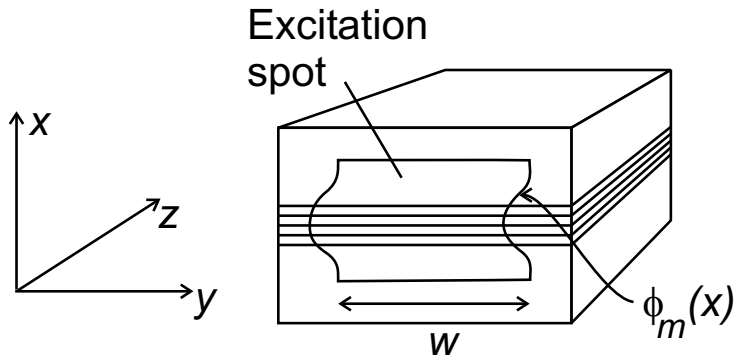

Figure 4.11: Schematic illustration of a quantum-well device under excitation by an optical spot. The illustrated spot is an approximation to a typical spot used in an experiment. This simple approximation enables us to relate the optical intensity at the wells to the power level of the optical spot used to excite the structure in the experiment.

integral in Eq. (4.51) is $L_{\mathrm{QW}}^{(k)} \cdot 1\,\mathrm{m}^{-1}$. Finally, we have defined $I_{\mathrm{peak}} = I_w \cdot 1\,\mathrm{m}^{-1}$. This is the maximum intensity across the spot. In the simulator, we use I_{peak} as the input parameter for the optical excitation power. This is the natural parameter to use because it ensures that the excitation intensity at the wells is independent of the device structure.

Finally, we mention that the equation above does not and should not include the number of wells. The relation between the power level and the intensity at one well, given by Eq. (4.53), is independent of how many wells the structure has, because we have assumed that the intensity across the entire well region is constant. Even if the wells are different, we need only calculate the power using one of the wells. Any well will give the same result because the confinement factor is approximately proportional to the well width.

As an example, for an intensity of 100 kW/cm^{-2}, a confinement factor $\Gamma^{(k)} = 0.02$ (per well), $L_{\mathrm{QW}}^{k} = 10$ nm and $w = 4.5$ μm, Eq. (4.53) gives a spot power level of ≈ 2.3 mW. We use $w = 4.5$ μm and $\Gamma^{(k)} = 0.02$ when we relate the intensity to the spot power.

The stimulated gain term G_{2D} for well k appearing in Eq. (4.19) and (4.20) is given by

$$G_{\mathrm{2D}}^{k} = -\alpha_{\mathrm{mat}}^{(k)} L_{\mathrm{QW}}^{k} v_g S \tag{4.54}$$

where S is the photon density in the well region. The photon density is related to the intensity by

$$S = \frac{I_{\mathrm{peak}}}{v_g \cdot \hbar\omega} \tag{4.55}$$

The absorption of an optical field is determined by

$$\frac{\mathrm{d}S}{\mathrm{d}t} = -\left[\sum_{\mathrm{wells},k} \alpha_{\mathrm{modal}}^{(k)}\right] v_g S \tag{4.56}$$

4.7.2 Recombination models

Besides the stimulated absorption, there are a number of recombination processes that contribute to the dynamics. Although we model effects on a time scale significantly shorter than the characteristic recombination times, and although the carrier densities generally are much below those found in lasers, we include the recombination terms for generality.

Spontaneous recombination

Spontaneous recombination is calculated as [105]

$$R^{\mathrm{3D}}_{\mathrm{spon}} = B(n - n^{\mathrm{th}})(p - p^{\mathrm{th}}) \tag{4.57}$$

where $B = 1 \cdot 10^{-12}$ cm^3/s is used for InGaAsP [134]. (Lower values may also be found in the literature [135].) The variables n^{th} and p^{th} are the carrier densities at thermal equilibrium.

For quantum wells we use a similar expression [135]:

$$R^{\mathrm{2D}}_{\mathrm{spon}} = B^{\mathrm{2D}}(n - n^{\mathrm{th}})(p - p^{\mathrm{th}}) \tag{4.58}$$

B^{2D} is the two-dimensional recombination parameter [130]:

$$B^{\mathrm{2D}} = \sum_{i=\mathrm{l,h}} \frac{e^2 n}{\pi c^3 \hbar^2 \epsilon_0 m_0^2} \bar{M}^2 (\rho_c + \rho_{i\mathrm{h}})^{-1} (k_{\mathrm{B}} T)^{-1} \tag{4.59}$$

with

$$\rho_c = \frac{m_{e,\|}}{\pi \hbar^2} \quad , \quad \rho_{i\mathrm{h}} = \frac{m_{i\mathrm{h},\|}}{\pi \hbar^2} \tag{4.60}$$

The expression (4.59) assumes non-degenerate carrier densities. The sum is over the lowest lying heavy-hole state and the lowest-lying light hole state.

Shockley-Read-Hall recombination

The so-called Shockley-Read-Hall recombination is caused by impurities in the crystal. These impurities introduce in-gap states which act as recombination centers. Recombination can occur substantially faster through these states than through spontaneous recombination. Typically, Shockley-Read-Hall recombination dominates the total recombination, and in much numerical work this is the only recombination term which is included.

The Shockley-Read-Hall recombination rate is given by [136]:

$$R^{\mathrm{3D}}_{\mathrm{SRH}} = \frac{np - n^{\mathrm{th}} p^{\mathrm{th}}}{\tau_n (p + p^{\mathrm{th}}) + \tau_p (n + n^{\mathrm{th}})} \tag{4.61}$$

A typical value for both τ_n and τ_p in InGaAsP is 10 ns [137, 135]. We have not found references on Shockley-Read-Hall recombination in quantum-wells, so we use a similar expression:

$$R_{\mathrm{SRH}}^{\mathrm{2D}} = \frac{n_{\mathrm{2D}} p_{\mathrm{2D}} - n_{\mathrm{2D}}^{\mathrm{th}} p_{\mathrm{2D}}^{\mathrm{th}}}{\tau_n (p_{\mathrm{2D}} + n_{\mathrm{2D}}^{\mathrm{th}}) + \tau_p (n_{\mathrm{2D}} + n_{\mathrm{2D}}^{\mathrm{th}})} \tag{4.62}$$

with the same values for τ_n and τ_p. It is clear that for a wide well, such an expression will be valid (which is true for all types of recombination). Our assumption is that it is valid for any well width.

Auger recombination

An Auger recombination process involves three carriers. A number of three-carrier combinations are possible. For example, in the CCCH Auger process, an electron in the conduction band is excited into a higher conduction-band state and at the same time an electron recombines with a hole. In the CHHS process the conduction-band to conduction-band transition in the CCCH process is replaced by a split-off to heavy-hole transition.

It is common to approximate the Auger recombination rate by using the electron density only:

$$R_{\mathrm{Aug}} = C n^3 \tag{4.63}$$

In [137], this relation shows good correspondence with measurements on lasers, and it seems to be generally accepted [135]. We use a symmetrical version of this expression because the electron and hole densities may be very different in modulators:

$$R_{\mathrm{Aug}}^{\mathrm{3D}} = C^{\mathrm{3D}} (n^3 + p^3) \tag{4.64}$$

The values for C^{3D} in the literature vary substantially, see e.g. [137, 135, 134]. We will use $C^{\mathrm{3D}} = 1 \cdot 10^{-28}$ cm^6/s based on [134].

For quantum wells, we use a similar expression:

$$R_{\mathrm{Aug}}^{\mathrm{2D}} = C^{\mathrm{2D}} (n^2 + p^2) \tag{4.65}$$

with the two-dimensional Auger coefficient $C^{\mathrm{2D}} = 1 \cdot 10^{-16}$ cm^4/s based on [138].

4.8 Band line-up

The issue of band line-up is an extremely important one. It concerns how the electron and hole bands line up when one material is grown on top of another. The line-up determines what values of ΔE_c, ΔE_{hh}, and ΔE_{lh} result at the heterointerface between two such materials.

There is much dispute about this issue. A number of models exist, some of which give quite different results. Reference [139] contains references to a number of important papers in the field.

Two models are considered in the present work. We will mention which model is used when simulations are presented in the following chapters. The choice of model significantly influences the dynamical properties. This is especially true for the transport out of the wells, which depends strongly on the well depths (see Eq. (4.23)).

4.8.1 Band offset model 1: Constant-offset line-up

In this model, the ratio between the conduction-band offset and the valence-band offset is constant:

$$\frac{\Delta E_c}{\Delta E_v} = k \tag{4.66}$$

A typical value for k for InGaAsP is 40/60 [140, 119]. Slightly lower values have also been used [141]. If the structure is strained, the hole bands are modified as described for instance in [142]. Models with constant band-offset ratios are based on early, empirical data. Constant-offset models probably survive because of their simplicity, and because they provide practical rules of thumb. The 70/30-split used for the InGaAs/InAlAs system (see e.g. [140]) is another example of a long-lived constant-offset model. We include the constant-offset model because it has been very widely used and therefore deserves attention also in a modeling context.

4.8.2 Band offset model 2: Tersoff line-up

The Tersoff line-up model is based on the idea that a dipole exists at the interface between two semiconductor materials. The band line-up is directly related to the dipole, and will arrange in a way that makes the dipole vanish [143]. The parameterization of the model used in our work is based on

[144].[8] We will not write it down here because the calculation is unpleasantly lengthy. We refer the reader to [144]. The input to the model, apart from the material-specific band parameters, is the alloy parameters x and y of $In_{1-x}Ga_xAs_yP_{1-y}$.

The Tersoff line-up model has proven useful for understanding the absorption in strained structures similar to ours [145]. In Chapter 5, we show that the model also helps us understand absorption spectra measured on our own samples.

An empirical model based on linear interpolation of the band offsets for binary materials may be found in [139]. The results from this model are very similar to those of Tersoff's model [139]. Recently, a thorough review on the subject appeared with a compilation of the band parameters and line-ups for the technologically most important III-V semiconductors and their alloys [146].

4.9 Other effects

Field-induced carrier heating

Acceleration of carriers in a field leads to an increase in carrier temperature. The description of carrier temperature dynamics requires a set of equations that account for the carrier energy densities [72, 147, 148]. We have not included such equations in our model.

The carrier temperature affects the mobility, which decreases when the carrier temperature goes up. Thus we might underestimate the transport times to the contacts. However, because we use a field-dependent mobility, the effect of heating on the transport *is* taken into account, indirectly. An increase in carrier temperature will lead to an increase in the escape current density from the wells, as may be seen from Eq. (4.24). This effect can only be included once the carrier energy densities are properly described.

Two-photon absorption

Our model does not account for two-photon absorption. Carriers excited by absorption of two photons at a time cause heating of the carrier population. It

[8] K. Yvind is kindly acknowledged for providing the background information and the parameterization of the Tersoff line-up model.

has been shown that two-photon absorption causes significant carrier heating in InGaAsP quantum-well amplifiers [149] excited by short pulses, 200-fs wide, with energies above ≈ 1 pJ. Especially electrons are heated, due to their low mass, and their temperature can be many hundreds or even thousands of degrees [149].

The probability for absorption of two photons at a time requires high photon densities. As it starts to be important at pulse energies above ≈ 1 pJ for pulse widths below a few hundred femtoseconds, we have not included it here. Including it would also require us to incorporate the energy density equations mentioned above.

Bandgap renormalization

Bandgap renormalization was investigated using the model from [119]:

$$\Delta E_g = -\Delta E_g^0 \cdot \left(\frac{\sigma_n n + \sigma_p p}{10^{24}\ \mathrm{m}^{-3}}\right)^\gamma \tag{4.67}$$

with $\sigma_n = 0.3$, $\sigma_p = 0.7$, $\Delta E_g^0 = 0.015$ meV, and $\gamma = 0.4$ [119]. The highest densities of photo-excited carriers in our simulations are around $1 \cdot 10^{23}$ m^{-3} (in single calculations on excitation by highly energetic pulses, the carrier density reaches $\sim 1 \cdot 10^{24}$ m^{-3}). A density of $1 \cdot 10^{23}$ m^{-3} will induce a change in the bandgap of about 6 meV, or 12 nm at 1.55 μm. The well properties have a large influence on the bandgap change, as demonstrated for instance in [150]. Lacking a general formula that takes into account the well width, depth, and composition, and due to the relatively small size of the change calculated above, we have not included bandgap renormalization in our calculations. The issue of bandgap renormalization is important, and once a reliable model is found, it should be included in place of Eq. (4.67).

4.10 Boundary conditions

In the simulator, the electrostatic voltage across the structure, from contact to contact, is kept fixed. Furthermore, we assume that the electron and hole Fermi levels are equal at the boundaries of the structure, that is, that electrons and holes are in thermal equilibrium at the boundaries:

$$E_{\mathrm{fv}}(x = 0) = E_{\mathrm{fc}}(x = 0) \tag{4.68}$$

$$E_{\mathrm{fv}}(x = L) = E_{\mathrm{fc}}(x = L) \tag{4.69}$$

The p-contacting point is at $x = 0$ and the n-contacting point is at $x = L$.

4.11 The numerical engine

The numerical engine used to solve the equations is divided into two parts. The first part is the core engine, which solves the Poisson equation and the continuity equations, the *core equations*. In the continuity equations, there are terms that involve the quantum-well states and carrier densities. The current density in and out of the wells, $J^i_{c,\mathrm{QW}}$ and $J^i_{v,\mathrm{QW}}$, as well as their 3D equivalents $J^{\mathrm{3D}}_{c,\mathrm{QW}}$ and $J^{\mathrm{3D}}_{v,\mathrm{QW}}$, depend on the carrier densities in the well and bulk states, as well as on the position (in energy) of the bound states. In the Poisson equation, the electron and hole charge densities, n_{2D} and p_{2D}, enter. These terms depend on the position of the bound states, and on the current densities in and out of the wells.

The second part of the numerical engine solves the Schrödinger equation in order to find the bound states. Once obtained, we can run the core engine to solve the core equations. To obtain self-consistency, we update the bound states regularly to ensure that the current and charge density contributions from the wells to the core equations are correct. A solution is obtained when the bound states no longer change when updated, and the *core variables* (the electron and hole carrier densities across the structure and in the wells, and the electrostatic potential across the structure) solve the core equations.

The core engine uses a Newton-Raphson method to find the solution. This involves calculating the Jacobian for the equations. The (i,j)-th element of the Jacobian is approximated using

$$\begin{aligned}\bar{J}_{ij}(\bar{y}^{(m1)},\bar{y}^{(m+1)}) &= \frac{\partial f_i}{\partial y_j^{(m+1)}}(\bar{y}^{(m)},\bar{y}^{(m+1)}) \\ &\approx \frac{f_i(\bar{y}^{(m)},\bar{y}^{(m+1)}+\Delta y\hat{e}_j)-f_i(\bar{y}^{(m)},\bar{y}^{(m+1)}+\Delta y\hat{e}_j)}{2\Delta y}\end{aligned} \tag{4.70}$$

where f_i is the i-th core equation, $\bar{y}^{(m)}$ is the unknowns-vector at iteration step m, $y_j^{(m)}$ is the j-th core variable at iteration step m, and $\hat{e}_j$ is a unit vector in the direction of the j-th core variable. We use the iterative procedure

$$\bar{y}^{(m+1)} = \lambda\left(\bar{y}^{(m)} - \frac{\bar{f}(\bar{y}^{(m)},\bar{y}^{(m+1)})}{\bar{J}(\bar{y}^{(m)},\bar{y}^{(m+1)})}\right) + (1-\lambda)\bar{y}^{(m)} \tag{4.71}$$

where we vary λ using a scheme that takes the "distance" to the solution into account.

Advantages of dividing the two problems

There are three very good reasons for solving the Schrödinger equation outside the core engine. Firstly, had we bundled the two problems, the Jacobian would have been considerably larger, and the calculation times would thus have been considerably longer. We would also automatically have the bound states calculated in each iteration step, even if they hardly changed. We avoid this with our method. Furthermore, including the Schrödinger equation into the core would have increased the bandwidth of the Jacobian drastically, which would lead to increased numerical problems.

Secondly, finding steady states from scratch is a complicated numerical exercise, even without wells. Including the Schrödinger equation in the core engine would destabilize the equation system during the first iterations.

Thirdly, dealing separately with the Schrödinger equation allows us to handle the bound states and the calculation of the Fermi levels for the wells much more easily. We normalize the wavefunctions, and modify only their shapes. In the core engine, we then scale up these normalized wavefunctions according to the carrier density. The advantage is that changes in the well carrier densities do not affect the wavefunctions themselves.

4.12 Electrical properties

In presenting the model, we have focused on the sweep-out of carriers from the absorbing region, where they are generated, to the contacts. However, as we discussed in the beginning of this chapter, the electrical properties of a device are equally important. The sweep-out of carriers may be fast, but if the capacitance of the device is high, the resistance-capacitance product, RC, will be the limiting factor for the response of the component as part of a circuit.

Several authors have used equivalent-circuit models to model measured S_{11} and S_{21} parameters [151, 84, 152, 41, 86, 153, 85, 87]. Resistors, capacitors, inductors, and current sources are used as fitting parameters in these models. Some of the circuit elements are known, such as the load resistor, which is 50 Ω. The inductances of the lead wires are usually also known. However, the resistance and the capacitance that characterize the modulator are typically fitted using parameters that have little physical basis.

We have made preliminary calculations of both capacitances and resis-

tances for a few components, for various biases and optical excitation power levels. These calculations are much too preliminary to be discussed here, but the minimization of the impedance mismatch with the external circuit should be part of the process of designing a modulator, and our simulator could possibly be used to produce input to an equivalent-circuit model.

In general, the sheet capacitance is

$$C = \frac{\mathrm{d}q}{\mathrm{d}V} \tag{4.72}$$

where q is the sheet carrier density and V is the bias. The differential sheet resistance is

$$R = \frac{\mathrm{d}V}{\mathrm{d}J} \tag{4.73}$$

in which J is the current density.

The resistance and the capacitance could be investigated as functions of optical power; heterobarrier design; well number and -design; contact doping; and other properties.

These issues go beyond the work presented in this thesis.

4.13 Summary

This chapter described our simulator for modeling of carrier sweep-out dynamics in electroabsorption modulators, and the physical picture of the carrier sweep-out on which it is based.

We described the various models that go into the simulator. The fundamental equations are the drift-diffusion equations, Poisson's equation, the Schrödinger equation, and the continuity equations. The calculation of the quantum-well states was discussed together with the calculation of the absorption. The simulator also contains models for spontaneous recombination, Shockley-Read-Hall recombination, and Auger recombination, and these models were described. The dynamics at heterojunctions, which includes transport through thermionic emission and Fowler-Nordheim tunneling, was described. The models describing escape of carriers from and capture to quantum-wells were presented. The two band line-up models that have been implemented in the simulator, one phenomenological, the other based on physical grounds, were described.

Other effects were mentioned in relation to the model, namely two-photon absorption, field-induced carrier heating, and bandgap renormalization. Field-induced carrier heating is partly and indirectly included through the use of a field-dependent mobility. Bandgap renormalization is included using a very simple, phenomenological model, whereas two-photon absorption is not included.

Finally, we touched upon the electrical device properties. These properties are as important for high-speed operation as the intrinsic transport properties of the device, and must be considered in the process of designing an electroabsorption modulator.

Chapter 5

Steady-state characterization of electroabsorption modulators

Steady-state characterization provides useful, basic information about a device. One of the most important properties of an electroabsorption modulator is the change in absorption that accompanies a change in the field across the intrinsic region. If absorption spectra are available for various biases, the *maximum attainable* extinction ratio can be determined as function of bias and wavelength. When the modulator is operated dynamically, the attainable extinction ratio will be lower as a result of carrier accumulation and field screening in the device. Thus, steady-state absorption spectra can be used to find the upper performance limit of the device with respect to its extinction ratio.

The saturation properties is another example of basic information that characterizes the dynamical properties of a device. The saturation is related to the escape times from wells and to carrier-induced field screening. By relating the excitation intensity to the absorption coefficient, information is obtained about the rate at which carriers are swept out of the intrinsic region.

Neither the absorption spectra, nor the saturation properties are easy to obtain from time-resolved measurements because the results of such measurements contain signatures of many individual transport processes. These include electron and hole escape from wells, transport to contacts, and transport across heterobarriers. The relative importance of each of those processes is difficult, if not impossible, to establish.

In this chapter, steady-state properties are investigated for various structures. We calculate absorption spectra as function of bias for two structures. Then we discuss the effect of band line-up on the field-screening behavior and the saturation properties. The saturation properties also depend on the carrier recapture dynamics in the device, and the thermionic escape model presented in Sec. 4.4.3 will be discussed in more detail, both on a general level, but also specifically with respect to the saturation properties. Finally, the influence of the separate-confinement heterostructure on the screening dynamics is investigated.

5.1 Modeling of absorption spectra

The absorption spectrum is obviously of the utmost importance in electroabsorption modulators, whether they are driven optically or electrically. The change in absorption should be as large as possible for a given change in the applied bias. It is also important to minimize the insertion loss in the modulator's on-state (the low-absorption operation point), and one may be interested in designing a device with a low polarization-dependent loss. A low polarization-dependent loss will be important in all-optical applications, where the in-line light polarization typically is arbitrary due to fiber birefringence. If the modulator has a low polarization-dependent loss, no additional filtering will be required for the device to operate properly. This means that devices with low polarization-dependent losses are simpler to operate and more power-efficient than devices with non-negligible polarization-dependent losses.

When the electroabsorption modulator is used as an external modulator, a low polarization-dependent loss may not be critical. Semiconductor lasers typically lase in only one polarization. Thus, the design of a modulator for external modulation is subject to significantly relaxed conditions. A considerable amount of work has gone into designing structures with low polarization-dependent losses [36, 154-157]. These structures are typically realized by using tensile strain in the wells to reduce the light hole bandgap (and using compressive strain in the barriers to avoid crystal dislocations).

Here, we consider two modulator structures designed for external modulation. The devices have wells with a slightly compressive strain. The structures were designed in collaboration with K. Yvind (COM) who also grew the structures. Both TE and TM spectra were measured for the two structures

for a number of biases from 0 to 8 V. The measurements were performed by F. Romstad (COM). Light from a tunable continuous-wave laser was coupled into the devices using a fiber. The output light was collimated with a microscope objective, polarization-filtered, and then detected with a broad-area detector.

Procedure for calculating absorption spectra

We described in Sec. 4.6.2 how the absorption spectra are calculated in our dynamical calculations. The physical picture described there required us to consider the wells independently. Depending on the field across the wells, and the width and depth of the wells, there may be a significant quantum-mechanical coupling between them. As discussed in Sec. 4.6.2, this coupling cannot be taken into account in our dynamical calculations. However, PinSim can be used to calculate the absorption spectra separately taking into account coupling between the wells. For the samples we investigate in this section it is crucial to take the coupling into account. The structures have very low barriers for both holes and electrons, and as a result the wavefunctions extend across many wells even at zero field.

As previously mentioned, excitonic absorption is not included in our absorption calculations, but there are also no clear signs of excitonic absorption in the measured spectra presented below. The absence of excitonic absorption in our samples is most likely due to the shallowness of the wells. The exciton in those samples will be ionized already at very low fields.

The procedure for calculating the absorption spectra is the following: For the device structure in question, the steady state is calculated for the applied bias of interest. This gives us the banddiagram for that particular bias. We then solve the Schrödinger equation for this potential to find the eigenstates, from which we then calculate the absorption spectrum using Eq. (4.48). We emphasize that the field across the wells is not a free parameter in the calculations. If a spectrum is measured for an applied voltage of, say, 2 V, then PinSim is used to find the field across the wells for that bias.

5.1.1 Absorption spectra for two structures

Calculations for two different structures will be presented and compared to measured spectra. The structures differ by their well- and barrier compositions.

Banddiagrams for the two structures

The two structures are shown in Fig. 5.1. The Tersoff band line-up model (Sec. 4.8.2) was used to calculate the band offsets. Both structures have ten wells. The interface between the doped regions and the intrinsic region is at the outermost barriers in Fig. 5.1. The depths of the hole wells in both structures are only about the room-temperature thermal energy. The depth of the electron wells in the two structures are a few times that.

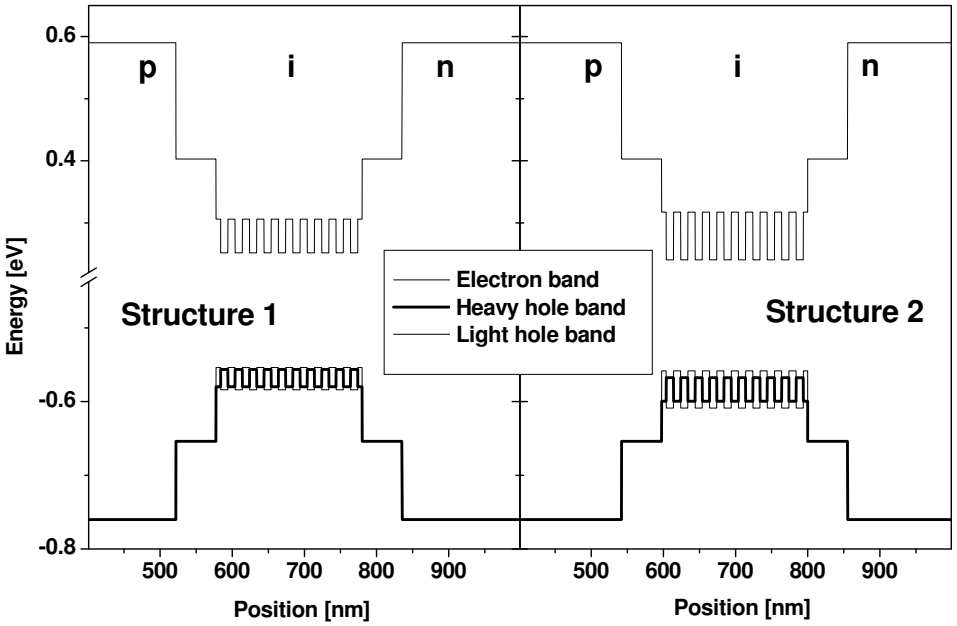

Figure 5.1: Banddiagrams for the two structures for which the absorption spectra are calculated.

The heavy hole wells in both structures are type I, whereas the light hole wells are type II. Absorption from type-I wells decreases for increasing fields because the electron and holes wavefunctions move away from each other as shown in Fig. 5.2, causing a reduction in the wavefunction overlap and thus

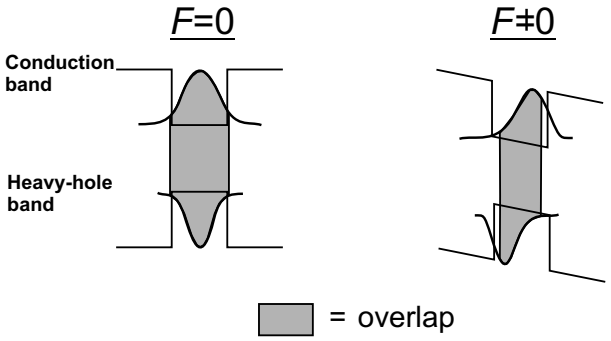

Figure 5.2: Schematic figure showing the ground state wavefunctions for $F = 0$ and $F > 0$ for the electron and the heavy-hole wells. The heavy-hole well is type I. Thus, the overlap, schematically illustrated by the grey areas, is largest at low fields and decreases for increasing fields.

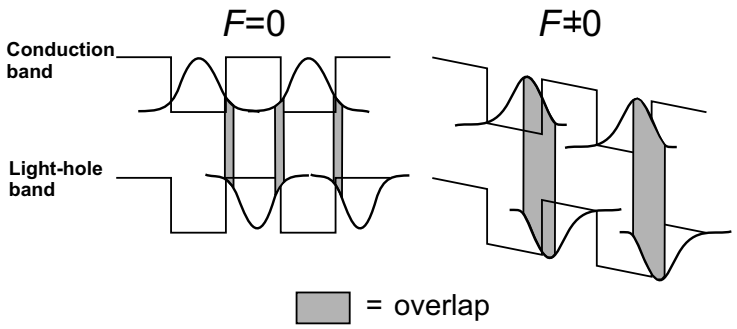

Figure 5.3: Schematic figure showing the ground state wavefunctions for $F = 0$ and $F > 0$ for the electron and the light-hole wells. The light-hole well is type II, so the overlap, schematically illustrated by the grey areas, is small at low fields but increases for increasing fields.

in the absorption (by Eq. (4.48)). Absorption from type-II wells is small at zero field because the electron and hole wavefunctions are concentrated at different positions as shown in Fig. 5.3. As opposed to absorption from type-I wells, the absorption from type-II wells increases when the field is increased because the electron and hole wavefunctions are displaced toward each other.

Structure 1, shown on the left in Fig. 5.1, has the lowest barriers of the two structures, both for electrons and for holes. The well depths of the two hole types are only about the room-temperature thermal energy. For electrons, the depths are closer to $2k_{\mathrm{B}}T$. We note that the Tersoff line-up model yields electron wells that are significantly deeper than both types of hole wells. This is in stark contrast to the conventional constant-offset line-up model described in Sec. 4.8.1, which assumes a ratio between the conduction-band offset and the bandgap of around 0.4 [140, 141].

Structure 2 has slightly deeper wells than Structure 1. The electron wells are close to 50 % deeper than those in Structure 1. The hole wells are close to 100 % deeper than those in Structure 1. The band-offset ratio is therefore somewhat smaller than that in Structure 1. Because the mass of the electron is significantly lower than the mass of the heavy hole, modifying the structure in such a way that the electron well is deeper than the heavy-hole well will result in a larger overlap between the ground state wavefunctions at low fields [158, 42].

Measured and calculated absorption spectra

Figure 5.4 shows the measured and calculated TE absorption spectra for Structure 1 at various biases, and Fig. 5.5 shows the TM spectra. Figure 5.6 shows the calculated and measured TE spectra for Structure 2, and Fig. 5.7 shows the TM spectra.

The correspondence between the measurements and the calculations is quite good for both structures and both polarizations, with respect to both the wavelength dependence and the bias dependence. The calculated TE spectra for Structure 2 are in particularly good correspondence with measurements.

The applied bias and the field across the wells are approximately related by

$$F = \frac{V_{\mathrm{bi}}}{L_{\mathrm{int}}} - \frac{V_{\mathrm{app}}}{L_{\mathrm{int}}} \tag{5.1}$$

where V_{bi} is the built-in voltage, V_{app} is the applied voltage, and L_{int} is the width of the intrinsic region.[9] The correspondence between the measured and the calculated spectra as function of applied bias thus tells us that the

[9] The built-in voltage in the structures we look at is around 1.3 V, and the built-in field is above 30 kV/cm.

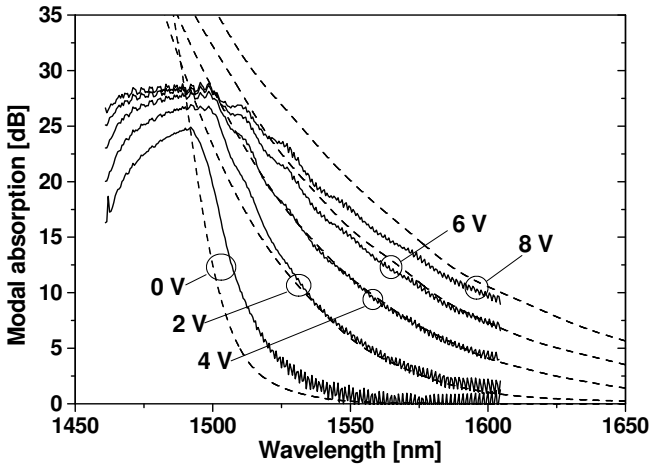

Figure 5.4: Measured and calculated TE spectra for Structure 1. The component is 250 μm long. Note that we show the modal absorption.

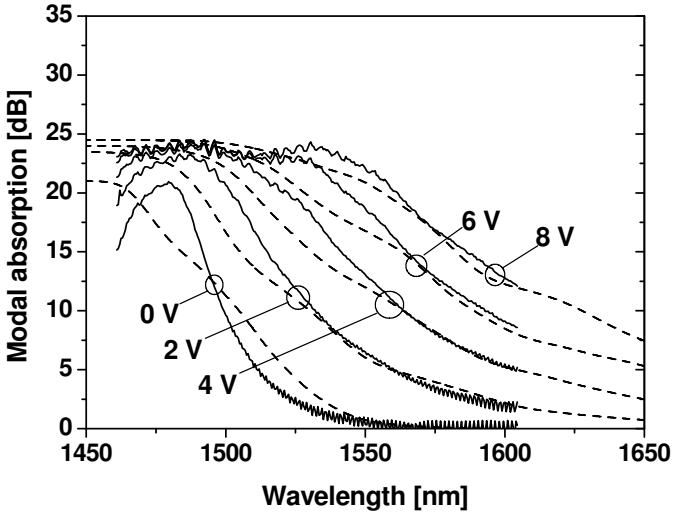

Figure 5.5: Measured and calculated TM spectra for Structure 1. The component is 250 μm long. Note that we show the modal absorption.

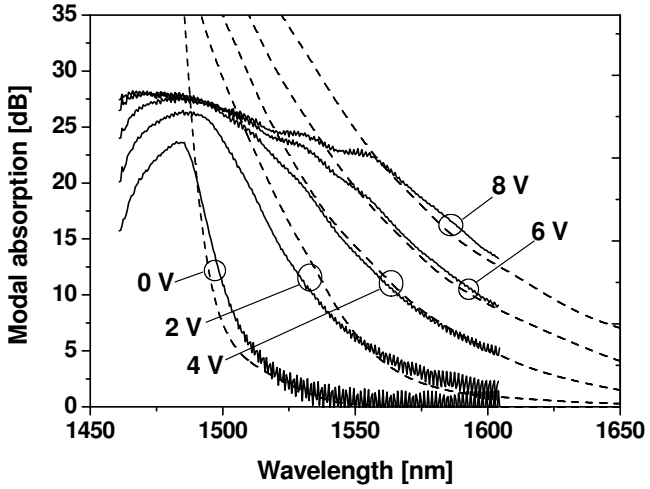

Figure 5.6: Measured and calculated TE spectra for Structure 2. The component is 250 μm long. Note that we show the modal absorption.

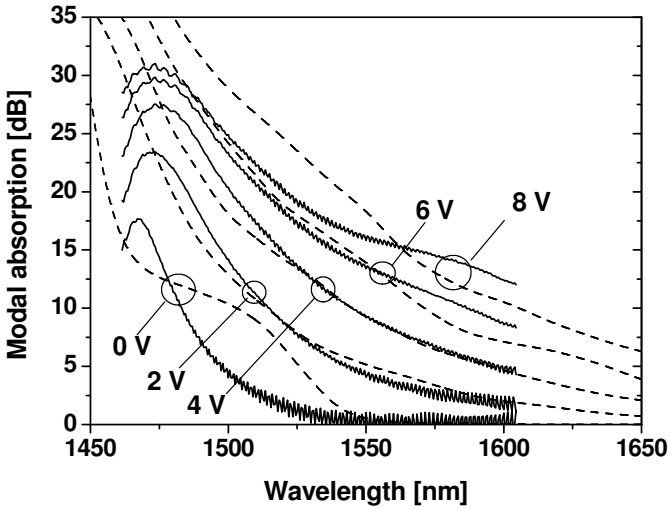

Figure 5.7: Measured and calculated TM spectra for Structure 2. The component is 250 μm long. Note that we show the modal absorption.

change in field that accompanies a change in the bias is well estimated by our calculations. (The reason why Eq. (5.1) is only approximately valid is that at low biases there is a non-negligible screening from carriers that pile up at the heterobarriers. The screening reduces the field, which is therefore lower than expected from Eq. (5.1).)

The TE absorption has contributions from both heavy-hole and light-hole states. The TE and TM absorption coefficients are given by

$$\alpha_{\mathrm{TE}} = \alpha_{\mathrm{e-hh}} + \frac{1}{3}\alpha_{\mathrm{e-lh}} \tag{5.2}$$

$$\alpha_{\mathrm{TM}} = \frac{4}{3}\alpha_{\mathrm{e-lh}} \tag{5.3}$$

where $\alpha_{\mathrm{e-hh}}$ is the absorption coefficient resulting from transitions from heavy-hole states to electron states, and $\alpha_{\mathrm{e-lh}}$ is the absorption coefficient resulting from transitions from light-hole states to electron states. The good correspondence for both TE and TM spectra between calculations and measurements thus indicates that the banddiagrams in Fig. 5.1 are good approximations to the real energy landscapes in the two samples, both for electrons and for the two hole types. Both the wavelength dependence and the bias dependence of the TE and TM spectra are critically dependent on the band offsets, and we conclude that the band offsets calculated using the Tersoff line-up model approximate well the real offsets. The relation between the material absorption and the modal absorption includes the confinement factor (by Eq. (4.47)), and the spectra presented above are calculated using $\Gamma = 0.02$ for all wells and both polarizations, and using a device length of 250 μm. The confinement factor is estimated from an optical mode calculation.

The step-like features in the TM spectra for Structure 2 (Fig. 5.7) compared to the TM spectra for Structure 1 occur in part because Structure 2 has deeper electron wells than Structure 1. The deeper electron wells have a 'more discrete' density of states.

There are limits to how detailed we may compare the calculated and measured spectra. The spectra are calculated using parabolic sub-bands and without taking band mixing into account. Including the coupling between the heavy-hole states and the light-hole states will change the dispersion relation and modify the absorption spectra to some degree. Even with parabolic sub-bands, the carrier masses are not known with certainty, and this may also contribute to the differences between measured and calculated spectra.

Finally, our calculated spectra show a larger modal absorption for the

high energies than do the measured spectra. Figure 5.5 shows the TM spectrum for Structure 1 where we have included a small contribution to the transmission from a "first-order" mode that is assumed to not be absorbed. The transmission is then given by

$$T = |A_0 \exp(-\alpha_{\text{modal}} L_z) + A_1| \tag{5.4}$$

where A_0 is the amplitude of the zero-order mode, A_1 is the amplitude of the first-order mode, L_z is the device length ($L_z = 250$ μm), and α_{modal} is the modal absorption. The coefficients A_0 and A_1 are used as fitting parameters. Including a higher-order mode in this way enhances the correspondence at higher energies, as seen in Fig. 5.5, and such a mode might therefore be partly responsible for the behavior seen in the measured spectra.

5.2 Absorption saturation

In this section, we investigate device saturation properties. The saturation power is important both for all-optical functionalities and for functionalities where the device is electrically modulated. As an external modulator, it is desirable to have a high saturation power. A high saturation power allows the power level at the input end of the device to be high and thus the power level for the modulated signal at the output can be high.

A single structure will be investigated in this section. However, the calculations will be performed using the two different line-up models to illustrate the influence of the line-up on the saturation properties. The line-up models are described in Sec. 4.8. The field distributions at various power levels are also presented. We consider a structure with ten wells. It is unstrained, with $In_{0.79}Ga_{0.21}As_{0.45}P_{0.55}$ barriers and $In_{0.53}Ga_{0.47}As$ wells. It is biased at -0.27 V, and the excitation wavelength is 1600 nm. We assume thermionic recapture in the calculations (see the definition on page 48).

Figure 5.8 shows the banddiagram when a constant 43/57 line-up is assumed. This line-up results in electron wells that are 126 meV deep and hole wells that are 167 meV deep. The electron separate-confinement heterobarriers are 132 meV high and the hole barriers are 175 meV high. Figure 5.9 shows the banddiagram calculated with the Tersoff line-up model. This line-up gives electron and hole wells that are 145 meV and 148 meV deep, respectively. The electron separate-confinement heterobarriers are 196 meV high and the hole barriers are 112 meV high. The optical power level is 50 μW (≈ -13

dBm) in Fig. 5.8 and Fig. 5.9. At this power level, it is difficult to see any differences in the field behavior between the two line-up models. However, the corresponding fields, which we show later in this chapter, display a small difference.

Figure 5.10 and Fig. 5.11 show the banddiagrams when the optical power level is 5 mW ($\approx$ 7 dBm). The field distributions are now very different for the two line-up models. The 43/57 line-up model gives a much more symmetrical field distribution than the Tersoff line-up model. The Tersoff line-up gives a high electron separate-confinement heterobarrier and a significantly lower hole barrier, as quantified above. This causes a large pile-up of carriers at the i-n interface, much more than at the p-i interface. As a result, the potential drop lies almost entirely at the i-n interface. It is clear that for both line-up models, there is a contribution to the potential drop from the well region. The largest potential drop, however, is not due to carriers in the wells, but due to carriers that have piled up at the heterobarriers.

Figure 5.12 shows the field distributions at three different power levels: 50 μW (banddiagrams shown in Fig. 5.8 and Fig. 5.9), 1 mW, and 5 mW (banddiagrams shown in Fig. 5.10 and Fig. 5.11). Figure 5.12 clearly shows that the field distribution is more symmetrical for 43/57 line-up than for Tersoff line-up. Even at low excitation levels, represented by the 50-μW case, the field is less symmetrical for the Tersoff line-up than for the 43/57 line-up. The carrier pile-up is also clearly different in the two cases. The Tersoff line-up model gives a high electron heterobarrier and a low hole heterobarrier, and this causes a shift of the pile-up towards the i-n interface compared to the situation with 43/57 line-up. Figure 5.12 also shows that the overall field screening is greater with Tersoff line-up than with 43/57 line-up, despite that the Tersoff line-up model gives a lower zero-power absorption coefficient at 1600 nm than the 43/57 line-up model.

Figure 5.13 shows the absorption coefficients for the two line-up models as function of excitation intensity (the third curve, labeled 'Tersoff, no recapture' will be discussed in Sec. 5.3). Of the two models, the 43/57 line-up model provides the higher 1600-nm absorption coefficient. We define the *saturation intensity* as that intensity for which the absorption coefficient is half the zero-intensity absorption coefficient. Tersoff line-up gives a saturation intensity of 260 kW/cm^{-2}, whereas the 43/57 line-up gives a saturation intensity of 300 kW/cm^{-2}. This means that the sweep-out rate is lower with Tersoff line-up than with the 43/57 line-up. The line-up affects the escape times from the wells. Tersoff line-up gives more shallow hole wells than does

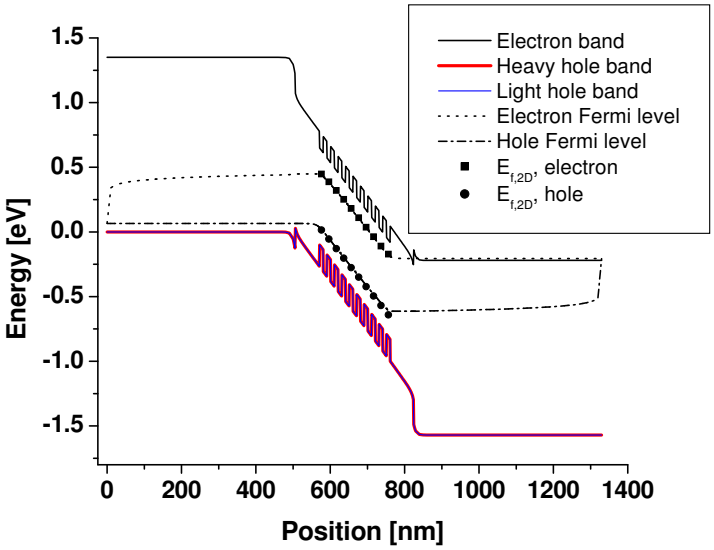

Figure 5.8: Banddiagram for our ten-well structure excited with an optical power of 50 µW. The 43/57 line-up model has been used to calculate the band offsets.

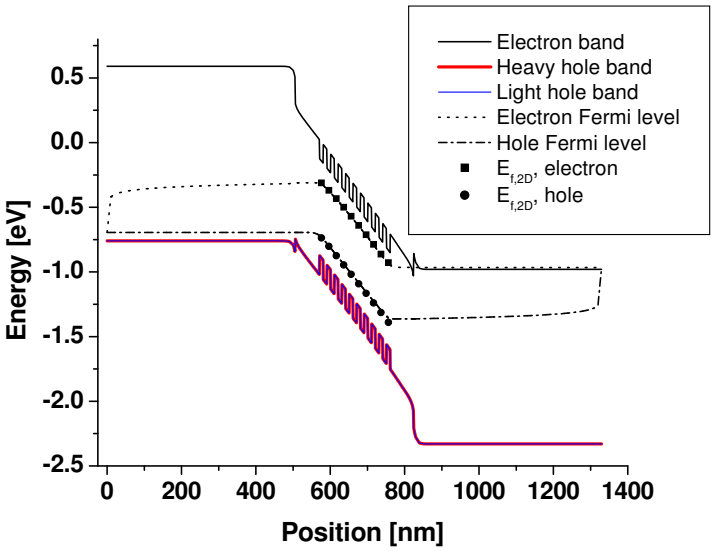

Figure 5.9: Banddiagram for our ten-well structure excited with an optical power of 50 µW. The Tersoff line-up model has been used to calculate the band offsets.

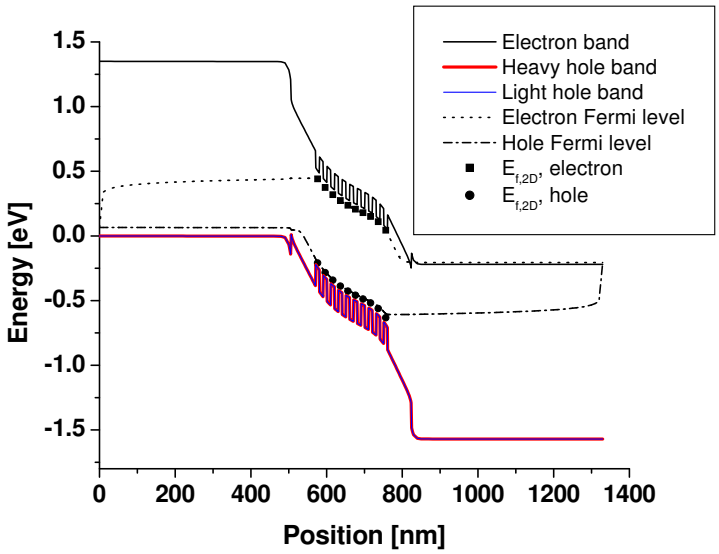

Figure 5.10: Banddiagram for our ten-well structure excited with an optical power of 5 mW. The 43/57 line-up model has been used to calculate the band offsets.

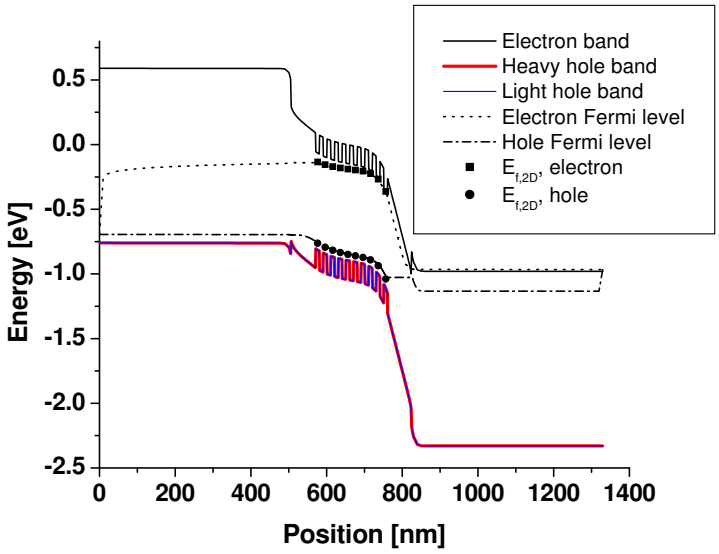

Figure 5.11: Banddiagram for our ten-well structure excited with an optical power of 5 mW. The Tersoff line-up model has been used to calculate the band offsets.

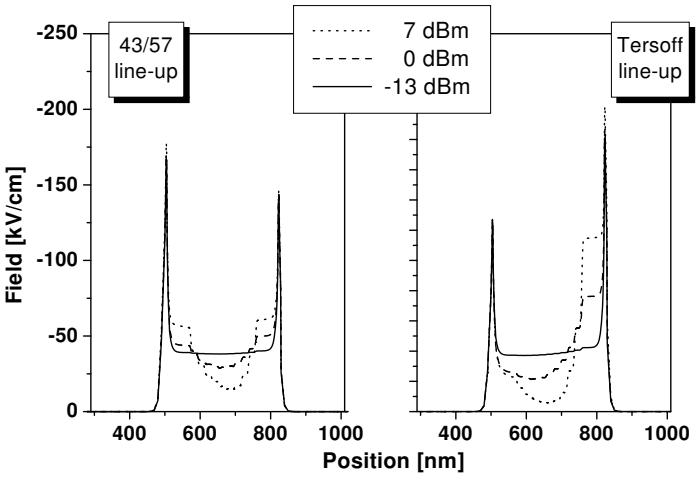

Figure 5.12: Field distributions with the two line-up models, for three different power levels: 50 μW, 1 mW, and 5 mW. As the power goes up, the field screening across the well region increases. On the left-hand side, the constant 43/57 line-up model is used; on the right-hand side, the Tersoff line-up model has been used.

the 43/57 line-up. At zero excitation power, the escape times for electrons and holes are 7 ps and 13 ps, respectively, when the Tersoff line-up model is used. They are 3.5 ps and 26 ps, respectively, when the 43/57 line-up model is used. This apparently indicates that the saturation power should be lower for the 43/57 line-up, but we found above that this is not so. Due to the non-uniform field across the well regions in the two structures, there is a large difference between the escape times for the different wells, both for holes and for electrons. However, also at 5 mW are the escape times for holes larger with 43/57 line-up than with Tersoff line-up. Furthermore, the thermionic recapture changes the effective escape times. The actual reason for the lower saturation intensity with Tersoff line-up is that there is a much higher field screening for this line-up than for the 43/57 line-up. The high electron heterobarrier predicted by the Tersoff line-up model cause a large pile-up of carriers at the i-n heterobarrier, and these carrier give rise to a large screening of the field.

The conclusion from the calculations and the discussion above is that a (very!) complicated interplay between the escape times, the capture times,

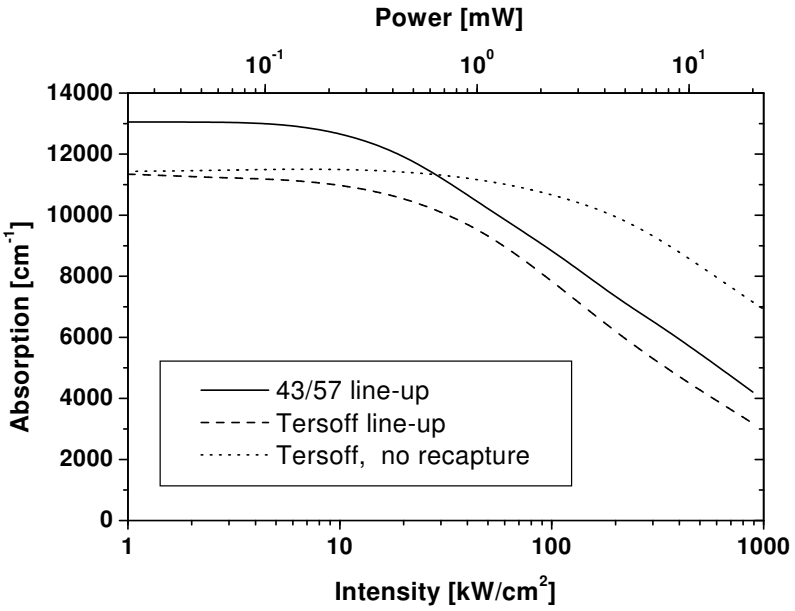

Figure 5.13: The dependence of the absorption coefficient on the excitation intensity is shown for the two different line-up models assuming thermionic recapture. For the Tersoff line-up model, the dependence is also shown for the case where there is no recapture.

and the pile-up at heterobarriers determines the saturation intensity. The corollary is that the zero-power escape times from the wells cannot be used to predict the saturation power.

The band line-up in a structure depends on the material compositions at the heterointerfaces. The line-up is also influenced drastically by strain. The Tersoff model generally gives a larger fraction between the conduction-band offset and the valence-band offsets than does the constant-offset 43/57 model. For applications that require high saturation powers it is therefore important to consider the use of strain carefully. For switching applications, it is desirable to have low switching energies. However, it is clear that a low saturation power should not be obtained through an increase of the sweep-out times. Instead, the saturation power should be lowered by increasing the field-induced absorption change [23].

5.3 Influence of recapture on the steady-state properties

Capture of carriers into the wells ensures that thermal quasi-equilibrium is established in the steady state. If there is no capture, the effective escape time is simply the time given by Eq. (4.23). When there is capture, the *effective* escape times increase because of the current of particles back into the wells. The calculations in Sec. 5.2 assumed thermionic recapture.

Figure 5.13, which was discussed in Sec. 5.2, also includes, for Tersoff line-up, the absorption coefficient as function of intensity when we assume that there is no recapture. (the term *no recapture* is defined on page 48). The figure shows that the saturation properties will be significantly affected if there is no recapture. Without recapture, the saturation intensity is about an order of magnitude higher than if the recapture is thermionic. The difference is due to the shorter effective escape times that result when we assume that there is no recapture instead of thermionic recapture.

In our model, the relation between the escape time and capture time, given by Eq. (4.28), must be satisfied in the steady state, at least when there is no optical excitation. This relation is well known from modeling of lasers [91]. However, laser models use capture times that are measured or calculated. Typical values are between a few hundred femtoseconds and a few picoseconds [159-164]. An effective escape time could then be found through Eq. (4.28), and it would of course be longer than the capture time (see Sec. 4.4.3).

For electroabsorption modulators, it is common to calculate the escape time rather than the capture time. We do this using Eq. (4.23). Then, by requiring that the net current out of the well be zero in the steady state, we find a capture time (given through equations (4.26) and (4.27)). The capture times found in this way can quite easily be down in the $1 - 100$ fs range, much lower than those in lasers and hardly physical seeing as no carrier scattering process in semiconductors is this fast. This suggests that relation (4.28) might not be valid under non-equilibrium conditions.

Actually, we would expect capture times in electroabsorption modulators to be even longer than those found in lasers with similar epitaxial structures. The density of carriers in the quasi-continuum states are lower in modulators than in a lasers. Thus, carrier-carrier scattering and carrier-phonon scattering, which are responsible for the capture of carriers into the wells,

will proceed at lower rates in modulators. The escape process, on the other hand, is due to scattering between localized carriers. It might therefore be suspected that this is a more efficient scattering process than the scattering processes responsible for capture of carriers, which are processes that involve scattering between carriers moving at high speeds. The escape 'process' and the capture 'process' in modulators are therefore physically very different. Our interpretation is that relation (4.28) *is* valid in the steady state, but one should not think of a 'capture time' and an 'escape time', because these do not describe two *physical* processes.

Based on the discussion above, we suggest that

1. When the state of the modulator is far from equilibrium, for instance after excitation with a short optical pulse, the effective capture time is significantly longer than that predicted by Eq. (4.27).

2. In the steady state, relation (4.28) is fulfilled, that is, there is thermionic recapture.

Furthermore, we suggest that both of these points are valid also under optical excitation. With respect to point 1, this is so by definition. With respect to point 2, it will be a reasonable assumption only for as long as the optical field does not affect the carrier temperatures significantly.

There is a significant amount of experimental evidence that supports our claims. Measurements of absorption recovery after short-pulse excitation typically show decay times comparable to what Eq. (4.23) would yield, that is, the capture current density is insignificant (we refer to Sec. 4.4.3 and Sec. 4.6 for a few references to papers that discuss the comparison of measured and calculated escape times). This corroborates point 1 above.

With respect to the steady state, experimentally determined saturation powers [23, 165] are comparable to those found above in Fig. 5.13 where we used thermionic recapture, whereas the exclusion of recapture in Sec. 5.2 resulted in much higher saturation power levels. This corroborates point 2 above.

Considering Fig. 5.13 it is clear that to model components, it is *critical* to understand the relative importance of the capture and escape processes. Based on the discussion above, we think that the guidelines given above for when to include escape and when to leave it out reflect reality well. This picture is used in most of the work presented in this thesis. We presented the calculation of the saturation properties with no recapture to support the

discussion above, and we will present dynamical simulations in Chapter 6 to sophisticate slightly the gross distinction given above.

Relation (4.26) is affected by the applied voltage. Recapture is less important at higher bias because the escape time is reduced compared to the capture time. Thus, comparing measured and calculated saturation energies for various applied voltages could provide more insight into the issues discussed above.

As mentioned, we return to the issue of recapture in Sec. 6.6, where the implications of recapture on the sweep-out dynamics is investigated.

5.4 Field screening due to heterobarriers

The separate-confinement heterostructure in semiconductor waveguide-based lasers and modulators has an index-of-refraction profile which provides guiding of light in modes with relatively low propagation losses. In semiconductor lasers, the separate-confinement heterostructure furthermore improves the electrical properties by helping to confine carriers to the active region. Modulator or laser, the presence of the separate-confinement heterostructure is almost a given, simply because the active material of interest has a bandgap which is significantly lower than that of the material on which the active material is grown. In 1550-nm InGaAsP-based devices, the active material will have a bandgap energy near 0.8 eV, and will typically be grown on an InP seed wafer, which has a bandgap energy of 1.35 eV. Therefore, some kind of transition must be made between the high-bandgap seed-wafer material and the active material.

The bandgap can be varied either in a stepwise fashion or continuously during wafer growth. The stepwise change of the bandgap is the most common approach because it is the simplest to realize. The potential barriers incorporated into an epitaxial structure must be overcome by carriers on their way to the contacts. If a barrier is high compared to the thermal energy, carriers will pile up near the barrier as discussed in Sec. 4.5.1. This pile-up is a problem in components that depend on changes in the electric field in the active region. The electroabsorption modulator is such a component. The carriers that are caught at the heterobarriers screen the field. Consequently, the field in the active region is affected when the optical power produces a large density of photo-excited carriers. Screening of the field in the well region also reduces the escape rate of carriers out of the wells through

Eq. (4.23).

The physics of this pile-up effect is similar to that of the thermionic emission model used for quantum wells and described in Sec. 4.4.3. There is an important difference. For the bulk heterobarrier dynamics, it is not possible to attribute a simple time constant to the transport. In a sense, it is the direct-current properties that are affected by the height of the barriers. The same current density can be supported by a small or a large barrier, but the degree of field screening that results in the intrinsic region for a given current density will be different for different barrier heights. The higher the barrier, the greater the pile-up.

To illustrate the influence of the heterobarrier structure on the power-handling capabilities, we examine how the field is screened in two structures with different heterobarrier structures. Figure 5.14 shows the two different structures. We use a constant 43/57 line-up. The intrinsic regions in the two structures are the same, but one structure has a one-step barrier ("1-step" in Fig. 5.14) between p-contact and the intrinsic region and between the intrinsic

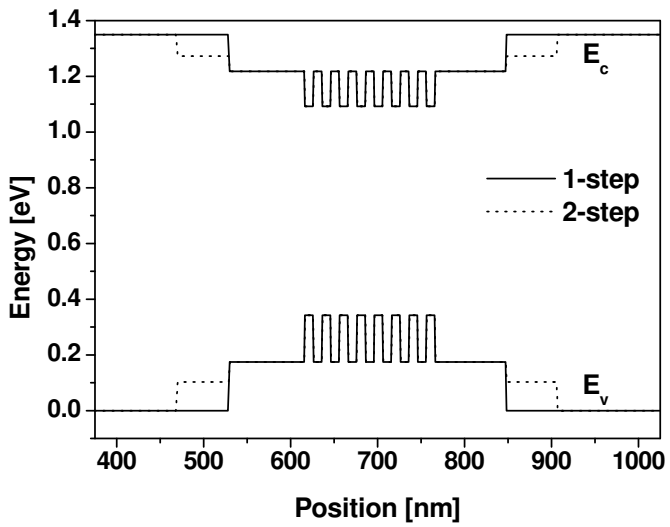

Figure 5.14: Illustration of the two structures that are investigated to determine the influence of the heterobarrier design on the steady-state properties.

region and the n-contact; the second structure ("2-step" in Fig. 5.14) has two steps on both sides of the intrinsic region. Because the intrinsic-region widths in the two structures are different, we need to apply different voltages to the two structures to obtain the same field across their well regions before optical excitation. This is to ensure that the mobilities and the times carriers take to escape from the wells are the same in the two cases. For the 1-step structure, the bias is -0.3 V; for the 2-step structure, it is -0.62 V. The structures are excited at 1600 nm with an optical power level of 2 mW, and we have assumed thermionic recapture.

Figure 5.15 shows the field distributions in the intrinsic regions of the two structures. Note that for both structures, the outermost field changes are due to transitions from highly doped regions to undoped regions ("p-i" marks an interface between a p-doped region and an undoped region, and "i-n" marks an interface between an n-doped region and an undoped region). The difference is significant. More carriers pile up in the 1-step structure, and this leads to a larger field screening in this structure than in the 2-step

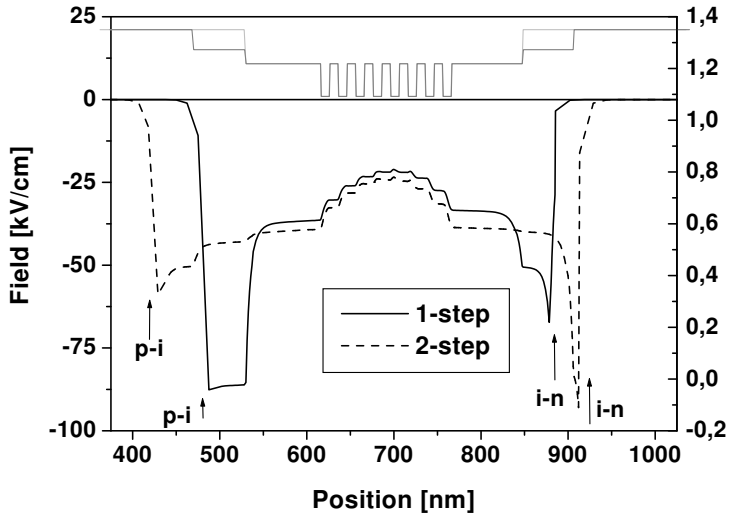

Figure 5.15: Field distributions in the two structures shown in Fig. 5.14 under optical excitation. The excitation power level is 2 mW. As a reference, the band-diagrams for the two structures are indicated.

structure. It can also be seen that holes contribute more to the screening than electrons.

For a given power level, the larger field screening in the 1-step structure will result in a lower absorption coefficient in this structure than in the 2-step structure. Because the carrier sweep-out rate is lower in the 1-step structure under excitation, due to the larger field screening, the carrier excitation rate must also be lower. In quantitative terms, the absorption coefficient at zero excitation power is $9.16 \cdot 10^3$ cm^{-1} for both structures. The absorption coefficient at 2 mW is $5.64 \cdot 10^3$ cm^{-1} for the 1-step structure and $6.23 \cdot 10^3$ cm^{-1} for the 2-step structure. It is worth noting that the ~ 10 % difference between the absorption coefficients is similar to the difference between the fields in the well regions of the two structures, shown in Fig. 5.15.

Our results clearly show that the heterobarriers must be given serious consideration when modulators are being designed. The screening of the field causes an increase in the escape times from the wells, and thus it reduces the speed of the component.

A number of papers mention that carriers pile up at heterointerfaces [166, 23, 167]. The calculations presented above quantify the pile-up in the steady state for two specific structures subjects to certain external conditions (bias, power level, excitation wavelength).

As shown above, dividing the single barriers in the 1-step structure into two steps reduces the field screening significantly. Further calculations have shown that dividing the barriers into more than two steps reduces the field screening only little further. From a wafer-growth perspective, this means that although attention must be given to the design of the heterobarriers, a few barrier steps will often suffice. However, at very high speeds it may be necessary to use more sophisticated transition schemes to reduce the pile-up even more. We investigate the influence of pile-up under pulsed excitation in Sec. 6.3.

A final point we wish to make here is that carrier pile-up decreases if the diffusion terms in eqs. (4.1)–(4.2) should become less important relative to the drift terms. This can be explained by the following argument (given for a single carrier type): If the diffusion term were reduced but the same number of carriers were present near the heterobarrier, then those carriers would be concentrated closer to the interface. This would increase the thermionic current across the barrier. Thus, equivalently, the density of piled-up carriers will be lower if the relative importance of the diffusion term is reduced.

Diffusion results from scattering between carriers. The diffusion "con-

stant" is thus reduced if the carrier density decreases. The influence of diffusion on the pile-up is of course not purely academic. Increasing the bias will also reduce the relative importance of diffusion and thus reduce pile-up.

The actual value of the diffusion constant, and its dependence on carrier density, field, and other variables, is very difficult to evaluate. The relation between diffusion and pile-up discussed above should therefore be considered a qualitative rather than a quantitative relation.

5.5 Summary

This chapter presented calculations of steady-state properties of electroabsorption modulator structures. The TE and TM absorption spectra were calculated for two different structures using our simulator. Comparison with measurements showed good correspondence with respect to both wavelength dependence and bias dependence.

Saturation of the absorption was investigated for two different line-up models. The field distribution at various power levels were presented. We found that the Tersoff line-up model gave a lower saturation power than did the constant-offset 43/57 line-up. Line-up is affected by strain, and thus the amount and type of strain (tensile or compressive) should be considered rather carefully when modulators are being designed.

The influence of recapture on the saturation intensity was investigated by comparing the saturation intensity when there is no recapture to the saturation intensity that results if the recapture is thermionic. With no recapture, the saturation intensity is about an order of magnitude higher than with thermionic recapture. Although this result pertains to a specific structure and specific external parameters, it illustrates that different recapture models can give very different results. Having such an impact on the properties, a significant effort should be put into understanding better the capture process in electroabsorption modulators.

Results were presented that showed a strong influence of the separate-confinement heterostructure design on the screening dynamics. The higher the separate-confinement barriers are, the larger the field screening will be. It was demonstrated that dividing a heterobarrier into two smaller steps can reduce the field screening significantly. Actually, for the structure that we considered, a division of the barriers into more than two steps reduced the field screening only little further. This means that even a relatively coarse division of the heterobarriers can eliminate a lot of the pile-up.

Chapter 6

Modeling of carrier sweep-out in electroabsorption modulators

All applications of the electroabsorption modulator rely on changes in the modulator's absorption. The absorption must be able to respond on the time scale appropriate for the application in question. For all-optical wavelength conversion, for instance, a transmission window is opened through optical excitation and closed again through the sweep-out of photo-excited carriers. The maximum allowed temporal width of the transmission window is determined by the operation bit-rate, and the challenge is to recover the absorption within the available time slot. Whether this is possible depends on the modulator design.

In Chapter 3, the influence of the sweep-out time on an electroabsorption modulator's ability to perform certain all-optical functions was investigated. Specifically, the discussion concerned wavelength-conversion, signal regeneration, and demultiplexing. A simple model which incorporated a saturation mechanism was used to describe the carrier sweep-out. In the present chapter, we investigate the sweep-out process itself using the model described in Chapter 4.

Time-resolved investigations are very useful for characterizing the absorption recovery in electroabsorption modulators. However, an experiment can yield only the total absorption recovery. It provides no information about the recovery in the individual wells, or about the underlying dynamics. The relative importance of band filling versus field screening is also difficult to

establish. It is possible to investigate it by indirect methods, but again the results represent only the overall recovery and give no information about the local behavior. Furthermore, such methods require that a number of simplifying assumptions be made, see e.g. [76].

Our model can be used to investigate the dynamics in electroabsorption modulators on a well-by-well basis. This enables us to follow not just the temporal but also the spatial course of the recovery. In this chapter, we present calculations of the absorption recovery in different structures under various conditions. From these calculations, we draw a number conclusions concerning the influence of design parameters and external parameters on the dynamics. The calculations simulate pump-and-probe experiments. A pump-and-probe experiment is performed by exciting the device under investigation with one pulse (the *pump*) and then time-resolve the ensuing absorption recovery by looking at the transmission of another, weak pulse (the *probe*). The pump-and-probe technique is one of the most powerful tools for characterizing the absorption recovery in electroabsorption modulators. It has a high temporal resolution, and it yields unambiguously the absorption change induced by the optical pump. The temporal resolution of a pump-and-probe experiment is determined by the width of the optical pulses that are employed.

Pump-and-probe simulations

The sweep-out is investigated by exciting the structures optically using 1-ps full-width-at-half-maximum Gaussian pulses. In all our calculations, the excitation peaks at $t = 2.5$ ps. We emphasize that the time variable thus is not a delay time (between the pump and the probe). Instead, zero delay time corresponds to $t = 2.5$ ps.

The absorption change per well can be divided into two parts: One that is due to changes in the field, and one that is due to band filling. Before excitation, there are almost no carriers in the wells. If the density of carriers in a well is zero, and the field across the well is changed, the absorption spectrum will change. This change will be referred to as the *field contribution to the absorption change*. After excitation, there will be carriers in the well, and the presence of these carriers gives a further contribution to the absorption change. This contribution will be referred to as the *band filling contribution to the absorption change*. To formalize this, let $\alpha = \alpha(F(t), N(t))$ be the

absorption coefficient at field $F(t)$ and carrier density $N(t)$ for a given well. Before excitation, at time $t = 0$ ps, there is some constant field F_0 across the well and a constant carrier density N_0 (≈ 0) in the well. The corresponding absorption coefficient is $\alpha(F_0, N_0)$. After optical excitation, the total absorption change at time t is

$$\Delta\alpha_{\text{total}}(t) = \alpha|_{F(t),N(t)} - \alpha|_{F_0,N_0} \tag{6.1}$$

The field contribution to the absorption change is

$$\Delta\alpha_{\text{field}}(t) = \alpha|_{F(t),N_0} - \alpha|_{F_0,N_0} \tag{6.2}$$

and the band filling contribution is

$$\Delta\alpha_{\text{band-fill}}(t) = \alpha|_{F(t),N(t)} - \alpha|_{F(t),N_0} \tag{6.3}$$

The absorption changes presented in the following are changes in the material absorption, which is given by Eq. (4.48).

Definition of decay time

In the following there will be examples of variables that do not approach their steady-state values monotonically from their peak values. The term "decay time" (or "recovery time") for a function f will therefore refer to *the time, relative to offset time t_0, of the last instant at which $|f(t)|$ equals fraction r of the maximum value of $|f(t)|$.*[10] Note that this definition is consistent with the time constant that characterizes a simple exponential decay, but it is more general. It can be used in cases where the decay is not exponential; in cases where the decay is not monotone decreasing from the peak; and in cases where the function of interest changes sign (one or more times).

The proper choice of the reference time t_0 depends on the circumstances. Often, the time at which the function peaks will be appropriate. However, when comparing functions that have different peak times, it will be more appropriate to use the same t_0 for all the functions, and to use a time that

[10] The definition is very hard to put into words. The formal definition of our decay time, τ, is

$$\tau = \max\left\{t \;\middle|\; |f(t)| = r \max\{|f(t)|\}\right\} \tag{6.4}$$

corresponds to some relevant event. As an example, the peaks for the three curves in Fig. 6.3 do not occur at the same time (the figure shows the field recovery in three different structures). However, the optical excitation peaks at $t = 2.5$ ps in all three cases, and $t_0 = 2.5$ ps would therefore be an appropriate offset.

We will be using $r = 1/e$ because this gives consistency with the single-exponential decay time.

6.1 Structures with one well

The simplest possible quantum-well structure has one well. In structures with more than one well, carriers are generated in a distributed fashion across a larger region involving several wells. Carriers excited in one well will affect the absorption for the other wells. Furthermore, the wells will contribute different amounts to the total absorption change. One-well structures are useful to look at because during optical excitation, carriers are generated in the smallest possible spatial region, and only one well contributes to the absorption. For those reasons, the results are simpler to interpret and provide a more clear picture of the basic carrier sweep-out dynamics.

6.1.1 Position of the well

Changing the position of a well influences the sweep-out dynamics because the distances to the two contacts change. Simulations of the sweep-out in structures with one well placed at various points in the intrinsic region can therefore provide information about the bulk transport. They can also provide information about the influence of the position of the well on the induced absorption change.

In the following, three structures are considered. They are unstrained, with $In_{0.79}Ga_{0.21}As_{0.45}P_{0.55}$ barriers and $In_{0.53}Ga_{0.47}As$ wells. Figure 6.1 shows the banddiagrams for the three structures. The nominal width of the intrinsic region is 320 nm for all the structures. The band line-up is a constant 43/57 line-up (see Sec. 4.8.1). The depth of the electron well is 126 meV, and the depth of both hole wells is 167 meV. The band gap energy in the structures is 0.75 eV (1650 nm). Table 6.1 gives the distances to the two contacts in each of the three structures (the distances are measured from the middle of the wells). The bias is -0.27 V in all cases, and the structures are pumped and

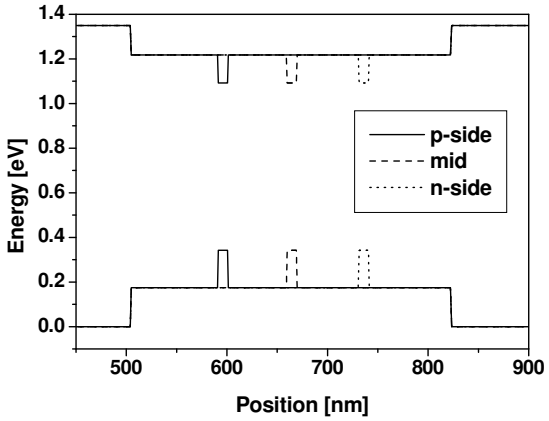

Figure 6.1: Banddiagrams for "p-side", "mid", and "n-side" structures, all of which have one well. The well is placed differently in the three structures.

probed at 1600 nm. Because the width of the intrinsic region is the same in all three structures, the field across the intrinsic regions will also be the same before excitation. Consequently, the absorption coefficient, the escape times from the wells, and the drift velocities are the same in all three structures before excitation. The excitation pulse energy is 0.5 pJ, which gives a carrier density of $\approx 1.5 \cdot 10^{15}$ m^{-2} in the wells. We have assumed that there is no recapture of carriers (see page 48 for a definition).

Figure 6.2 shows, on the left, the absorption recovery in the three structures; in the middle, the field contributions to the absorption changes; and on the right, the band filling contributions to the absorption changes. The

	"p-side"	"mid"	"n-side"
Distance to p-side [nm]	90	160	230
Distance to n-side [nm]	230	160	90

Table 6.1: Distances to p- and n-contacts in the three structures "p-side", "mid", and "n-side". The total width of the intrinsic region is the same in all cases: 320 nm.

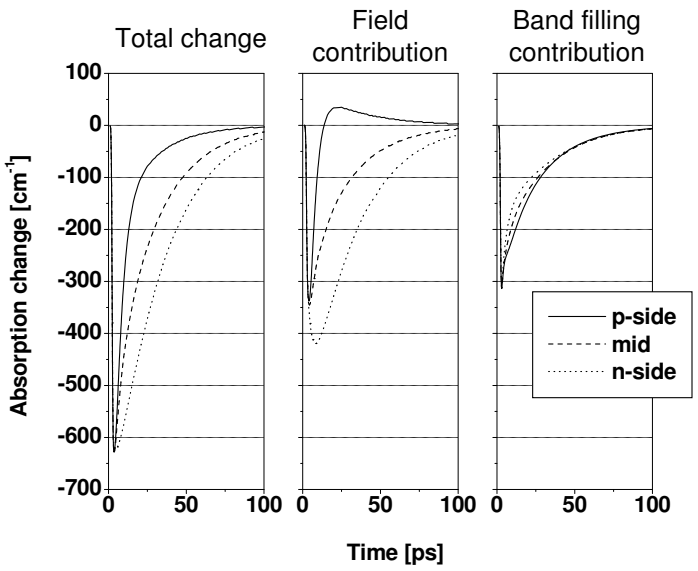

Figure 6.2: Absorption changes in the three one-well structures with different positions of the well. The field and band filling contributions are also shown. The excitation pulse energy is 0.5 pJ for all three structures.

behavior of the total absorption recovery is very different in the three structures, whereas the band filling contributions to the absorption changes in the three structures are very similar. The differences in the total absorption for the three structures are therefore mostly due to the field contributions to the absorption changes.

The differences seen in the band filling contributions in the three structures (Fig. 6.2 (*right*)) result because the field-changes across the wells are different in the three structures. These field changes are shown in Fig. 6.3. The field changes affect the escape times for holes and electrons (which are 25.7 ps and 3.4 ps, respectively, before excitation), and they affect the densities of states. The background for the differences in the *field changes* will be discussed in a moment.

For the "p-side" structure the band filling contribution and the field contribution to the absorption change conspire to give a faster absorption recovery in this structure than in the two other structures. This means that

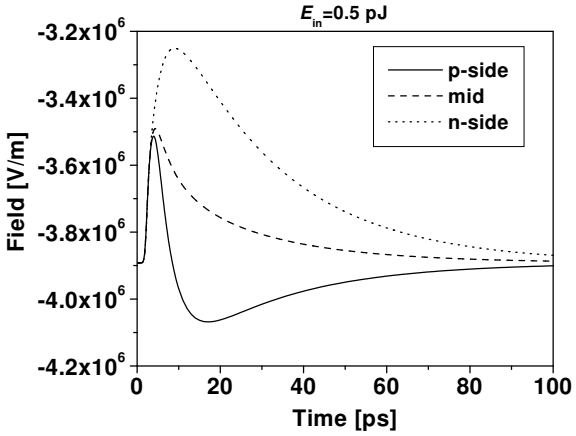

Figure 6.3: Field recovery for three one-well structures with different positions of the well.

of the three structures the "p-side" structure provides the shortest switching window. However, because the band filling contributions essentially are the same for the three structures, the maximum bit rate at which they can operate in a systems application will be pratically the same for all three of them. Below this bit rate the "p-side" structure will be preferable.

Boundary conditions for the field

The electrostatic potential is assumed to be constant across the diode (see Sec. 4.10). Thus, if $E(x;t=0)$ is the field distribution before excitation and $E(x;t)$ is the distribution at time t, then

$$\int_0^L [E(x;t) - E(x;t=0)]\, \mathrm{d}x = 0 \tag{6.5}$$

where the limits of integration mark the p-contacting point ($x = 0$) and n-contacting ($x = L$) point of the epitaxial structure. Since holes escape more slowly from the well than electrons, there will be a positive charge-density contribution at the well, and this will induce a change in the field through Eq. (4.5). On either side of the well the field must adjust to ensure that Eq. (6.5) is fulfilled.

For the argument below we will assume that the field is constant on both sides of the well (see Fig. 6.4), and denote by ΔE the field change induced by the carriers in the well. This field change is almost the same in the three structures, at least before the carriers reach the contacts. The change ΔE is split with a fraction s on the p-contact side of the well and $(1-s)$ on the n-contact side of the well. Because we have assumed that the field is constant on both sides of the well, we can approximate Eq. (6.5) by

$$d_p s \Delta E - d_n (1-s) \Delta E = 0 \tag{6.6}$$

where d_p is the distance from the well to the p-contact, and d_n is the distance to the n-contact. From Eq. (6.6) we find

$$s = \frac{d_n}{d_p + d_n} \tag{6.7}$$

Depending on the position of the well, the field on either side will change according to this ratio. In the "p-side" structure, where the well is closer to the p-side, we have $s = d_n/(d_p+d_n) > 1/2$ and thus the field change on the p-contact side of the well is larger than the field change on the n-contact side of the well. Vice versa for the "n-side" structure. The actual field distributions before excitation and at $t = 8$ ps are shown in Fig. 6.4. The arrows show the position of the well in each structure. The average field across the well in each structure can be seen in Fig. 6.3.

The argument above explains why the field changes across the wells are different for the three structures (keep in mind that ΔE is almost the same in the three structures). It implies that if the electron escape time were longer than the hole escape time, the field changes would have been reversed (in a qualitative, not a quantitative sense) compared to those shown in Fig. 6.3: The field on the p-contact side of the well would be reduced, and the field on the n-contact side would increase.

Details of the sweep-out process

Table 6.2 shows the ($r = 1/e$, $t_0 = 2.5$ ps) decay times for the three structures, based on various variables.

If the recovery times are found from the total absorption changes, as is typical in a single-pulse pump-and-probe experiment (where this is the only accessible parameter), the "p-side" structure is found to be the fastest by

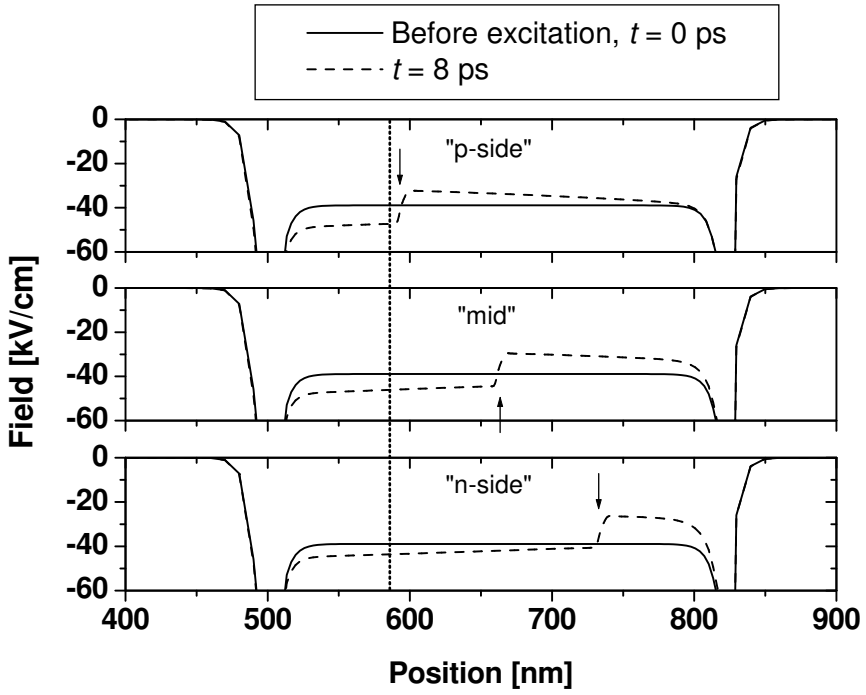

Figure 6.4: Field distributions in the three one-well structures with different positions of the well. The fields are shown for times $t = 0$ ps (that is, before excitation), and at $t = 8$ ps. The arrows mark the position of the well in the structures. The vertical, dotted line marks $x = 585$ nm. This point is used in the section that discusses the details of the sweep-out.

far (as mentioned previously) and the "n-side" structure is found to be the slowest. If the field contributions to the absorption changes are considered, the same picture results, although the "p-side" structure is now even faster, and the "n-side" structure is even slower than if measured using the total absorption change. If the field changes are considered, the "mid" structure is found to have the fastest recovery. Finally, measuring the decay using the band filling contributions to the absorption changes tells us that the "p-side" structure has the slowest recovery, and that the "n-side" structure has the fastest recovery.

It is clearly not easy to find a recovery time using either the field or the

absorption changes. It turns out that all of the results above are erroneous.

Before excitation, the hole and electron escape times are 25.7 ps and 3.4 ps, respectively. As the hole escape time thus is long compared to both the electron escape time and to the transport time across the intrinsic region, the escape of carriers from the hole well will be the limiting factor for the transport out of the intrinsic region. It is clear that the absorption can not recover until all carriers have been removed from the wells, and thus the band filling contribution to the absorption change represents most precisely the "recovery".

To gain a better understanding of the sweep-out in the three structures, it is useful to look at the transport within the intrinsic region. Figure 6.5 shows the carrier density of holes measured at a certain point in the intrinsic region as function of time. We will refer to this as the "3D pulse". The point at which we measure the 3D pulses is indicated by the vertical, dotted line in Fig. 6.4.

The differences between the 3D pulses in the three structures are immediately explained by the drift transport times. Compared to the "p-side" structure, there is an extra distance in the "mid" and "n-side" structures to the point at which the 3D pulses are measured. The extra distances are +70 nm and +140 nm, respectively, for the two structures. Using Fig. B.1 we find a hole velocity of $\approx$ 38 nm/ps at $E \approx 39$ kV/cm, the field in the three structures before excitation. At this velocity, 70 nm is covered in a little more than 1.84 ps. In Fig. 6.5, the inset shows the 3D pulses when the "mid" and "n-side" curves are displaced by -1.84 and -3.68 ps, respectively, corresponding to the extra transport times to the point of measurement, $x = 585$ nm.

	"p-side"	"mid"	"n-side"
$\Delta\alpha_{\text{tot}}$	9 ps	23 ps	37 ps
$\Delta\alpha_{\text{field}}$	6 ps	23 ps	40 ps
ΔE	24 ps	15 ps	36 ps
$\Delta\alpha_{\text{band-fill}}$	22 ps	20 ps	16 ps

Table 6.2: Decay times found using various variables: The total absorption change, the field contribution to the absorption change, the field change, and the band filling contribution to the absorption change. The decay times are found using $t_0 = 2.5$ ps and $r = 1/e$.

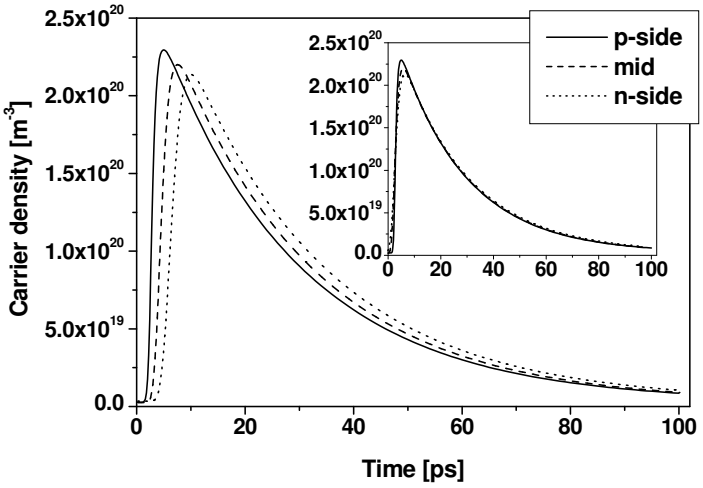

Figure 6.5: Carrier densities measured as function of time at $x = 585$ nm — this point is marked by the dotted line in Fig. 6.4. The inset shows the carrier densities when we adjust for the differences in transport times from the point of measurement to the well in each of the structures.

When this adjustment is made, the three 3D pulses appear very similar, and the tails of the curves almost coincide (the latter is not easy to see from the figure).

The simple, but important implications are that the sweep-out times are almost the same in the three structures and that the differences are almost entirely accounted for by the drift transport-time differences between the three structures. Above, it was concluded that the estimates of "recovery times" listed in Table 6.2 are wrong. The conclusion was based on the fact that the results are inconsistent; the decay times depend on which variable we choose to represent the "recovery". Having discussed above the detailed hole sweep-out, it is even more clear that these estimates are wrong. From the extra distance and the hole velocity, a difference in transport times from the well to the p-contact of about 3.6 ps was found between the "p-side" and "n-side" structures. The decay times found using the 3D pulses shown in Fig. 6.5 are 23.5 ps, 24.8 ps, and 26.7 ps for the "p-side", the "mid", and the "n-side" structures, respectively (all times are calculated relative to the

peaks of the 3D pulses). Because electrons escape faster than holes and have a higher drift velocity, we conclude that the "p-side" structure has the fastest recovery.

Only the decay times found using the band filling contributions ($\Delta\alpha_{\mathrm{band-fill}}$ in Table 6.2) resemble the numbers above. Still, the band filling decay times incorrectly attributes the longest recovery to the "p-side" structure. Section 6.1.2 below will discuss the implications of these inconsistencies and how the combination of single-pulse pump-and-probe measurements with other characterization techniques can provide a more thorough characterization of the recovery.

With respect to device speed, we conclude that putting the well closer to the p-contact gives a higher speed. However, the optical overlap may depend on the well position, and this must be kept in mind before the position of the well is changed. Note that if holes escape *faster* from the well than electrons, the conclusion with respect to device speed may be different from the one above.

Figure 6.4 showed that the field change across a well depends on the well's position. However, the excitation energy used in Fig. 6.4 is relatively low, and thus field-induced changes in the transport parameters are not very important (small differences could be distinguished among the band filling contributions in Fig. 6.2). However, at higher power levels, the field-induced changes in the escape times from the well and in the carrier drift velocities will be large, and they will depend on the position of the well in the manner described above. Field-induced changes in various transport parameters will be investigated in later sections.

We also investigated the influence of diffusion on the transport time and found that it hardly affects the transport to the contacts, but causes a slight smearing of the front edge of the 3D pulses. Diffusion mostly affects the dynamics at heterobarriers as discussed in Sec. 5.4.

6.1.2 Different measures of *recovery time*

An important consequence of the discussion above is that the actual recovery time is not so simple to obtain from a single-pulse pump-and-probe sweep-out measurement. Taking the total absorption change as a measure of the recovery, just as in a single-pulse pump-and-probe experiment, one might infer from Table 6.2 that the "p-side" structure could be used for operation almost up to 100 GHz. This is incorrect, as we discussed above.

The single-pulse characterization should be combined with other ways of characterizing the recovery. One way is to make a pump-and-probe experiment in which a modulated (for instance sine-modulated) optical pump is used to periodically generate carriers. The modulation amplitude on a transmitted probe provides information about the slower components of the recovery. The periodic pump ensures that the charging effects that slower components of the recovery give rise to are also revealed. This is illustrated schematically in Fig. 6.6. The left part of the figure shows the normalized pump amplitude at three bit rates: 10, 20, and 40 Gbit/s (each normalized to have unity maximum amplitude). On the right, the transmitted optical probe is illustrated for the three bit rates. These are normalized using the amplitude of the 10-Gbit/s probe transmission. At low frequencies, the modulation amplitude of the transmitted probe will be independent of the excitation frequency, as carriers have ample time to escape during a pump cycle. This is illustrated by the 10-Gbit/s signal (the cycle duration is 100 ps at 10 Gbit/s). When the cycle duration comes close to the carrier sweep-out time, carriers will just barely have time to escape from the wells, and charging effects due to slower components of the recovery will start to affect the modulation amplitude, reducing it. This is illustrated by the 20-Gbit/s case (cycle duration: 50 ps) in Fig. 6.6. When the frequency is increased further, carriers are unable to escape within the cycle duration. They accumulate within the structure, where they impede modulation of the carrier density. Thus, the modulation amplitude of the transmitted probe will be small, as illustrated by the 40-Gbit/s case in Fig. 6.6. At 40 Gbit/s, the cycle duration is 25 ps.

The experiment described above is almost exactly the method by which all-optical wavelength conversion is performed using the electroabsorption modulator (all-optical wavelength conversion was discussed in detail in Chapter 3). The advantage of the method described above is of course that it involves also those carriers that might remain in the structure after the absorption, when measured in a single-pulse pump-and-probe experiment, *apparently* has recovered. Characterization of the speed of a device should therefore involve not only a temporal resolution of the absorption change, as obtained with a single-pulse pump-and-probe technique, but also a periodic-excitation measurement that accesses the longer sweep-out components.

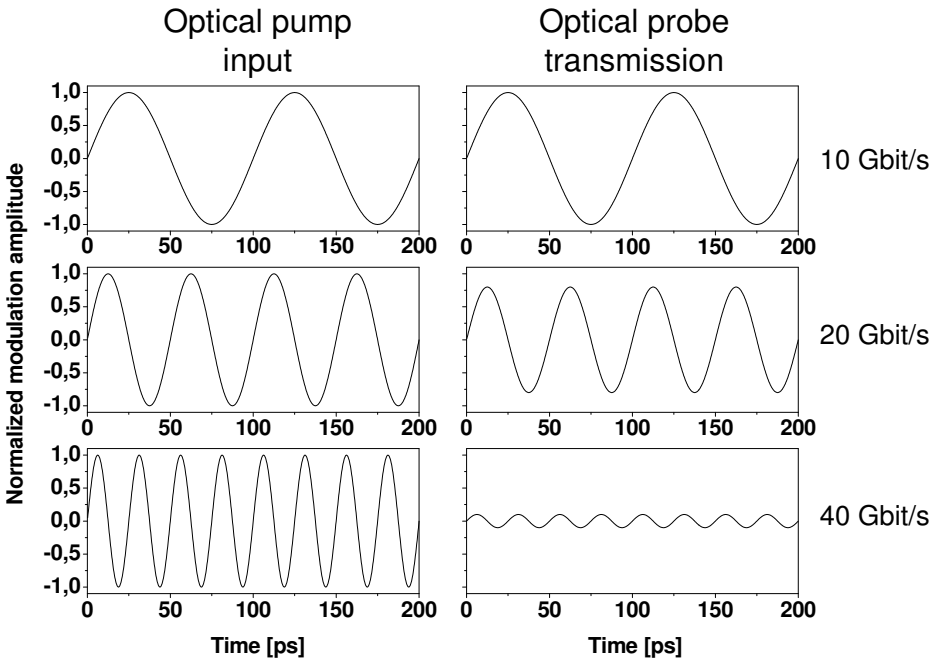

Figure 6.6: Schematic illustration of the response of a device at different excitation frequencies. The optical pump drives the absorption change, and at low speed (illustrated as 10 Gbit/s) the optical probe transmission has the highest obtainable modulation amplitude. As the pump frequency is increased, the device response decreases due to carrier accumulation.

6.1.3 Width of the intrinsic region

The width of the intrinsic region also influences the sweep-out process. As discussed in Sec. 6.1.1, the distance to the contacts influences the recovery time.

To investigate the influence of the width of the intrinsic region on the sweep-out process, the absorption recovery is calculated for the three structures shown in Fig. 6.7. The widths of the intrinsic regions are given in Table 6.3. Structure "Medium" is exactly the same as structure "mid" from Sec. 6.1.1, and the bias is the same, -0.27 V. For the two other structures,

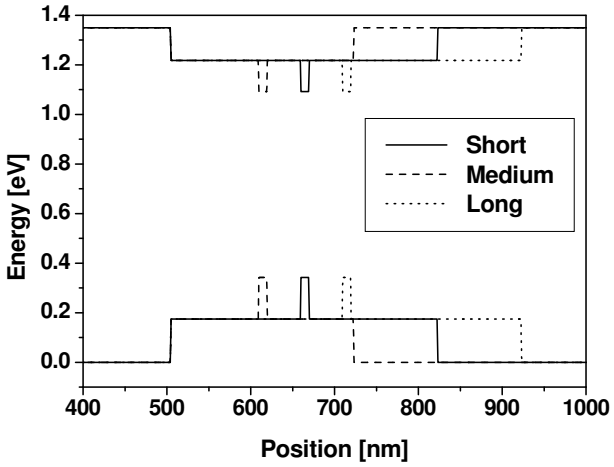

Figure 6.7: Banddiagrams for structures "Short", "Medium", and "Long". Each structure has one well. The width of the barriers is varied. Within each sample, the barriers on the two sides of the well have the same width.

"Short" and "Long", the bias is adjusted in each case to give the same field across the wells as in the "Medium" structure. The biases are given in Table 6.3. Adjusting the biases ensures that both the absorption coefficients, the escape times, and the drift velocities are the same in the three structures before excitation. The absorption is pumped and probed at 1600 nm with an excitation pulse energy of 0.5 pJ. This gives a carrier density in the wells of $\approx 1.5 \cdot 10^{15}$ m^{-2}. We have assumed in these calculations that there is no recapture of carriers.

	"Short"	"Medium"	"Long"
Width of i-region [nm]	220	320	420
Bias [V]	0.12	-0.27	-0.66

Table 6.3: Width of the intrinsic region for the three structures "Short", "Medium", and "Long". The biases applied to the three structures are also given.

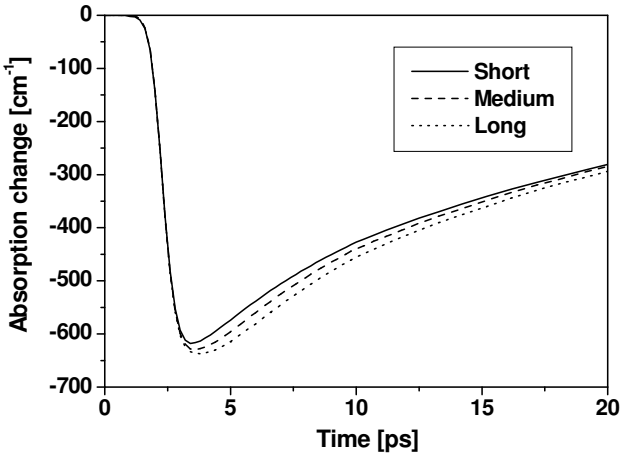

Figure 6.8: Absorption change for three one-well structures with different intrinsic-region widths. The pulse energy is 0.5 pJ. The absorption is pumped and probed at 1600 nm.

Figure 6.8 shows the recovery of the absorption in the three structures after excitation. The differences in the absorption recovery for the three structures are quite small. The field contributions to the absorption changes (not shown) account for most of the differences between the curves. Consistent with the discussion in Sec. 6.1.1, drift accounts for most of the differences in the sweep-out times (the 3D pulses are only quantitatively different from those in Fig. 6.5, and are therefore not shown). The distance to each of the contacts in the "Long" structure is only 100 nm longer than that in the "Short" structure. For holes, which move more slowly than the electrons, this extra distance is covered in ≈ 2.6 ps (the carrier velocities are shown in Fig. B.1 – the field is ≈ 39 kV/cm).

The main difference between the three structures is found in the magnitude of the field change. Figure 6.9 shows the changes in field with time for the three structures. The peak field-change is about 19 % and 38 % larger for the "Medium" and "Long" structures, respectively, compared to the peak field-change in the "Short" structure. The nominal widths of the intrinsic regions in the "Medium" and "Long" structures are about 45 % and 90 %

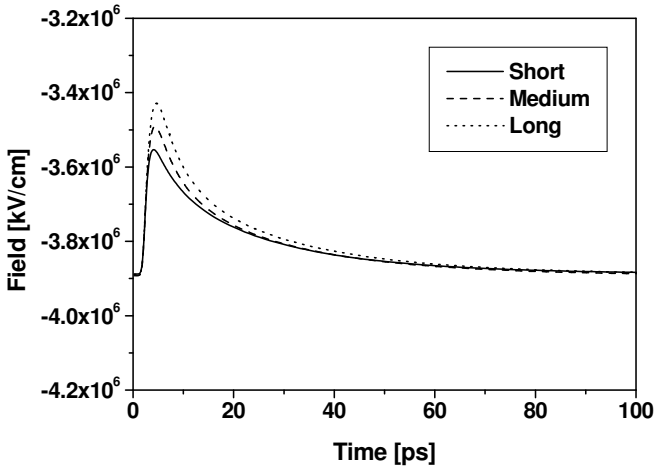

Figure 6.9: Field recovery for three one-well structures with different intrinsic-region widths.

larger, respectively, than the intrinsic region in the "Short" structure. It is clear that the field screening magnitude and the intrinsic-region width are correlated. The reason is that the number of carriers that contribute to the field screening is larger, the wider the intrinsic region is. As a first approximation, the number screening carriers is proportional to the distance to the contacts. However, the situation is not quite that simple. Because carriers pile up at the separate-confinement heterobarriers, and because the structures are excited by relatively short pulses, carrier pile-up will affect the field screening. This can be understood qualitatively from this simple picture: If carriers were unable to pass the separate-confinement heterobarriers, the field screening at $t = \infty$ would be (very closely) the same in the three structures. If there were no heterojunctions (or if there were junctions, but just no pile-up), the screening would be proportional to the distance to the contacts. The barriers are of course finite in our structures, and piled-up carriers are continuously being drained away across the heterojunctions. The field screening is therefore somewhere between being equal for the three structures (which is the case if carriers cannot cross the heterojunctions), and being proportional to the distance to the contacts (which is the case if there are no junctions,

or if carriers just do not pile up at them).

Figure 6.9 also shows that the field change initially is the same in all three structures. This is the regime where carriers have not yet reached the contacts even in the "Short" structure. More specifically, electrons have not reached the n-contact. Electrons escape significantly faster than holes, and they move faster in the field. Thus, they will reach the n-contact faster than the holes will reach the p-contact (escape times are quoted on page 106, and the drift velocities may be found in Fig. B.1). Once carriers reach the contacts in the shortest structure, their removal provides a term that acts to reduce the field change. Note, however, that the field change may still increase if more carriers escape from the well than are being drained at the contacts. This explains both why the peak field change is larger and why it occurs later as the width of the intrinsic region is increased: More carriers escape from the well before draining at the contacts sets in. By the argument given above, the field change for the "Medium" and "Long" structures are the same in the beginning until carriers reach the contacts in the "Medium" structure.

The conclusion in this section has implications for both electrical and optical modulation. Because the field change is larger, the wider the intrinsic region is, switching energies in all-optical applications will decrease if the width of the intrinsic region is increased. This of course comes at a price, in this case the price is an extra ≈ 2.6 ps of transport time across the intrinsic region in the "Long" structure compared to the "Short" structure. This extra time of course affects the electrical modulation speed in the same way.

6.2 Bias dependence

In this section, the influence of the bias on the absorption recovery is investigated. The "mid" structure from Sec. 6.1, shown in Fig. 6.1, is used for these simulations.

Figure 6.10 shows for different reverse biases the recovery of the absorption after excitation. The absorption is pumped and probed at 1640 nm, the excitation energy is 0.5 pJ, and we have assumed that there is no recapture. Firstly, the figure demonstrates that the absorption change increases with bias. This is due to the quantum-confined Stark effect. Secondly, the figure shows that the recovery time decreases when the bias is increased. An increase in the bias leads to an increase in the field across the well. This will

lower the effective well barrier and cause carriers to escape faster from the wells (see Eq. (4.23)).

There is also a change in the electron and hole drift velocities when the field is changed, but both velocities are typically so fast that the escape times from the wells, and not the drift velocities, are the limiting factors for the sweep-out rate. When the wells are very shallow, however, this conclusion is not correct. This is the subject of Sec. 6.2.1.

The conclusion in this section is that operation at higher biases is advantageous. The optically induced absorption change is higher, and the absorption recovers faster. These are attractive properties both for electrical and optical applications. These conclusions are well known, and have been drawn many times based on measurements.

Especially for all-optical applications, where a high optical power is necessary to induce the required absorption change, a certain minimum bias is

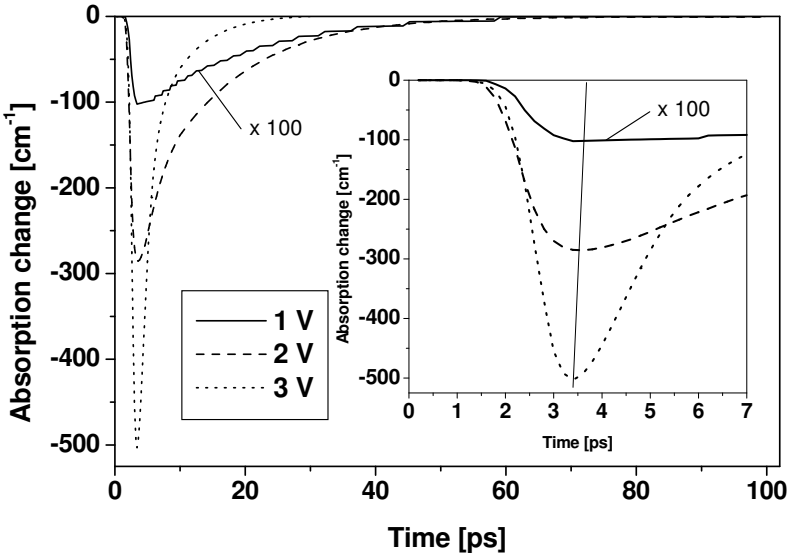

Figure 6.10: The absorption change as function of bias for a structure with one well. The decrease in recovery time for increasing bias is due to reduced escape times from the wells. The bias change also causes a change in the absorption. (The curve for 1 V is a bit "noisy" because the absorption changes are close to PinSim's absorption resolution, which is about 0.1 cm^{-1} per well.)

required for carriers to be swept out within the allowed time (which is determined by the operation bit-rate). However, the bias should be only just high enough that the desired speed is obtained. For this bias, the switching power will be the lowest possible under the constraint that the recovery speed must allow operation at the desired speed.

For applications where the absorption is modulated electrically, the sweep-out times within the applied bias range must be low enough that photo-excited carriers can be removed within each pulse cycle.

6.2.1 Sweep-out from shallow wells

The carrier escape times from wells increase with well depth according to Eq. (4.23). In the present section, we calculate the sweep-out in a structure with shallow wells.

In Sec. 6.1.1 we investigated structures with $In_{0.79}Ga_{0.21}As_{0.45}P_{0.55}$ barriers and $In_{0.53}Ga_{0.47}As$ wells. In the present section, we use the "mid" structure, but with $y = 0.6$ in the barrier instead of $y = 0.45$, still lattice-matched (see Eq. (4.6)). Again, we use a constant 43/57 line-up. This results in an electron well 37 meV deep and a hole well 49 meV deep. The structure is pumped at 1290 nm and probed at 1300 nm, and the excitation energy is 0.5 pJ.

Figure 6.11 shows the recovery for applied biases -1 V, -2 V, and -3 V. The decay time is between 2.5 and 3 ps for all three biases, showing that the absorption recovery in a shallow-well structure can be extremely fast. This is not too surprising, as the barrier height for both electrons and holes are on the order of the thermal energy and the optical phonon energy. The electron escape time is around 100 fs and the hole escape time around 250 fs. Because the escape times are this short, the band filling contribution to the absorption change is very small. Carriers are channeled essentially directly into the barriers where they contribute to field screening. In the present calculations, the field contribution to the absorption change accounts for essentially all of the total absorption change for all three biases. For this reason, the break-up of the absorption changes into field and band filling contributions is not shown.

With recovery times of a few picoseconds and escape times in the 100-fs range, it is clear that escape from the well is not the rate-limiting factor. Instead, transport across the intrinsic region, and to some extent transport across the heterobarriers, determine the absorption recovery in the fashion

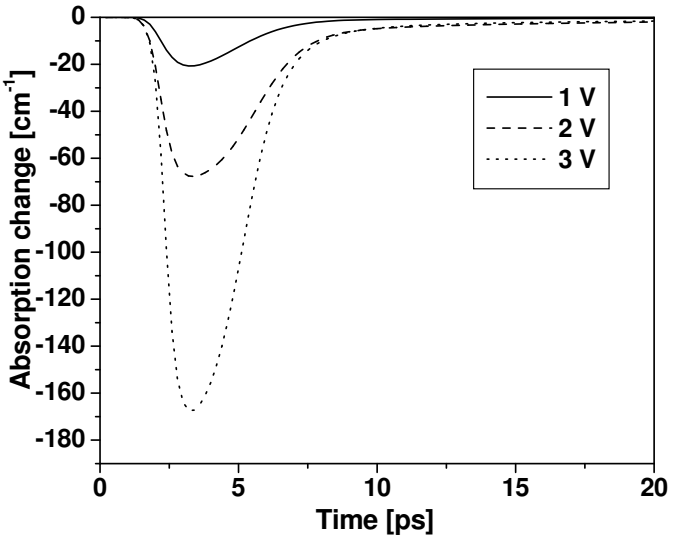

Figure 6.11: Recovery as function of bias for a well with $y = 0.6$ and barriers with $y = 0.45$. The structure is pumped at 1290 nm and probed at 1300 nm, and the excitation energy is 0.5 pJ.

described in Sec. 6.1.1. Looking closely at Fig. 6.11, we see a tail with a somewhat longer decay time than that which characterizes the initial recovery behavior 5 to 10 ps upon excitation. This slow component is related to charging effects (carrier pile-up) at the heterojunctions. The charging effects cause the effective response time of the structure to be longer than the decay time that characterizes the initial, partial recovery. Periodic-excitation pump-and-probe simulations are required to determine the importance of these slow components. We refer to Sec. 6.1.2 for a discussion of one such method. The influence of the heterobarrier design on the absorption recovery is discussed in more detail in Sec. 6.3.

Carrier escape from shallow wells was investigated by Feldmann *et al.* for GaAs/AlGaAs multi-quantum-well structures with 10-nm wide wells [168]. Although the material system is different, the depths of the wells in Feldmann *et al.*'s samples are comparable to the depths of the wells in our structure (the band offsets are of course somewhat different). Also the masses are comparable. Feldmann *et al.* found that even at a bias of only a few volts,

the *absorption decay times* were only a few picoseconds, limited mainly by transport away from the wells, not by escape out of the wells. Our results are completely in line with these observations. However, we use the term "absorption decay time" above to emphasize that the "sweep-out times" reported by Feldmann *et al.* really were decay times found in the manner described in the beginning of this chapter. The small, but long tails that we see in our simulations could well have been part of the recovery in Feldmann *et al.*'s structures without being distinguishable in the measurements.

Long tail or not, an important conclusion from the discussion above is that even for very shallow wells there is a lower limit for the absorption recovery time, determined by the width of the intrinsic region and by the carrier drift velocities. In our structures, the lower limit for the response time is a few picoseconds. If there are significant charging effects in the device, the effective sweep-out time will be determined not by the drift transport times but by the discharging of the heterojunctions.

6.3 Dynamics at heterojunctions

Heterobarriers affect the dynamics by causing a pile-up of carriers, which then screen the field. Calculations of the steady-state field screening in two structures with different separate-confinement heterostructures were presented and discussed in Sec. 5.4.

In this section, the sweep-out upon short-pulse excitation is investigated for the same two structures. The structures are shown in Fig. 5.14. As explained in Sec. 5.4, different biases are applied to the two structures in order to have the same field across the wells before excitation, thereby ensuring that the escape times and the drift velocities are the same in the two structures before excitation. The absorption is pumped at 1570 nm, and the excitation energy is 50 fJ.

Figure 6.12 shows the field recovery in the two structures after excitation. The field screening persists for much longer in the one-step structure than in the two-step structure. Figure 6.13 shows for various times the hole and electron densities in the intrinsic regions of the two structures. It is clear that the pile-up is much larger in the one-step structure than in the two-step structure. The long recovery time in the one-step structure is mainly due to holes, which pile up at the barrier close to the p-contact. Electrons also contribute to the screening, but less so. In the two-step structure there

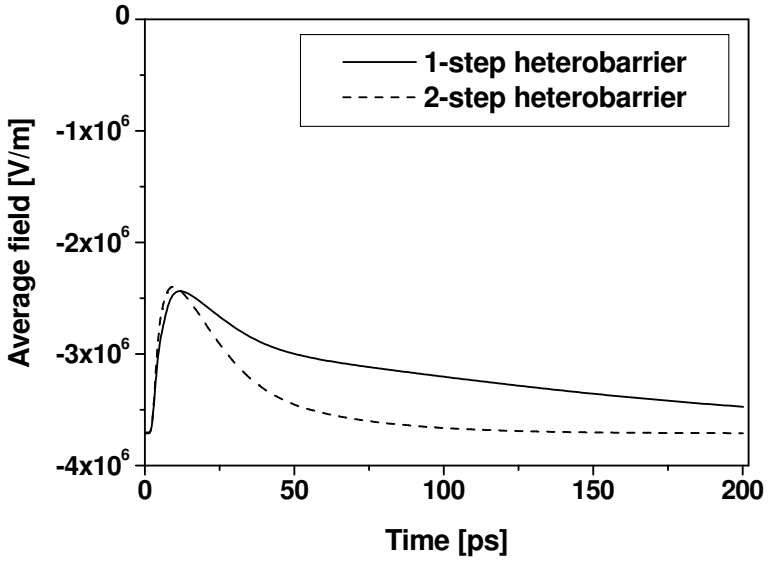

Figure 6.12: Field recovery after optical excitation in the two structures shown in Fig. 5.14.

is only a negligible pile-up. It is important to note that holes and electrons escape from the wells with different characteristic times. Thus, the hole pile-up comes about later than the electron pile-up, and the time-dependence of the pile-ups should therefore be considered independently for the two carrier types.

The widths of the intrinsic regions in the two structures are different. However, the intrinsic region in the two-step structure is only about 100 nm wider than that in the one-step structure, and the results in Sec. 6.1.3 showed that increasing the width of the intrinsic region by this much affects the sweep-out time only very little. Thus, the difference between the transport times to the separate-confinement heterobarriers is responsible for only an insignificant part of the differences seen in Fig. 6.12. We refer to Fig. 6.9 and to the discussion in Sec. 6.1.3.

The pile-up depends on the bias. In Sec. 6.4.1, the one-step structure will be investigated under a higher applied bias. At the higher bias, the pile-up is significantly reduced. From an application point-of-view, it is important

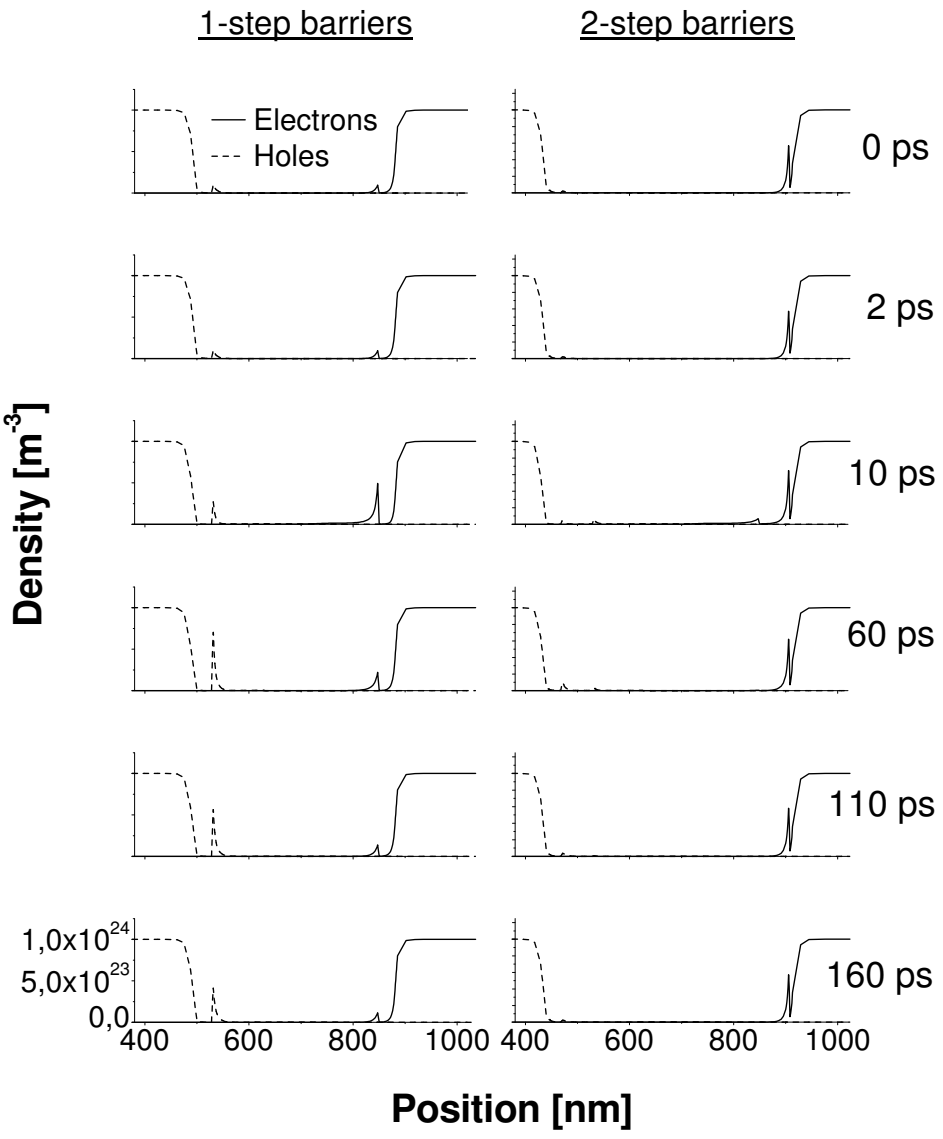

Figure 6.13: Electron and hole densities across the intrinsic regions in the one-step and two-step structures at various times.

to investigate how a specific design affects the operation. For electrical modulation, for instance, the applied bias is typically relatively low because the absorption band edge is steeper at smaller fields. This reduces the voltage swing required for operation. However, the low bias could result in carrier pile-up, if only in the low-bias end of the alternating-bias span.

For operation at very high speed, the dynamics at the heterojunctions must be examined closely. Even slight charging effects will reduce the device response time. Division of the heterobarriers into more steps than two should be considered if the response time is being limited by the transport dynamics at the separate-confinement heterojunctions.

6.4 Structures with several wells

Section 6.1 presented results of calculations on structures that had just a single well. Section 6.1.1, for instance, described for a structure with one well how the field and absorption behavior is affected when the well is moved from one place in the intrinsic region to another.

The present section discusses the dynamical behavior in structures that have more than one well. In such structures, carriers that are generated in one well will affect the dynamics at the other wells.

6.4.1 Detailed dynamics in a multi-quantum-well structure

In this section we investigate the distributed nature of the sweep-out in a multi-quantum-well structure. A structure with eight wells is considered. The structure is the one-step structure investigated in sections 5.4 and 6.3, and its banddiagram is shown in Fig. 5.14 (with label "1-step"). It is similar to the structures from Sec. 6.1.1, but it has eight wells instead of one. The applied bias is -2 V, and the absorption is pumped at 1600 nm. In the following calculations we assume that there is no recapture.

Figure 6.14 shows the field across each of the eight wells after excitation with a 0.5-pJ pulse. The wells are numbered starting from the p-contact side of the well region. As expected, the field change is different across the different wells. The essence of this behavior was discussed in Sec. 6.1.1. Adding seven extra wells is of course not a trivial change to a one-well structure. Still, the behavior for each of the wells is in qualitative agreement with what would

be expected from the one-well simulations when each well's position is taken into account.

Figure 6.14 also shows the average field across the entire well region. Not surprisingly, the average field experiences a decrease. However, if the wells were moved towards the p-contact, more wells would experience a field *increase*, and the average field would be reduced less and might even increase (we refer once again to Sec. 6.1.1). A field increase is not desirable for switching, where an absorption bleaching is sought. Moving the wells towards the n-contact instead would increase the field screening across the wells. This consideration is clearly important in the design of devices, especially devices for all-optical signal processing.

For voltage-modulation of the absorption, it might be desirable to move the wells closer to the p-side. When the field is high, the device has a large absorption (through the quantum-confined Stark effect). When carriers are excited, the field reduction *in the well region* will be smaller if the wells are closer to the p-side. As a consequence, the absorption reduction induced by the carriers through screening will also be smaller. The field might even increase, as illustrated by Fig. 6.2. A reduced field screening is also advantageous because it reduces the field-induced increases of the escape times (from the wells, that is). It is important to remember that moving the wells will change the confinement factors for the wells. If the confinement factors are reduced, then the modal absorption will decrease (see Eq. (4.47)). In reality, the confinement factor does not change all that much when the wells are moved 50 or 100 nm. However, if the absorption just barely is sufficient for the application in question, the position of the well region will be critical. In that case, the wells must be placed where the overlap between the optical field and the absorbing medium is maximum.

Figure 6.15 shows the field change upon excitation with a 5-pJ pulse. The qualitative behavior is similar to that in Fig. 6.14. However, the 5-pJ pulse excites a higher density of carriers, thereby causing a larger field screening and also a larger average field screening. Figure 6.15 also clearly shows that the carrier sweep-out takes longer. For Well 8, for instance, the field remains screened for a significantly longer time than after excitation with the 0.5-pJ pulse.

Figure 6.16 and Fig. 6.17 show the carrier densities in the eight electron and hole wells as function of time for the two excitation energies. Although the excitation pulse energy is ten times higher in the 5-pJ case than in the 0.5-pJ case, the densities of excited carriers are not ten times larger. This

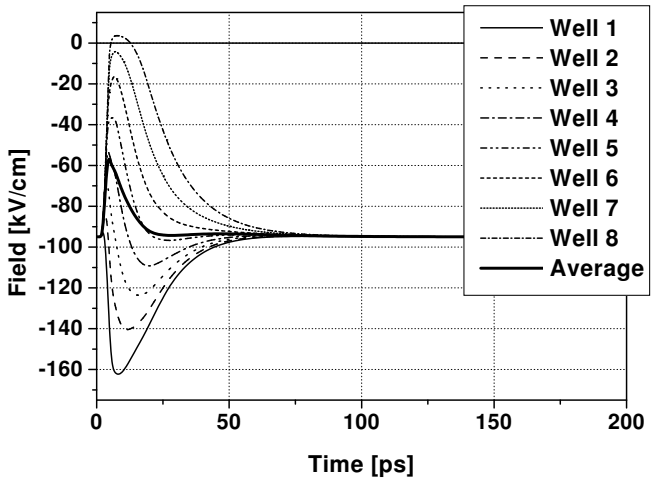

Figure 6.14: The field across each well in our eight-well structure excited by a 0.5-pJ pulse. The thick line is the average field.

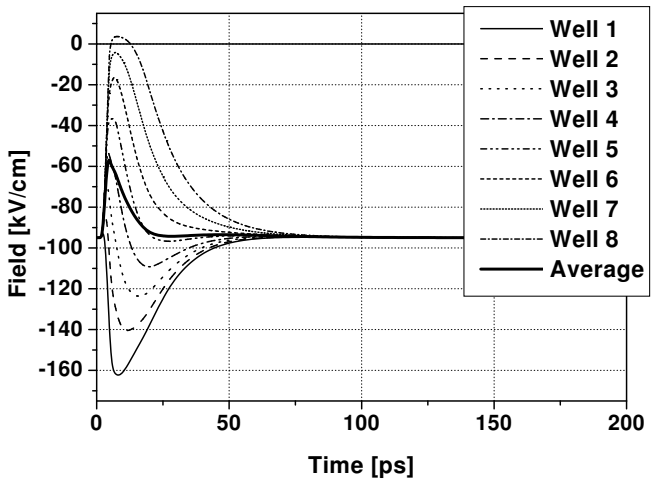

Figure 6.15: The field across each well in our eight-well structure excited by a 5-pJ pulse. The thick line is the average field.

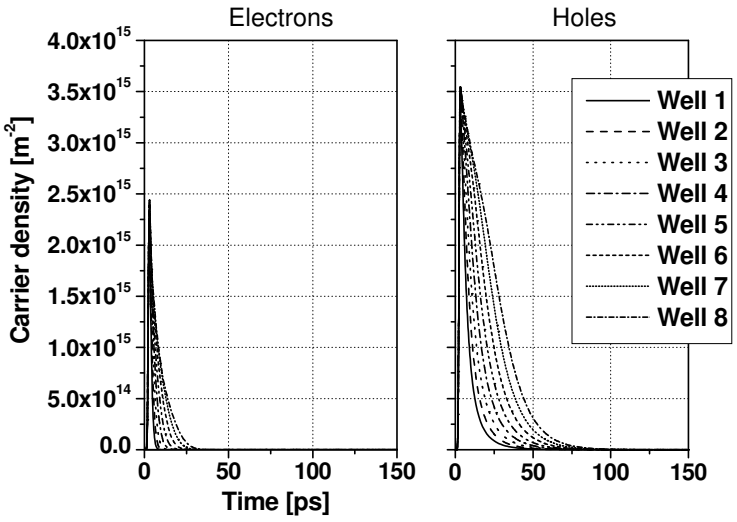

Figure 6.16: Carrier densities in the electron and hole wells as function of time. The excitation energy is 0.5 pJ.

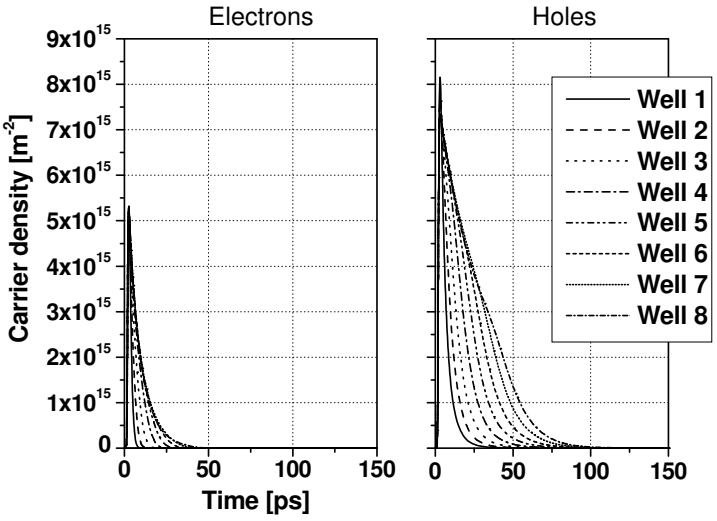

Figure 6.17: Carrier densities in the electron and hole wells as function of time. The excitation energy is 5 pJ.

is because the absorption is reduced through band filling effects during the excitation.

For each of the two energies, the difference in the carrier escape times from well to well is due to field screening. As shown by Fig. 6.14 and Fig. 6.15, the field increases at Well 1 (the well closest to the p-contact), changing gradually towards Well 8, where it decreases. The changes in the field modify the carrier escape times, as shown in Fig. 6.18 for the 0.5-pJ case, and these changes immediately explain the course of the escape seen in Fig. 6.16.

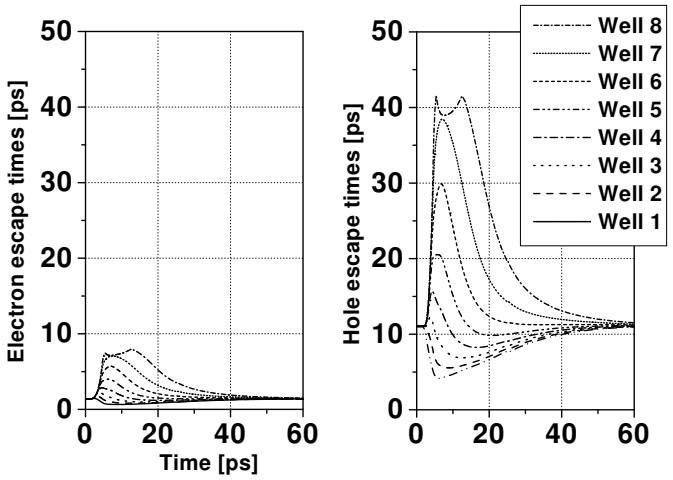

Figure 6.18: Escape times for electrons and holes. The excitation pulse energy is 0.5 pJ.

Finally, Fig. 6.18 illustrates the important fact that the escape time from a well *increases* faster when the field is screened than it *decreases* when the field is increased. Formally, $-\,\mathrm{d}\tau_{\mathrm{esc}}/\,\mathrm{d}F$ decreases with field, F; τ_{esc} is the escape time out of the well. This behavior is due to the exponential function in Eq. (4.23), which may be approximated as

$$\exp\left[\frac{E_{\mathrm{b}}-E_1}{k_{\mathrm{B}}T}\right] \approx \exp\left[\frac{FL_{\mathrm{QW}}/2-(E_b-E_1^{(0)})}{k_{\mathrm{B}}T}\right] \tag{6.8}$$

where L_{QW} is the width of the well, defined in Fig. 4.2; E_b is the barrier energy, which is illustrated in Fig. 4.3; and $E_1^{(0)}$ is the eigenenergy of the lowest bound state at zero field.

If the field across a well is screened substantially, the escape from that well might become the limiting factor for the sweep-out. This point emphasizes

the importance of considering carefully how the wells are placed within the intrinsic region.

6.4.2 Varying the number of wells

In this section we investigate the influence of the number of wells on the absorption dynamics. In the simulations, the intensity at each well is such that the product (number of wells) · (intensity at each well) is independent of the number of wells. This means that the intensity that excites a five-well structure is one-fifth the intensity that excites a one-well structure.

We investigate three structures in this section: A one-well structure, a three-well structure, and a five-well structure. The one-well structure is the same as the "mid" structure from Sec. 6.1.1. The three-well and five-well structures result by adding one and two extra wells, respectively, on both sides of the well in the one-well structure. The width of the barriers between the wells is 10 nm. The total width of the intrinsic region is the same in the three structures. The absorption is pumped and probed at 1600 nm, and we assume that there is no recapture.

Before embarking on the discussion of the results, let us mention that changing the number of wells will change the modal absorption. In our approximation, the modal absorption coefficient for a structure with n wells is $\sum_k \alpha_{\text{modal}}^{(k)}$ where $\alpha_{\text{modal}}^{(k)}$ is the modal absorption coefficient for well k (see Eq. (4.56)). This means that a larger fraction of the light is absorbed when the number of wells is increased. This is not our immediate concern, but we return to this issue when we look at transmission through the three structures.

Figure 6.19 shows the absorption change induced in the one-well, the three-well, and the five-well structures. The one-well structure is excited by a pulse with energy $E_p = 50$ fJ, the three-well structure by a pulse with energy $E_p/3$, and the five-well structure by a pulse with energy $E_p/5$. The field and band filling contributions are also shown.

We need some definitions in order to proceed. The *field-change* across well k in an n-well structure is $\Delta E_n^{(k)}$, and the *average field-change* is

$$\Delta E_n^{(\text{av})} = \frac{1}{n} \sum_k \Delta E_n^{(k)} \tag{6.9}$$

The *peak average field-change* is the maximum, in time, of the average field-change.

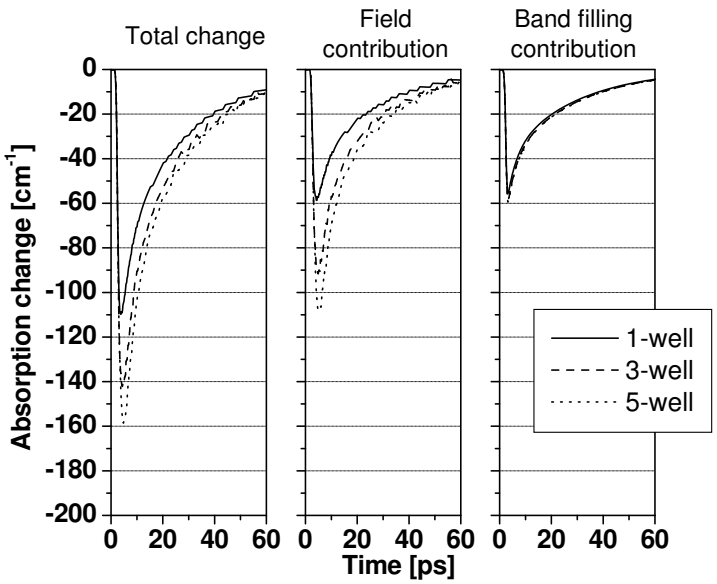

Figure 6.19: Absorption changes in the one-well, three-well, and five-well structures. The field and band filling contributions are also shown. The excitation pulse energy is 50 fJ for the one-well structure, 50/3 fJ for the three-well structure, and 50/5 fJ for the five-well structure.

The band filling contributions to the absorption changes are almost the same for the three structures. This is expected for low-energy excitation. The main difference in the total absorption changes for the three structures stems from the field-induced absorption changes. The field contribution to the absorption change is largest in the five-well structure. However, this should not be interpreted as being the result of a larger *average field-change*. Actually, the highest peak average field-change is found in the three-well structure, and the five-well structure has the *smallest* peak average field-change of the three structures. However, the field-induced absorption change is not determined by the average field-change, $\Delta E_n^{(\mathrm{av})}$, but by the total field change, $n\Delta E_n^{(\mathrm{av})}$. To see this, we calculate the absorption change for a structure with n wells.

The total absorption, α_n, can be written

$$\alpha_n(t) = \sum_k \alpha_n^{(k)}(t) \tag{6.10}$$

$$= \sum_k \left(\alpha_{n,0}^{(k)} + \Delta\alpha_{\text{band-fill}}^{(k)}(t) + \frac{\mathrm{d}\alpha}{\mathrm{d}E} \cdot \Delta E_n^{(k)}(t) \right) \tag{6.11}$$

where $\alpha_n^{(k)}$ is the contribution from well k, $\alpha_{n,0}^{(k)}$ is the absorption from well k before excitation, $\Delta\alpha_{\text{band-fill}}^{(k)}$ is the absorption change due to band filling for well k, and $\mathrm{d}\alpha/\,\mathrm{d}E$ is the derivative of the absorption coefficient with respect to electric field. We have assumed that $\mathrm{d}\alpha/\,\mathrm{d}E$ is constant. The total absorption change $\Delta\alpha_n$ is

$$\Delta\alpha_n(t) = \sum_k \alpha_{\text{band-fill}}^{(k)}(t) + \sum_k \frac{\mathrm{d}\alpha}{\mathrm{d}E} \cdot \Delta E_n^{(k)}(t) \tag{6.12}$$

$$= \sum_k \alpha_{\text{band-fill}}^{(k)}(t) + \frac{\mathrm{d}\alpha}{\mathrm{d}E} \cdot n \cdot \Delta E_n^{(\text{av})}(t) \tag{6.13}$$

We note that for $E_p = 50$ fJ, all three structures have approximately the same contribution to the absorption change due to band filling, as mentioned above. Therefore, the first term, $\sum_k \alpha_{\text{band-fill}}^{(k)}$, in Eq. (6.13) is approximately independent of the number of wells for $E_p = 50$ fJ.

Because the five-well structure has the highest value of $n\Delta E_n^{(\text{av})}$, it also has the highest field-induced absorption change. The average field-change in the one-well structure is, actually quite precisely, 1.6 times that in the five-well structure, at any time. Using Eq. (6.13) we expect the field contribution in the five-well structure to be $5/1.6 \approx 3.1$ times higher than that in the one-well structure. Figure 6.19 shows a factor closer to 2. The difference is due to the assumption that $\mathrm{d}\alpha/\,\mathrm{d}E$ is constant, when it is actually higher at lower fields.

When the excitation energy is increased, the band filling effects become more important. Because the intensity at each well in the calculations is inversely proportional to the number of wells, band filling will be most important in the structure with the fewest wells; here, this means the one-well structure. In the following, the energy of the pulse which is used to excite the one-well structure is increased to $E_p = 2$ pJ. The energy of the pulse that excites the three-well structure is still $E_p/3$, and the five-well structure is excited by a pulse with energy $E_p/5$.

Figure 6.20 shows the absorption changes in the three structures, together with the field and band filling contributions. As expected, the absorption change is lowest for the one-well structure. The larger absorption changes in the structures with more wells result because more carriers can be excited in those structures. The higher density of carriers increases both the field contribution and the band filling contribution to the absorption change.

Propagation effects

We found above that the absorption change is higher when the number of wells is increased but the product of intensity and number of wells is kept constant. However, a higher absorption change does not guarantee a higher modulation on-off ratio. The reason is that the lower modal absorption in a structure with fewer wells gives a longer effective interaction length.

In the following, we will express on-off ratios in terms of the *extinction*

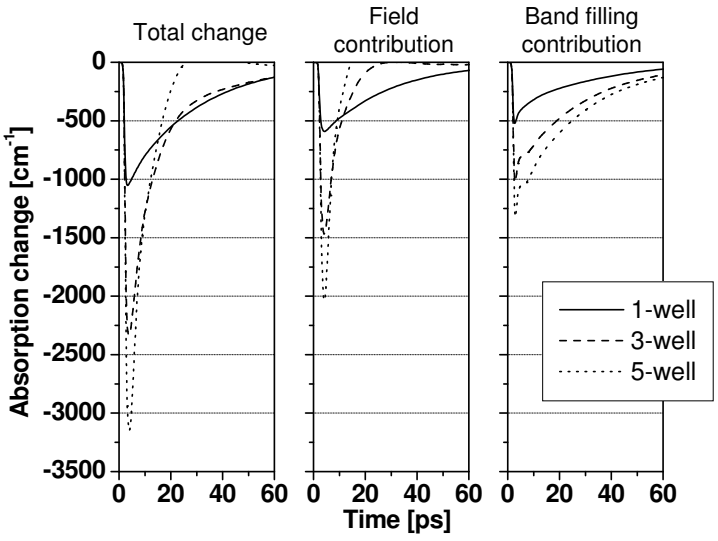

Figure 6.20: Absorption changes in the one-well, three-well, and five-well structures. The field and band filling contributions are also shown. The excitation pulse energy is 2 pJ for the one-well structure, 2/3 pJ for the three-well structure, and 2/5 pJ for the five-well structure.

ratio, ER, which is given by

$$ER = 10 \cdot \log \left(\frac{S_{\text{out}}}{S_{\text{out}}^{(0)}} \right) \tag{6.14}$$

where S_{out} and $S_{\text{out}}^{(0)}$ are the transmitted photon densities with and without optical excitation.

To take propagation effects into account, we assume that the induced absorption change is proportional to the local photon density. Table 6.4 shows the extinction ratios and insertion losses calculated for the three structures. The one-well structure is excited with a 2-pJ pulse, and the three- and five-well structures are excited with 2/3-pJ and 2/5-pJ pulses, respectively. We assume that the confinement factor $\Gamma = 0.02$ per well. When propagation effects are taken into account, the extinction ratio for a 100-μm long device is largest if the five-well structure is used. For a 200-μm long device, the three-well structure will provide the largest extinction ratio.

The insertion losses are also given in Table 6.4. The insertion loss, IL, is defined as

$$IL = 10 \cdot \log e \cdot \Gamma \alpha_n(t = 0) L_z \tag{6.15}$$

where L_z is the device length, α_n is the absorption coefficient, defined in Eq. (6.10), and $\Gamma = 0.02$ is the confinement factor, assumed to be equal for all the wells. The absorption coefficient before excitation is $\alpha_n(t = 0) = 1.4 \cdot 10^3$ cm^{-1}. We are not going to discuss the insertion losses in detail here, but we provide the figures as a reminder that the insertion loss is intrinsically related to the maximum attainable extinction ratio, to the number of wells, and to the device length, and must kept in mind when devices are being designed.

The results above show that for all-optical applications there is a number of considerations involved in optimizing a device. For a short device, a higher number of wells will provide a better extinction ratio. If a certain extinction ratio is required, then the device must either have a certain minimum length or a certain minimum absorption coefficient. As demonstrated above, the extinction ratio divided by the power level increases with the number of wells. In words: the extinction ratio increases faster than the number of wells.

This leads to the conclusion that for all-optical applications, structures with more wells are generally desirable. However, we showed that a device with fewer wells can be more efficient if the conditions are right.

	1-well	3-well	5-well
$L_z = 100$ μm			
ER [dB]	0.88	1.62	1.80
IL [dB]	1.22	3.65	6.08
$L_z = 200$ μm			
ER [dB]	1.69	2.57	2.39
IL [dB]	2.43	7.30	12.2

Table 6.4: Extinction ratios and insertion losses for the one-well, three-well, and five-well structures. The one-well structure is excited by a 2-pJ pulse. The extinction ratios and insertion losses are shown for device lengths $L_z = 100$ nm and $L_z = 200$ nm.

Furthermore, a structure with more wells may present other limitations. As shown in Fig. 6.4 (and discussed in detail in Sec. 6.1.1), the average field change across a well placed in the middle of the intrinsic region is low, but increases when the well is moved away from the center. The structures investigated in the present section are all symmetrical with respect to the placement of the wells in the intrinsic region. Some wells therefore experience a field increase, some experience a low change, and some experience a field reduction. Figure 6.14 illustrates this for a structure with eight wells. The escape times increase for the wells that experience a decrease in the field, which are those closest to the n-contact.[11] This was illustrated in Fig. 6.18 for excitation of an eight-well structure with a 0.5-pJ pulse. In the present section, the hole escape times before excitation are 25.7 ps for all wells in all three structures. After excitation with a 2-pJ pulse, the holes escape from the well in the one-well structure with a decay time of 22.0 ps (measured from the peak of the excitation).[12] For the well closest to the n-contact in the three-

[11] As discussed in Sec. 6.1.1, the direction of the field change depends on which carrier type remains longer in the wells. The field will decrease near the n-contact when electrons escape faster from the wells than holes. The situation will be reversed if electrons take longer to escape than holes.

[12] The cause of the escape time *decrease* for holes in the one-well structure may be found in Fig. 6.4, which shows that the field on the p-contact side of the well in the "middle" case *increases*. This gives a lower effective barrier for holes. (The field on the n-contact side is reduced, and therefore the escape time for electrons will be increased.)

well structure, the value is 31.5 ps, and for the well closest to the n-contact in the five-well structure, the decay time is 35.7 ps (still with the three-well structure being excited by a 2/3-pJ pulse, and the five-well structure by a 2/5-pJ pulse) At the lower pulse energy, 50 fJ (for the one-well structure), the corresponding values are 26.1 ps, 26.2 ps, and 26.2.

The higher escape times for wells close to the n-contact mean that the device speed may suffer when more wells are put into the intrinsic region. The number of wells should therefore be just high enough that the escape from the "slowest" well is fast enough for the required speed of operation. This puts an upper limit on the absorption change that the device can deliver. However, for the number of wells thus determined, the energy required for switching is the lowest possible (within the constraint that no more wells may be added).

6.5 Oversaturation

From the results presented earlier in this chapter, we can conclude that the power level influences the recovery time mainly through field-induced changes in the escape times from the wells. However, the calculations presented uptil now have been for moderate power levels. The present section concerns the dynamics at very high excitation levels.

We focus on Structure 1, which we presented in Sec. 5.1.1. The structure is biased at -1 V, and the absorption is probed at 1520 nm. We use Structure 1 here because of its particularly shallow wells, from which carriers escape very quickly. Before optical excitation, the escape time for electrons is 110 fs and the escape time for holes is 70 fs. Even with a completely screened field, the escape times do not exceed 450 fs. Thus, the issue of field-induced changes in the escape times is of little importance for the dynamics in this section.

Figure 6.21 shows the recovery for two different excitation energies, 10 pJ and 100 pJ, and two different excitation wavelengths, $\lambda_e = 1510$ nm and $\lambda_e = 1548$ nm. The absorption is higher at $\lambda_e = 1510$ nm than at $\lambda_e = 1548$ nm, and a considerably higher density of excited carriers results after excitation at the shorter wavelength. The four curves in Fig. 6.21 thus represent different densities of excited carriers.

In the 10-pJ, $\lambda_e = 1548$-nm case, the recovery is fast, below 20 ps. In this case, only field-induced changes in the dynamical parameters affect the

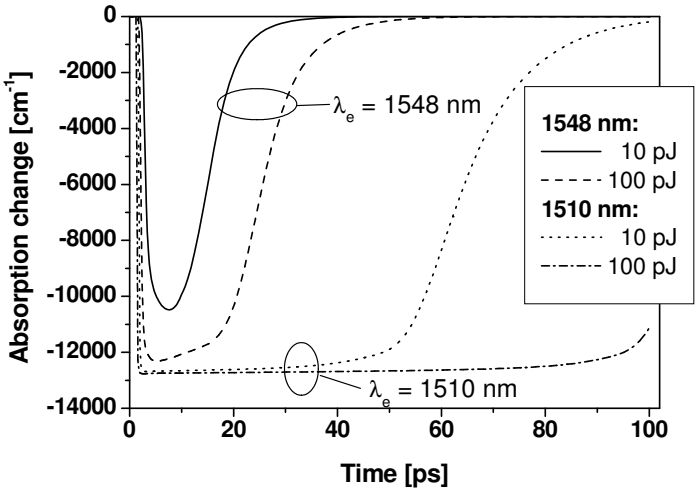

Figure 6.21: The figure shows the calculated absorption recovery after oversaturation. The recovery is shown for two different excitation wavelengths and two different pulse energies.

sweep-out time, which is just a few picoseconds longer than the low-energy sweep-out time. For excitation at the shorter wavelength and with an energy of 100 pJ, the recovery time is longer than 100 ps, several orders of magnitude longer than the escape times from the wells. The field-induced changes in the escape times are clearly not responsible for the long recovery time, as also mentioned above.

Instead, the long recovery time is the result of a special physical situation that comes about at very high carrier densities. Upon excitation, the field in the well region will be completely screened, and a quasi-equilibrium is established in which the sign of the charge density changes between positive and negative across the well region. This is due to an asymmetry between the densities of confined electrons and confined holes. It results in a field across the wells which changes sign near the middle of each well, as shown in Fig. 6.22. The field forces bulk carriers (that is, carriers in quasi-continuum states) toward the zero-field points; electrons toward the zero-field points in the barriers, and holes toward the zero-field points in the wells. From an energy perspective the change in the field direction corresponds to a potential

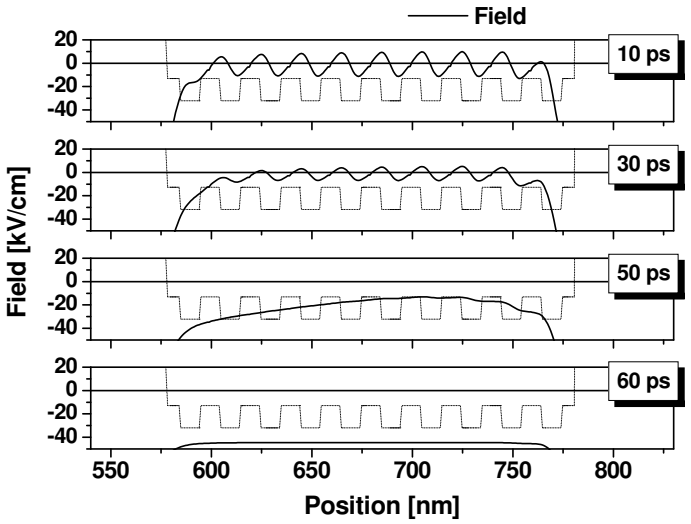

Figure 6.22: The figure shows the calculated field in the well region at different times after excitation at 1510 nm by a pulse with a high energy, 10 pJ. After the excitation, the field remains completely screened for some time due to the carriers themselves forming potential wells that impede carrier transport. For reference, the banddiagram is also shown.

well. The depths of the potential wells increase with the density of excited carriers and thus with excitation energy. Only near the edge of the well region, where the field is high, are carriers accelerated by the field. Due to the potential wells, carriers are removed only very slowly from the well region through a process where they diffuse out and are swept away by the field that exists outside the well region. However, the potential wells persist for a long time, as quantified in Fig. 6.21. With time, the depths of the potential wells are reduced, and as they are eliminated the transport becomes dominated by drift, and the recovery will therefore proceed fast. As mentioned above, the potential well depths increase with the density of excited carriers. Therefore, the plateau-part of the recovery, where the absorption is completely saturated, is longer for higher excitation energies. However, once the actual recovery sets in, it proceeds in almost the same fashion irrespective of the excitation pulse energy, as may be seen in Fig. 6.21.

Measurements of the absorption recovery as function of excitation pulse

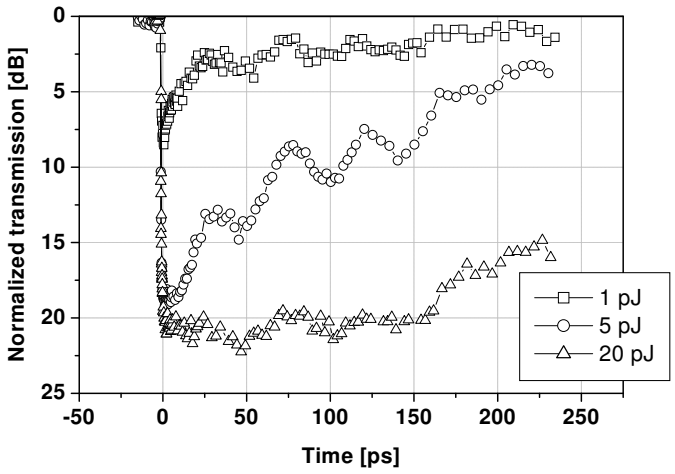

Figure 6.23: The figure shows the normalized transmission measured in a pump-and-probe experiment using 200-fs wide pulses at 1520 nm. The recovery is measured for three different excitation pulse energies.

energy were made by F. Romstad (COM) on a device with the same nominal epitaxial structure as our "Structure 1" (absorption spectra for this device were presented in Sec. 5.1.1). The device was biased at -3 V in the experiments. The absorption was pumped and probed at 1520 nm. The measurements are shown in Fig. 6.23. The origin of the oscillations seen in Fig. 6.23 has not been established, but there are indications that they are caused by the electrical circuit.

The measured recovery times are similar for excitation pulse energies of 1 pJ and 5 pJ. However, at 20 pJ the recovery takes much longer, more than 250 ps. We point out that the bias used in the experiment is different from the one used in the calculations.

Propagation effects are important at the lower pulse energies. However, in the 20-pJ measurement the device is saturated through its entire length, and the absorption coefficient is therefore more uniform through the device in that measurement than in the measurements for lower pulse energies. Thus, our calculations should be compared to the experiment that uses the 20-pJ pulse, and it is clear that there is a good qualitative agreement between the

calculations and the measurements. For an energy five times higher than the one used in the experiment, we predict a recovery time which is somewhat shorter than the measured value. The differences between the measured and the calculated results have not yet been explained. To do this, a more detailed analysis of the influence of various parameters on the sweep-out after oversaturation is required.

Note that the recovery time does not scale with the excitation pulse energy (this is hardly surprising). The calculated recovery time is close to 70 ps for excitation at $\lambda_e = 1510$ nm with a 10-pJ pulse, and it is ~ 120 ps for excitation with a 100-pJ pulse. With those numbers, we cannot expect to be able to reach a 250-ps sweep-out time (as in the experiment) just by increasing the excitation pulse energy. Other explanations must be sought for the differences between the measurements and our calculations.

To compare the experiments for lower pulse energies to our calculations requires us to take propagation effects into account. We have not yet done this.

6.6 Influence of recapture on the sweep-out dynamics

In Sec. 5.3 we discussed the saturation properties both with thermionic recapture and with no recapture. We also suggested that recapture might not be important on a short time scale. In the present section, we investigate how the degree of recapture influences the sweep-out. The simulations concern Structure 1, which we presented in Sec. 5.1.1.

Figure 6.24 shows the absorption recovery for applied biases of 0 V and -4 V. The absorption is pumped at 1510 nm when the bias is 0 V, and at 1550 nm when the bias is -4 V. The absorption is probed at 1520 nm in both cases. The recovery is calculated both with thermionic recapture and with no recapture.

Figure 6.24 clearly shows that at 0 V the presence of thermionic recapture increases the recovery time significantly compared to the case with no recapture. At -4 V, the recapture process does not affect the dynamics significantly. This is because the increase of the field across the wells reduces the escape times, which results in a higher net escape rate.

Presence of capture could explain measurements where escape times are

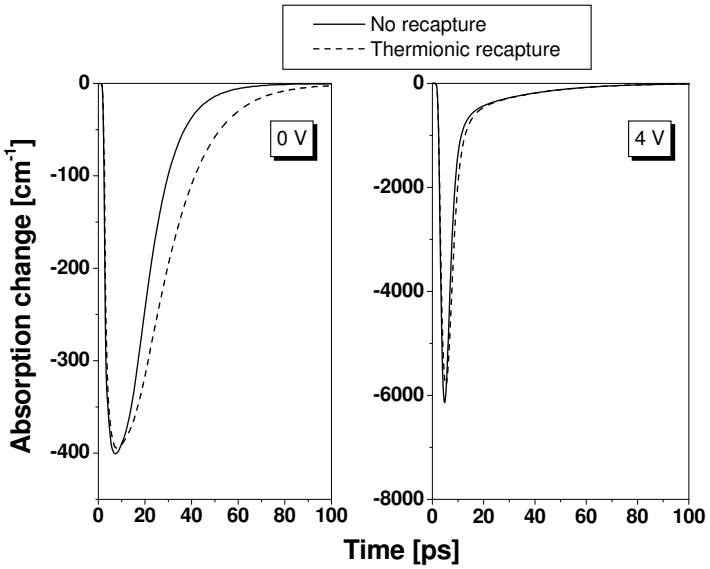

Figure 6.24: Absorption recovery calculated with thermionic recapture and with no recapture, for two different applied biases.

longer than what would be expected from a consideration involving only escape and not capture (this is what we have been referring to as *no recapture* — see page 48). Although most authors disregard recapture, a few papers [169-171] present results which the authors say can only be explained when recapture is taken into account. Hawdon *et al.* mention in passing that recapture must be taken into account to be able to understand their measurements [169]. Moss *et al.* make the simple experiment of comparing the sweep-out rate in two structures which differ only by the number of wells. At low fields, the ratio between the recovery times for the 25-well and the 10-well structures is very close to 2.5, demonstrating unambiguously that recapture really does take place. At higher fields, this ratio goes to about 1, that is, recapture is much less important [170], as the calculations presented above also show. At low excitation power levels, where the escape times are not significantly affected by photo-excited carriers, we also find that the sweep-out time is almost proportional to the number of wells when thermionic recapture is assumed; this is in agreement with the measurements by Moss *et al.* described

above. The behavior is demonstrated in Fig. 6.25, which we will discuss in a moment.

Yoshida *et al.* presented a model which consists of two rate equations: One for the barrier population, and one for the well population. It was stated that there is a "backward flow of carriers" into the wells [171], and a capture term was therefore included in the equations. The simple model by Yoshida *et al.* is completely analogous to the capture and escape part of our model, except Yoshida *et al.* use the escape and capture times as fitting parameters, whereas we calculate them. Without discussing the details, Yoshida *et al.* find a good correspondence between measurements and calculations only when a capture term is included. A capture time of 50 ps is found.[13]

To our knowledge, Yoshida *et al.*'s paper is the first paper on modeling of sweep-out in electroabsorption modulators to take recapture into account. As we have argued many times, work should be put into understanding the conditions under which recapture is important. The paper by Yoshida *et al.* is a step on the way.

For deeper wells, recapture can increase the sweep-out time significantly. Figure 6.25 shows the density of electrons in the electron wells of the structure considered in Sec. 6.4.1. The bias is -0.3 V, the pulse energy is 50 fJ, and we assume thermionic recapture. The recovery with no recapture is shown on the left in Fig. 6.16 (page 124) for an excitation pulse energy of 0.5 pJ. In Fig. 6.25, where the recapture is thermionic, the escape of electrons from "Well 2" is offset compared to "Well 1" because carriers from "Well 1" are captured into "Well 2". For each subsequent well, the same behavior takes place, and the sweep-out time becomes nearly proportional to the number of wells, in line with the results by Moss *et al.* [170] which we referred to above. This behavior is caused by the very fast recapture 'time' that is present when we assume thermionic recapture. Note that there even is an increase in the density of carriers in a number of the wells closest to the n-contact long after the optical excitation has ceased. The same behavior is observed for a number of those hole wells that are closest to the p-contact (not shown). The recovery time under thermionic recapture is about ten times longer than with no recapture, and it is clear that the degree of recapture can influence

[13] This is orders of magnitude higher than that which is calculated from equations (4.27) and (4.26). Such a long capture time essentially corresponds to "no recapture" in our model. However, in Yoshida *et al.*'s model, carriers are captured from the vicinity of the separate-confinement heterobarrier, where the density is much higher than near the wells, which is where carriers are captured in our model.

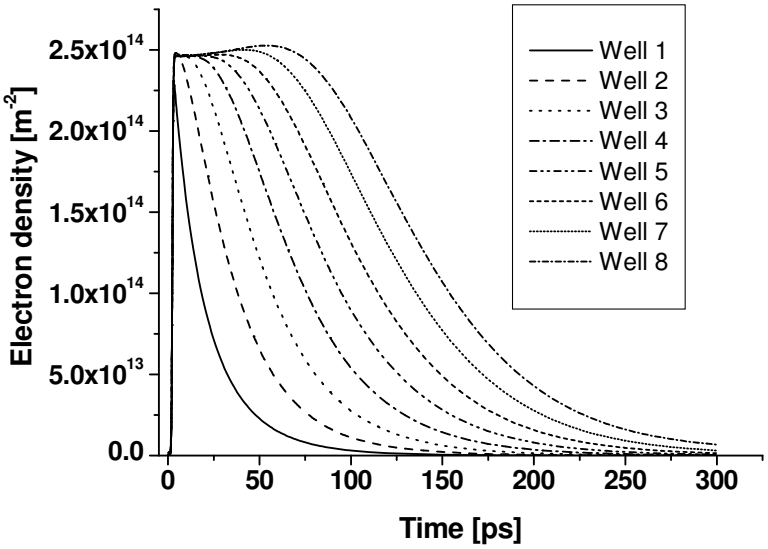

Figure 6.25: The figure shows the electron escape for the eight wells of the structure from Sec. 6.4.1. We have assumed thermionic recapture, and the excitation pulse energy is 50 fJ.

the sweep-out significantly. We refer to Sec. 5.3, where we discussed the importance of recapture both in the steady state and far from equilibrium.

6.7 Summary

In this chapter we have studied carrier sweep-out in electroabsorption modulators by looking at the absorption recovery and the field dynamics after optical excitation. Various structures were considered.

We investigated how the position of the well in a structure with just one well affects the field- and absorption recovery. It was found that the field dynamics at the well is critically dependent on the well's position within the intrinsic region. This was explained using Poisson's equation, and we discussed briefly the influence of the escape times of holes and electrons on the behavior.

When the well is moved within the intrinsic region, the distances to the two contacts change. This is not trivially reflected in the dynamics. The field and absorption changes are complicated functions of the carrier distribution dynamics, and we showed that they are not always good measures of "recovery". We suggested that single-pulse pump-and-probe experiments, which are very important for characterizing the course of the absorption recovery, be supplemented by a measurement technique that can probe the slower components of the sweep-out. Not being able to extract a "recovery time" from the absorption change or from the field change, we looked at the transport of holes from the well to the p-contact. We were able to conclude that drift accounts for nearly all of the change in the sweep-out time that results when the position of the well is changed. Of the three structures we investigated, the structure for which the well was closest to the p-contact had the fastest recovery.

The influence of the intrinsic-region width on the sweep-out process was also investigated. Again, signatures of the differences in the distances to the contacts were clearly seen, and again, we found that drift accounted for nearly all of those differences. The more important effect of changing the width of the intrinsic region is on the amplitude of the induced field change. The wider the intrinsic region is, the larger the induced field-change across the well will be. For all-optical applications, a wider structure may therefore be desirable because it will have a smaller switching energy. However, the increased screening effect must be weighed against the increase in the escape times from the wells and in the transport times to the contacts, both of which lead to an increase in the sweep-out time.

We investigated the influence of the applied bias on the device dynamics. We found that an increase in the applied bias leads to an increase in the absorption change and to a faster recovery. These properties are well known from measurements. We also modeled sweep-out from shallow wells and found very short sweep-out times, in correspondence with measurements on similar structures.

The separate-confinement heterostructure also influences the dynamical properties of electroabsorption modulators. We compared two structures with different separate-confinement heterobarrier structures and found that dividing a large barrier into just two, smaller barriers can drastically reduce the pile-up effects. At very high speeds, where even small charging effects will affect the device performance, introducing more steps should be considered to reduce carrier pile-up further.

Structures with several wells were investigated. First, we demonstrated that the field in the well region in such structures is highly non-uniform. This non-uniformity causes the field-induced changes in the escape times from the wells to be different from well to well. Some wells experience a field increase, some experience a field reduction. The escape times for the different wells will change accordingly, and we showed directly how the field screening affects the escape of carriers from the wells.

Structures with different numbers of wells were modeled. We found that for a fixed product $n \cdot E$ of the number of wells, n, and the excitation pulse energy, E, a structure with more wells will provide a larger absorption change. This means that a structure with more wells generally is desirable. However, increasing the number of wells also results in a slower sweep-out, and the number of wells should therefore be high enough that the desired extinction ratio is realized, but low enough that the recovery time permits operation at the required speed.

Sweep-out at very high excitation pulse energies was investigated. Measurements have shown that the sweep-out is prolonged at high excitation pulse energies, and we were able to explain the physics behind this effect.

Finally, we discussed the influence of recapture on the dynamics. Although recapture has been seen in experiments, the role of recapture on a short time scale is not understood. We showed how the recovery proceeds when the recapture is thermionic, and how it proceeds when there is no recapture, and we found that the effective escape time can be many times longer if the recapture is thermionic. A serious experimental effort is required to shed more light on the importance of recapture.

Chapter 7

Conclusion

This thesis has been concerned with modeling of electroabsorption modulators. Electroabsorption modulators are expected to play an important role both in the coming 40 Gbit/s optical communication systems and in next-generation, all-optical communication systems. Understanding the dynamics in electroabsorption modulators will help to support the development of high-speed components tailored for different functions. For external modulation, for instance, a high saturation power and a high extinction ratio are required, together with a low insertion loss. For all-optical switching, a low insertion loss, a low polarization-dependent loss, and a low saturation power are desirable. The different requirements can obviously not be fulfilled by the same device. Different device designs are required.

Chapter 3 concerned modeling of three all-optical functionalities: Wavelength conversion, demultiplexing, and signal regeneration. To investigate systems-related issues, we used a relatively simple model containing a phenomenological model for the sweep-out dynamics. The sweep-out time is one of the most important parameters in electroabsorption modulators, as it sets the limit for the device operation speed. A simple model in which the sweep-out time is put in "by hand" can of course only describe qualitative dependencies. However, with more qualified input on the sweep-out behavior, this simple model would have a significantly larger predictive power.

Chapter 4 described a detailed model for the carrier sweep-out dynamics in electroabsorption modulators. The model, which we have dubbed PinSim, is a comprehensive drift-diffusion model similar to models that are used to

investigate quantum-well lasers and quantum-well photo-detectors. PinSim can provide qualified, structure-dependent information about the sweep-out characteristics of a device and is thus useful for designing electroabsorption modulator structures. Besides the design aspect, structure-dependent information on the sweep-out behavior could be used to increase the predictive power of the simpler model used in Chapter 3.

In Chapter 5 we used PinSim to investigate the steady-state dynamics in various electroabsorption modulator structures. The work focused on basic characterization of devices. A number of issues were discussed that relate to the design of electroabsorption modulators, such as device absorption spectra, saturation properties, and the effects of field screening induced by carriers that pile up at heterobarriers. The more fundamental issue of carrier recapture was discussed from a theoretical point of view, and from a practical point of view we investigated the saturation properties under various degrees of recapture.

Chapter 6 discussed in detail the sweep-out dynamics for a number of different epitaxial structures. From a fundamental standpoint we discussed the absorption recovery and the field recovery for a number of simple structures. The results enabled us to conclude that the position of the well and the barrier thicknesses influence the carrier sweep-out time mainly through differences in the carrier drift-times to the contacts. We described and analyzed the significant influence that the well position has on the absorption change induced by optical excitation. Typically, electrons escape faster than holes in InGaAsP structures, and putting the wells close to the p-side contact will make for the fastest device. The drawback of having the wells close to the p-side end of the intrinsic region is that the field contribution to the absorption change for certain wells may contribute an absorption *increase* upon excitation. The confinement factor must of course also be kept in mind when the placement of the wells within the intrinsic region is considered.

In connection with these investigations, we showed that the "recovery time" depends on the way in which it is measured. A single-pulse pump-and-probe measurement is a very good way to characterize the absorption recovery. However, a $1/e$-type decay time found from such a measurement may well be an insufficient measure of the recovery time. We gave plenty of examples of how the sweep-out times measured in various apparently acceptable ways can differ significantly. It was argued that the single-pulse pump-and-probe absorption recovery measurement should be combined with a periodic-excitation experiment when devices are characterized. This type

of measurement gives important information about the slower components of the sweep-out, as it allows carrier accumulation effects to be probed.

Other properties were investigated, such as the bias-dependent absorption coefficient and absorption recovery, the absorption recovery in a shallow-well structure, the detailed dynamics in a structure with several wells, and the influence of the heterobarrier design on the dynamical properties.

A detailed study of the dynamics in structures with different numbers of wells was performed. We discussed the influence of the number of wells on the field and band filling contributions to the absorption change. Using a simple approximation of the carrier-induced absorption changes, we were able to include propagation effects and calculate the extinction ratios and insertion losses for the different structures. From those calculations, we drew a number of conclusions about the influence of the number of wells on the all-optical properties of a device. The number of wells also influences the escape times from the different wells, and this issue must also be considered during the design of a device.

Our detailed model was also able to explain the retardation of the recovery under high-energy pulse excitation. A curious effect is responsible for the behavior: After excitation, the carrier distribution itself creates potential wells that impede field-induced carrier removal, i.e. drift. Diffusion is responsible for the initial removal of carriers, and this means that the initial sweep-out is very slow. As the potential wells are reduced through this process, the diffusion component of the transport becomes increasingly important. However, once the potential wells have been eliminated, drift will again become the dominating transport mechanism, carriers will be removed quickly, and the pre-excitation field will be restored.

Finally, the issue of recapture, also discussed in Chapter 5, was investigated using time-resolved calculations. We showed that the importance of recapture is reduced when the field across the wells is increased. The recapture process is not well understood, and we suggested that a focused experimental investigation of it be undertaken.

The present work, presenting both system-level calculations and very detailed sweep-out calculations, is to our knowledge the first comprehensive theoretical study of the carrier sweep-out dynamics in electroabsorption modulators. Separately, the two models we have presented are versatile tools for investigating electroabsorption modulator dynamics. Together, however, they could form a very strong tool for understanding in detail the results of ex-

periments involving electroabsorption modulators.

We believe that electroabsorption modulator models such as PinSim will become increasingly important in the future. Although measurements and actual applications are what matter at the end of the day, an understanding of the behavior of a specific device is, as we have indicated several times in this work, quite difficult to obtain through measurements alone. Calculations using a model such as ours may bring about the understanding of some observed behavior, or may reveal ways in which the epitaxial structure can be modified to improve the device performance.

The shortcomings of the model from Chapter 4 should be eliminated in order to increase the quantitative precision of the model. The absorption calculation, for instance, could be sophisticated, and a calculation of the optical mode could be included into PinSim. Also energy density equations could be introduced into the model so that temperature effects could be taken into account.

There is much more work to be done in this field. The present work has presented a number of simple calculations as well as more complex calculations of the dynamical properties in electroabsorption modulators. More exotic designs could be interesting to investigate with our model. Structures having unequal wells, for instance, might show some desirable property. The propagation aspect is important for modeling of the transmission properties of devices. Although touched upon in Chapter 6, propagation effects have not been investigated much in connection with the calculations that we made using PinSim. Making calculations that include propagation effects would be a very interesting next step. Understanding the experimental results from system-related applications is currently one of the most pressing issues with respect to electroabsorption modulators.

Appendices A–G

Appendix A

Calculation of Fermi levels

The calculation of Fermi levels is crucial for many of the models that are used in the present work. The Fermi level is related to the density of carriers and to the density of available states.

We assume that carriers are in thermal equilibrium. Thermal equilibrium is brought about by carrier-carrier scattering and carrier-phonon scattering. When the external driving-forces vary slowly compared to the carrier-carrier scattering times, some hundreds of femtoseconds, this is a good assumption. However, when this limit is violated, carriers will have a non-thermal energy distribution, and the relations below will not be valid. We use excitation pulses 1-ps long, and the thermal-equilibrium approximation is therefore acceptable.

A.0.1 Fermi levels for bulk

The Fermi level $E_{\mathrm{fe,3D}}$ for the conduction band is defined through

$$n = \int_{E_{\mathrm{c}}}^{\infty} \frac{\rho_c}{1 + \exp(\frac{E - E_{\mathrm{fe,3D}}}{k_{\mathrm{B}} T})} \, \mathrm{d}E \tag{A.1}$$

and the Fermi level $E_{\mathrm{fh,3D}}$ for the valence band is defined through

$$p = \int_{E_{\mathrm{hh}}}^{\infty} \frac{\rho_{\mathrm{hh}}}{1 + \exp(\frac{E - E_{\mathrm{fh,3D}}}{k_{\mathrm{B}} T})} \, \mathrm{d}E + \int_{E_{\mathrm{lh}}}^{\infty} \frac{\rho_{\mathrm{lh}}}{1 + \exp(\frac{E - E_{\mathrm{fh,3D}}}{k_{\mathrm{B}} T})} \, \mathrm{d}E \tag{A.2}$$

where ρ_c, ρ_{hh}, and ρ_{lh} are the densities of states in the conduction band, the heavy hole band, and the light hole band, respectively. E_c, E_{hh}, and E_{lh} are the band edge energies for the same bands. As indicated in Eq. (A.2), we assume that light and heavy holes have a common Fermi level.

There is no explicit expression for the Fermi level as function of the carrier density. However, several good approximations exist that relate explicitly the Fermi level to the carrier density. One such expression is the 2/1-Padé approximation [172] given by

$$\beta\mu \approx \ln\xi + K_1 \ln(K_2\xi + 1) + K_3\xi, \quad -\infty < \beta\mu \leq 30 \tag{A.3}$$

where μ is the Fermi level, $\beta = 1/k_B T$, and

$$\xi = \frac{\nu}{\nu_0} = \frac{2}{\sqrt{\pi}} \int_0^\infty \mathrm{d}x \sqrt{x} \frac{z e^{-x}}{1 + z e^{-x}} \tag{A.4}$$

$$\nu_0 = \frac{1}{4} \left(\frac{2 m_\nu^* k_B T}{\pi \hbar^2} \right)^{3/2} \tag{A.5}$$

where $z = \exp(\beta\mu)$. The constants are $K_1 = 4.8966851$, $K_2 = 0.04496457$, and $K_3 = 0.1333760$, and the masses can be found in Sec. A.0.3. The error introduced by using (A.3) is within a couple of percent in the indicated range. Other approximations exist, see e.g. [173]. The *Boltzmann approximation* is obtained when only the term $\ln\xi$ is retained.

In case there is strain in a layer, the valence bands are no longer degenerate. In the Boltzmann approximation, we can immediately rewrite Eq. (A.2) as

$$p = p_{str}^0 \exp\left(\frac{E_{fh,3D}}{k_B T} \right) \tag{A.6}$$

where

$$p_{str}^0 = \frac{1}{4} \left(\frac{2 m_{str}^* k_B T}{\pi \hbar^2} \right)^{3/2} \tag{A.7}$$

with

$$m_{str}^{*\,3/2} = \left[m_{hh}^* \exp\left(-\frac{E_{hh}}{k_B T} \right) \right]^{3/2} + \left[m_{lh}^* \exp\left(-\frac{E_{lh}}{k_B T} \right) \right]^{3/2} \tag{A.8}$$

A.0.2 Fermi level in wells

For carriers in a quantum well, the density of carriers ν_{2D} is related to the Fermi level $E_{f\nu,2D}$ through

$$\nu_{2D} = \sum_i \nu_{2D}^{(i)} = \sum_i \int_{-\infty}^{\infty} \frac{\rho_{\nu,2D}^{(i)}(E)}{1+\exp(\frac{E-E_{f\nu,2D}}{k_B T})} dE, \qquad (\nu = n, p) \tag{A.9}$$

where $\nu_{2D}^{(i)}$ is the density of carriers in the i-th sub-band and $\rho_{\nu,2D}^{(i)}$ is the density of states for the same sub-band. We assume that the sub-band dispersion is parabolic. This leads to a constant density of states in the in-plane direction for each bound state:

$$\rho_\nu^{(i)}(E) = \frac{m_{\nu,\|}^{(i)}}{\pi\hbar^2}\Theta(E - E_i) \tag{A.10}$$

where $m_\|^{(i)}$ is the in-plane mass and Θ is the Heaviside function (defined in footnote 6 on page 61). E_i is the energy of the i-th bound state.

Using Eq. (A.10), the relation between the carrier density and the Fermi level can be written

$$\begin{aligned}
\nu_{2D} &= \sum_{\substack{\text{quantized} \\ \text{states, } i}} \nu_{2D}^{(i)} \\
&= \sum_i \left(\int_{E_i}^{\infty} \frac{m_{\nu,\|}^{(i)}}{\pi\hbar^2} \frac{1}{1+\exp(\frac{E-E_{f\nu,2D}}{k_B T})} dE \right) \\
&= \sum_i \frac{m_{\nu,\|}^{(i)}}{\pi\hbar^2} f_{2D}\left(\frac{E_{f\nu,2D} - E_i}{k_B T}\right)
\end{aligned} \tag{A.11}$$

where

$$f_{2D}(\frac{E}{k_B T}) = \int_0^{\infty} \frac{1}{1+\exp(\frac{E'-E}{k_B T})} dE' = k_B T \ln[1+\exp(\frac{E}{k_B T})] \tag{A.12}$$

and $m_{\nu,\|}^{(i)}$ is the in-plane mass level i. For the valence band, both heavy and light hole states exist. These states typically have different energies because the heavy-hole and light-hole masses in the growth direction are different.

Also the in-plane masses are very different, the light-hole mass typically being significantly heavier than the heavy-hole mass.

Using Eq. (A.11), we can solve for the Fermi level in the well. In case the carrier density is non-degenerate, that is, $k_{\mathrm{B}}T \gg E_{\mathrm{f}\nu,2\mathrm{D}} - E_1$, where E_1 is the lowest bound state for the appropriate band, we can approximate

$$\begin{aligned} f_{2\mathrm{D}}(\frac{E_{\mathrm{f}\nu,2\mathrm{D}} - E_1}{k_{\mathrm{B}}T}) &= k_{\mathrm{B}}T \ln[1 + \exp(\frac{E_{\mathrm{f}\nu,2\mathrm{D}} - E_1}{k_{\mathrm{B}}T})] \\ &\approx k_{\mathrm{B}}T \exp(\frac{E_{\mathrm{f}\nu,2\mathrm{D}} - E_1}{k_{\mathrm{B}}T}) \end{aligned} \tag{A.13}$$

and we find this approximation for Eq. (A.11):

$$\nu_{2\mathrm{D}} = \frac{m^{(i)}_{\nu,\|}}{\pi\hbar^2} k_{\mathrm{B}}T \exp(\frac{E_{\mathrm{f}\nu,2\mathrm{D}} - E_1}{k_{\mathrm{B}}T}) \tag{A.14}$$

We use the general equation Eq. (A.11), except in Eq. (4.24) where we use Eq. (A.14). As for bulk, we will assume that heavy holes and light holes have a common Fermi level.

Modification to density of states near quantum wells?

Some authors modify the 3D density of states near a quantum well [174] to take into account that the band edge at the position of well is lower than that at the barrier. Instead of using a $\sqrt{E + \Delta E}$ dependence, where E is taken to be zero at the bottom of the well and ΔE is the depth of the well, these authors use a $\sqrt{E} - \sqrt{\Delta E}$ dependence. The difference between the two expressions can be substantial, as one can easily verify by calculating for a "typical" quantum well the relation between the carrier density and the Fermi level using the two expressions.

We have chosen not use the $\sqrt{E} - \sqrt{\Delta E}$ form. To count the density of states is this way requires physically that the density of states *in the well* be 3D-like. However, typically there is one, two, maybe three states in the well. Furthermore, the wells we look at are rather thin and thus have little influence on the density of bulk states. We therefore use the $\sqrt{E + \Delta E}$ dependence for the bulk states, and take the presence of bound states in the well to be the only source of change in the density of states near the well.

A.0.3 Carrier masses

The carrier masses are very important for the properties of a device. A lot of confusion exists about which masses are appropriate in different contexts. To avoid this confusion in the present work, we have made sure to emphasize for each formula exactly which mass we believe is appropriate. The masses below are taken from [142].

Electrons

The effective mass for electrons is given by

$$\frac{m_{\mathrm{e}}^*}{m_0} = 0.08 - 0.116x + 0.026y - 0.059xy + (0.064 - 0.02x)y^2 + (0.06 + 0.032y)x^2 \quad \text{(A.15)}$$

We take this mass to be isotropic, that is, equal in the growth direction and in the in-plane directions.

Holes

The effective masses for heavy holes and light holes are, respectively:

$$\frac{m_{\mathrm{hh}}^*}{m_0} = 0.5xy + 0.4(1-x)y + 0.6(1-x)(1-y) + 0.67x(1-y) \quad \text{(A.16)}$$

$$\frac{m_{\mathrm{lh}}^*}{m_0} = 0.87xy + 0.026(1-x)y + 0.12(1-x)(1-y) + 0.17x(1-y) \quad \text{(A.17)}$$

The heavy hole masses along the growth direction and parallel to the quantum-well layers are given by

$$\frac{m_{\mathrm{hh},\perp}}{m_0} = \frac{1}{\gamma_1 - 2\gamma_2} \qquad \frac{m_{\mathrm{hh},\parallel}}{m_0} = \frac{1}{\gamma_1 + \gamma_2} \quad \text{(A.18)}$$

and the light holes masses are

$$\frac{m_{\mathrm{lh},\perp}}{m_0} = \frac{1}{\gamma_1 + 2f_+\gamma_2} \qquad \frac{m_{\mathrm{lh},\parallel}}{m_0} = \frac{1}{\gamma_1 - f_+\gamma_2} \quad \text{(A.19)}$$

The parameters γ_1 and γ_2 are the Luttinger parameters, which are functions of x and y:

$$\gamma_1 = 6.85xy + 20.4(1-x)y + 4.95(1-x)(1-y) + 4.05x(1-y) \quad \text{(A.20)}$$

$$\gamma_2 = 1.9xy + 8.3(1-x)y + 1.65(1-x)(1-y) + 0.49x(1-y) \quad \text{(A.21)}$$

The parameter f_+ depends on the strain in the structure. Details may be found for instance in [142].

Appendix B

The field-dependent mobilities in InGaAsP

B.1 Mobilities

The motion of carriers in a high field can be well described through the use of a field-dependent mobility. Experimental data may be found in e.g. [108]. We use the parameterization from [175] for the electron and holes mobilities μ_{n} and μ_{p}:

$$\mu_{\mathrm{n}}(E) = \frac{\mu_{\mathrm{n}}^0 + v_{\mathrm{nhf}}\beta|E|}{1+\beta E^2} \tag{B.1}$$

$$\mu_{\mathrm{p}}(E) = \frac{\mu_{\mathrm{p}}^0 v_{\mathrm{phf}}}{v_{\mathrm{phf}} + \mu_{\mathrm{p}}^0 E} \tag{B.2}$$

with $v_{\mathrm{nhf}} = 5.4 \cdot 10^6$ cm/s, $v_{\mathrm{phf}} = 5.2 \cdot 10^6$ cm/s, $\beta = 0.8 \cdot 10^{-7}$ m^2/V^2, and $\gamma = 1$. E is the electric field, and μ_{n}^0 and μ_{p}^0 are the low-field mobilities. For those, we use [119]:

$$\mu_{\mathrm{n}}^0 = (0.45 + 0.65y)\left(\frac{300\ \mathrm{K}}{T}\right)^{1.25}\ \mathrm{m}^2/\mathrm{V}^2 \tag{B.3}$$

$$\mu_{\mathrm{p}}^0 = 0.036\left(\frac{300\ \mathrm{K}}{T}\right)^{2.2}\ \mathrm{m}^2/\mathrm{V}^2 \tag{B.4}$$

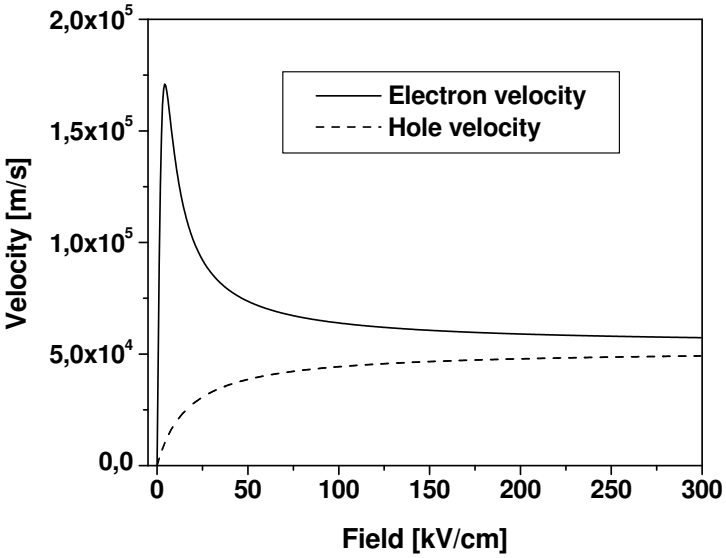

Figure B.1: Drift velocities for electrons and holes as function of field for InP.

Although the equations above are determined from measurements on lattice-matched $In_{1-x}Ga_xAs_yP_{1-y}$ material, we allow ourselves to also use these formulas away from the lattice-matched $(y, x(y))$ graph (see Eq. (4.6)). Figure B.1 shows the field-dependent velocities, $\mu_\nu(E)E$, for holes and electrons.

Appendix C

Model verifications

Here, we describe some of the fundamental tests that have been performed to ensure that the equations are implemented correctly in the simulator, and that the numerical engine works correctly.

C.1 The p-n junction

The most fundamental problem that PinSim can solve is that of finding the electrostatic potential in a p-n diode. When two materials with opposite doping types are brought into contact, the mobile carriers redistribute until a situation is established where the net current is zero. If a bias is applied to the diode, a non-zero current will be sustained in the structure. The analytical solution to the problem is easy to write down in the Boltzmann approximation when diffusion is disregarded [109]:

$$\phi(x) = \begin{cases} \phi(-\infty) & x > -d_p \\ \phi(-\infty) + \frac{eN_A}{2\epsilon}(x - d_p)^2 & -d_p < x < 0 \\ \phi(\infty) - \frac{eN_D}{2\epsilon}(x - d_n)^2 & 0 < x < d_n \\ \phi(\infty) & x > d_n \end{cases} \tag{C.1}$$

(note that x in Eq. (C.1) is referenced from the junction). Figures C.1 and C.2 show the electrostatic energy across a p-n junction with InP on both sides, but with p-type doping on one side and n-type doping on the other side. The

density of p-dopants, N_A, is $1.0 \cdot 10^{24}$ m^{-3}, and the density of n-dopants, N_D, is $1.5 \cdot 10^{24}$ m^{-3}. The susceptibility $\epsilon = 3.6^2 \epsilon_0$.

Figure C.1 shows the electrostatic energy when the applied voltage is 1 V (i.e., forward bias). The analytical expression does not include the diffusion term and hence we show the calculation with PinSim both with and without the inclusion of the diffusion term. The result of the calculation that excludes the diffusion term is in almost perfect correspondence with the analytical result. The inclusion of diffusion tends to smear out the carriers, and hence the potential change occurs over a somewhat larger region.

We also expect the diffusion to have a smaller influence when the field is increased, which is indeed seen in Fig. C.2 where the bias is 0 V. More detailed calculations reveal that the influence of the diffusion is correctly calculated. This is discussed below.

C.2 Diffusion versus drift

In the comparisons above, the analytical results are only valid when the diffusion contribution to the current is much smaller than the drift contribution.

In reality, diffusion is present and tends to smear out the carrier distribution, as shown in Fig. C.1 and C.2. In the following, we test that the diffusion term is correctly incorporated.

The slope of the carrier density is determined by the balance between the drift and the diffusion terms. Under reverse bias, there is only a small current, and we can assume $J_\nu = 0$ ($\nu = \mathrm{n}, \mathrm{p}$). Then, an analytic expression for n and p as functions of position may be found. The current density equations are

$$(\text{eqs. (4.1)} - \text{(4.2)}): \qquad J_\nu = e\mu_\nu \nu E \pm eD_\nu \frac{\mathrm{d}\nu}{\mathrm{d}x}, \quad \nu = n, p \tag{C.2}$$

Using the assumption $J_\nu = 0$, we find

$$\mu_\nu \nu E = \mp D_\nu \frac{\mathrm{d}\nu}{\mathrm{d}x} \tag{C.3}$$

Using

$$(\text{Eq. (4.4)}): \qquad D_\nu = \mu_\nu \frac{kT}{e} \tag{C.4}$$

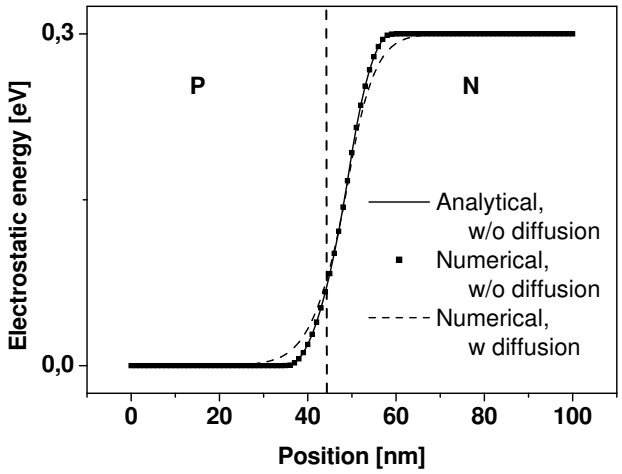

Figure C.1: Numerically calculated electrostatic energy in the vicinity of a p-n junction, with and without diffusion. The applied bias, V_{app}, is 1 V (i.e. forward bias). The analytical expression Eq. (C.1) for the electrostatic energy, found in the absence of diffusion, is also shown.

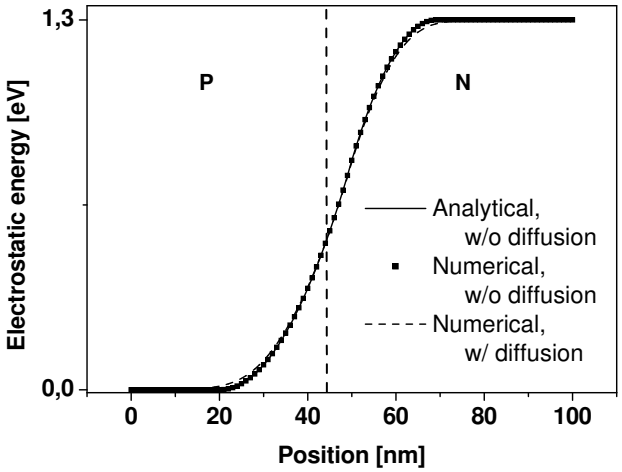

Figure C.2: Same as Fig. C.1, but $V_{\mathrm{app}} = 0$ V. Note that the diffusion term is less important when the reverse bias is increased. The influence of diffusion is smaller than in Fig. C.1 due to the increased field in the intrinsic region.

we are able to find

$$\frac{eE}{kT} = \mp \frac{1}{\nu} \frac{\mathrm{d}\nu}{\mathrm{d}x} \tag{C.5}$$

Assuming that the field is sloped (due to a background doping profile), and writing the linear field in the intrinsic region as

$$E(x) = E'(x - x_0) + E(x_0) \tag{C.6}$$

Eq. (C.5) can be integrated to

$$\nu(x) = \nu(x_0) \exp\Big(\mp \frac{eE'(x - x_0)^2 - 2eE(x_0)(x - x_0)}{2kT} \Big) \tag{C.7}$$

This is compared in Fig. C.3 with the numerical results from PinSim. The figure shows the hole and electron carrier densities across the structure. Note that this structure is a p-i-n structure.

The correspondence is excellent. The remaining differences are due to the approximation in Eq. (C.6) that the field is exactly linear, and due to small, insignificant numerical errors. The curving of the carrier densities in the log-plot is due to $E' \neq 0$. Note that the curves for the carrier densities span many orders of magnitude. The correspondence is very sensitive to the parameters involved, which means that the fit by no means is coincidental. It was also checked that changes to Eq. (C.2) were reflected correctly in the numerical results, which turned out to be the case.

The comparison is only made in the intrinsic region, where the carrier densities vary significantly, and where the electric field is high. There we get by far the most clear demonstration.

C.3 J-V characterization

On a simple level, we have tested the basic bulk drift-diffusion equations by looking at the current density as function of electric field in a single-layer material doped with either donors or acceptors. The simple relation

$$J_\nu = e\nu\mu_\nu E \tag{C.8}$$

should be recovered, which indeed it is.

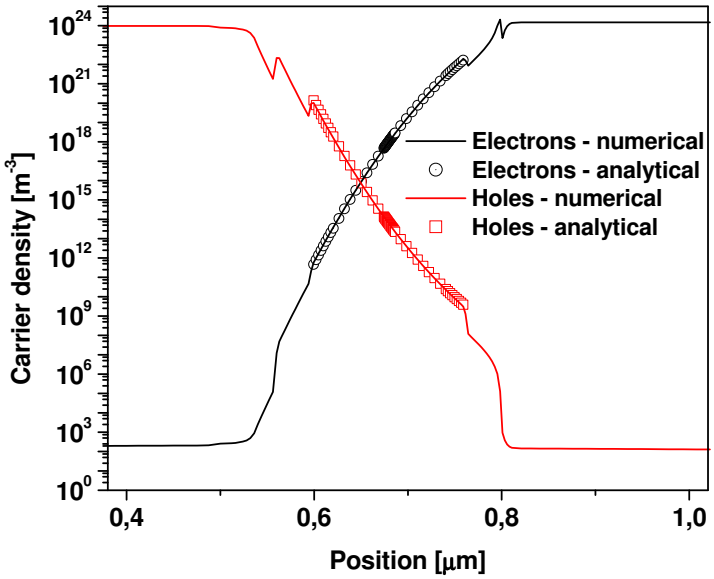

Figure C.3: Comparison between analytically and numerically calculated electron and hole carrier densities in a p-i-n structure.

C.4 Other verifications

Besides the verifications shown above, all the other equations have of course also been verified. We will not show these tests here, but we mention that they include verification of the continuity equations for bulk carriers (eqs. (4.16)–(4.17)) and well carriers (eqs. (4.19)–(4.20)), the current density across the heterobarriers (Eq. (4.32) and (4.34)), the expression for the electron escape current out of the wells (Eq. (4.24)) as well as that for holes, and the Schrödinger equation, Eq. (4.39). Finally, we have made sure that the coupling between the Schrödinger equation and the continuity equations is accounted for properly.

Appendix D

The discretized equations

In the following, we write down the discretized forms of the equations used in the simulator.

D.1 Spatial derivatives

The Poisson equation

The Poisson equation (4.5) is discretized as:

$$\frac{D_{i+\frac{1}{2}} - D_{i-\frac{1}{2}}}{(h_i + h_{i-1})/2} - \rho_i = 0 \tag{D.1}$$

where we have defined

$$D_{i+\frac{1}{2}} = -\epsilon \frac{\phi_{i+1} - \phi_i}{h_i} \tag{D.2}$$

and approximated

$$\left.\frac{\mathrm{d}D}{\mathrm{d}x}\right|_{x_i} \approx \frac{D_{i+\frac{1}{2}} - D_{i-\frac{1}{2}}}{(h_i + h_{i-1})/2} \qquad (\text{note that } D = \epsilon E = -\epsilon \frac{\mathrm{d}\phi}{\mathrm{d}x}) \tag{D.3}$$

The drift-diffusion and continuity equations

For the drift-diffusion equations we use the so-called Sharfetter-Gummel approximation [106]. In the derivation of the discretized drift-diffusion equa-

tions, we assume that J_ν is varying slowly enough that

$$J_\nu(x) \approx J_\nu(\frac{x_{i+1}+x_i}{2}), \quad x \in [x_i, x_{i+1}] \tag{D.4}$$

is a good approximation. Here, we write down the electron current density equation. The electron and hole current density equations are almost identical, differing only by a single sign. The expression for one type of carrier can therefore easily be found from the expression for the other. We do this after we have derived the discretized electron current density equation.

We start from Equation (4.1), which can be written in one dimension as

$$\frac{\mathrm{d}n}{\mathrm{d}x} + an = b \tag{D.5}$$

Note that we have left out the contribution from the escape and capture current from Eq. (4.16) and (4.17). These terms are trivially added.

Assuming that a and b can be considered constant for $x \in [x_i, x_{i+1}]$, we find

$$n(x) = e^{-a(x-x_0)} \left[\int_{x_0}^{x} b e^{a(x'-x_0)} dx' + c \right] \tag{D.6}$$

$$= e^{-a(x-x_0)} \left[\frac{b}{a}(e^{a(x-x_0)} - 1) + c \right] \tag{D.7}$$

Putting $x_0 = x_i$ and finding c, and then evaluating the expression at $x = x_{i+1}$ and rearranging, we find

$$\frac{b}{a} = \frac{n_{i+1}}{1 - e^{-ah_i}} - \frac{n_i e^{-ah_i}}{1 - e^{-ah_i}} \tag{D.8}$$

where

$$h_i \doteq x_{i+1} - x_i \tag{D.9}$$

and

$$n_i \doteq n(x_i) \tag{D.10}$$

Finally, we write the generic solution as

$$bh_i = B(-ah_i)n_{i+1} - B(ah_i)n_i \tag{D.11}$$

where

$$B(x) \doteq \frac{x}{e^x - 1} \tag{D.12}$$

is the *Bernoulli function.*

For the electron current equation, we have

$$a = \frac{\mu_n}{D_n}\frac{\mathrm{d}\phi_c}{\mathrm{d}x} \approx \frac{\mu_n}{D_n}\frac{\phi_{c,i+1} - \phi_{c,i}}{h_i} \tag{D.13}$$

$$b = \frac{J_n}{eD_n} \tag{D.14}$$

where

$$\phi_c = -\phi \tag{D.15}$$

so that, keeping in mind the approximation (D.4):

$$J_{n,i+\frac{1}{2}} \approx eD_n b \tag{D.16}$$

$$= \frac{eD_n}{h_i}\left(B(-\frac{\mu_n}{D_n}\Delta\phi_{c,i+\frac{1}{2}})n_{i+1} - B(\frac{\mu_n}{D_n}\Delta\phi_{c,i+\frac{1}{2}})n_i\right) \tag{D.17}$$

with

$$\Delta\phi_{c,i+\frac{1}{2}} = \phi_{c,i+1} - \phi_{c,i} \tag{D.18}$$

Finally, we have

$$-\frac{\partial n}{\partial t} + \frac{1}{e}\left(\frac{J_{n,i+\frac{1}{2}} - J_{n,i-\frac{1}{2}}}{(h_i + h_{i-1})/2}\right) - R(n_i, p_i) = 0 \tag{D.19}$$

If the bulk point is next to a heterobarrier, then either the term $J_{n,i-\frac{1}{2}}$ or the term $J_{n,i+\frac{1}{2}}$ in Eq. (D.19) will be replaced by the expression for the current density across the heterobarrier. If the heterobarrier is on the right of the bulk point, the term $J_{n,i+\frac{1}{2}}$ is replaced. If the heterobarrier is on the left, the term $J_{n,i-\frac{1}{2}}$ is replaced. For the heterobarrier, we have an electron and a hole carrier density on either side of the barrier. Thus, the heterobarrier is characterized by five variables: The electron and hole carrier densities on either side of the barrier, and the potential.

Finding the equation for $J_{p,i+\frac{1}{2}}$ is now straightforward as the basic continuity equation is almost identical to that for electrons, expect for the sign of the diffusion term, which translates into opposite signs for both a and b. Hence, the discretization results in

$$J_{p,i+\frac{1}{2}} \approx -eD_p b \tag{D.20}$$

$$= -\frac{eD_p}{h_i}\left(B(\frac{\mu_p}{D_p}\Delta\phi_{v,i+\frac{1}{2}})p_{i+1} - B(-\frac{\mu_p}{D_p}\Delta\phi_{v,i+\frac{1}{2}})p_i\right) \tag{D.21}$$

with

$$\Delta\phi_{v,i+\frac{1}{2}} = \phi_{v,i+1} - \phi_{v,i} \tag{D.22}$$

Taking into account

$$\frac{\partial J_p}{\partial x} + e\frac{\partial p}{\partial t} = -eR \tag{D.23}$$

the equation for the hole current becomes

$$\frac{\partial p}{\partial t} + \frac{1}{e}\left(\frac{J_{p,i+\frac{1}{2}} - J_{p,i-\frac{1}{2}}}{(h_i + h_{i-1})/2}\right) + R(n_i, p_i) = 0 \tag{D.24}$$

The quantum-well continuity equations Eq. (4.19) and (4.20) are trivially discretized as they contain no spatial derivatives.

The time derivatives above are discretized as discussed in Sec. D.2.

The Schrödinger equation

The Schrödinger equation is:

$$\left[-\frac{\hbar^2}{2}\frac{\mathrm{d}}{\mathrm{d}z}\left(\frac{1}{m_{\nu,\perp}}\frac{\mathrm{d}}{\mathrm{d}z}\right) + V(z)\right]\psi_n(z) = \varepsilon_n\psi_n(z) \tag{D.25}$$

where $m_{\nu,\perp}$ is the mass in the growth direction for the carrier type in question ($\nu = \mathrm{c}, \mathrm{hh}, \mathrm{lh}$). The masses may be found in Sec. A.0.3.

First, we make the following approximation:

$$\frac{1}{m_{\nu,\perp}}\frac{\mathrm{d}\psi}{\mathrm{d}z}\Big|_{x_{i+\frac{1}{2}}} \approx \frac{\psi_{i+1} - \psi_i}{m_{\nu,\perp}^{i+\frac{1}{2}} h_i} \tag{D.26}$$

where

$$m_{\nu,\perp}^{i+\frac{1}{2}} = \frac{m_{\nu,\perp}^{i+1} + m_{\nu,\perp}^{i}}{2} \tag{D.27}$$

and

$$h_i = x_{i+1} - x_i \tag{D.28}$$

Using the generic approximation

$$\frac{\mathrm{d}f}{\mathrm{d}x}(x_i) \approx 2\frac{f_{i+\frac{1}{2}} - f_{i-\frac{1}{2}}}{h_i + h_{i-1}} \tag{D.29}$$

we can find the discretized Schrödinger equation:

$$-\frac{\hbar^2}{2}\frac{2}{h_i + h_{i-1}}\left[\frac{\psi_{i+1} - \psi_i}{m_{\nu,\perp}^{i+\frac{1}{2}} h_i} - \frac{\psi_i - \psi_{i-1}}{m_{\nu,\perp}^{i-\frac{1}{2}} h_{i-1}}\right] + V_i\psi_i = E\psi_i \tag{D.30}$$

where

$$V_i = V(x_i) \tag{D.31}$$

is the potential at $x = x_i$.

D.2 Time derivatives

Because of its stability properties [106], we make use of the backward Euler method. Thus, the generic equation

$$\frac{\mathrm{d}f}{\mathrm{d}t} = g(t) \tag{D.32}$$

is discretized as

$$\frac{f(t_{k+1}) - f(t_k)}{d_k} = g(t_{k+1}) \tag{D.33}$$

The time corresponding to time step number k is t_k, and d_k is the time difference between step k and $k+1$:

$$d_k = t_{k+1} - t_k \tag{D.34}$$

Using the equations above, Eq. (D.19) becomes

$$-\frac{n^{(k+1)}-n^{(k)}}{d_k}+\frac{1}{e}\left(\frac{J^{(k+1)}_{n,i+\frac{1}{2}}-J^{(k+1)}_{n,i-\frac{1}{2}}}{(h_i+h_{i-1})/2}\right)-R(n_i^{(k+1)},p_i^{(k+1)})=0 \qquad \text{(D.35)}$$

where we have explicitly shown the times at which variables are evaluated (t_k and t_{k+1}).

The time derivatives in the other continuity equations are discretized the same way.

Numerical errors in time-dependent simulations

Time derivatives are approximated using a linear expansion as shown above. From the differential equation

$$\frac{\mathrm{d}x}{\mathrm{d}t}=f(x;t) \qquad \text{(D.36)}$$

the change in x is found as

$$\Delta x=f(x;t)\cdot\Delta t \qquad \text{(D.37)}$$

where Δt is the time step. (Despite what we described in Sec. D.2, in the present section we evaluate f in t instead of in $t+\Delta t$ — this is not important for the argument.)

As an example, the equation for the density for electrons in a well can be simplified as

$$\frac{\mathrm{d}n}{\mathrm{d}t}=-\frac{n}{\tau} \qquad \text{(D.38)}$$

which has the solution

$$n(t)=n_0\cdot\exp\left(-\frac{t}{\tau}\right) \qquad \text{(D.39)}$$

The parameter τ is some characteristic time (e.g., the escape time for electrons in wells). The approximated change for n at $t=0$ is

$$\Delta n(t)|_{\text{approx}}=\frac{n_0}{\tau}\cdot\Delta t \qquad \text{(D.40)}$$

whereas the real change in n is

$$\Delta n(t)|_{\text{real}} = n_0 \left(1 - \exp\left(-\frac{t}{\tau}\right)\right) \tag{D.41}$$

The error is given by

$$\frac{\Delta n|_{\text{approx}}}{\Delta n(t)|_{\text{real}}} = \frac{\Delta t/\tau}{1 - \exp(-\Delta t/\tau)} \tag{D.42}$$

For $\Delta t/\tau = 1$, the error is 60 %, for $\Delta t/\tau = 1/2$, the error is 27 %, and only when $\Delta t/\tau = 1/10$ is the error below 5 %.

A much better approximation for the change in n is

$$\Delta n(t)|_{\text{approx}} = \frac{2n_0}{2\tau + \Delta t} \cdot \Delta t \tag{D.43}$$

This approximations should be introduced into PinSim. We have not done this yet.

D.3 Scaling of the equations

The problem at hand involves many equations, often more than a thousand. Furthermore, there is a number of different types of equations in the problem: The Poisson equation, and the 2D and 3D continuity equations. The variables in the problem are the densities of electrons and holes in the discretization points, and the electrostatic potential in the those same points. The discretization of the equations is described above. Numerically, a "solution" is a set of these variables that results in the left-hand sides of Eq. (D.1), (D.19), and (D.24) together with the quantum well equations (which are similar to (D.19) and (D.24)) evaluating to values below some appropriately small number ε. However, the Poisson equation has unit C/m^3 whereas the bulk continuity equations have unit $\text{m}^{-3}\text{s}^{-1}$. The 2D continuity equations have unit $\text{m}^{-2}\text{s}^{-1}$. This means that numerically they evaluate to very different orders of magnitude, and we can not be sure that a given ε is appropriate to "solve" all the equations. Therefore, we scale the equations to unity order. (The Schrödinger equation needs not be scaled, as it is solved outside of the core engine, as described in Sec. 4.11.) Scaling the equations also reduces the numerical errors that result when we invert the Jacobian.

Defining

$$x_0 \doteq L(\text{1D case}) \tag{D.44}$$
$$\phi_0 \doteq \frac{kT}{e} \tag{D.45}$$
$$C_0 \doteq \max |C(x)| \, , x \in [0, L] \tag{D.46}$$
$$D_0 \doteq \max |D_n(x), D_p(x)| \, , x \in [0, L] \tag{D.47}$$
$$R_0 \doteq \frac{D_0 C_0}{x_0^2} \tag{D.48}$$
$$t_0 \doteq \frac{x_0^2}{D_0} \tag{D.49}$$

we scale the position variable x, the time variable t, and the core variables in this way:

$$\tilde{x} = \frac{x}{x_0} \tag{D.50}$$
$$\tilde{t} = \frac{t}{t_0} \tag{D.51}$$
$$\tilde{\phi} = \frac{\phi}{\phi_0} \tag{D.52}$$
$$\tilde{\nu} = \frac{\nu}{C_0}, \quad \tilde{\nu}_{\text{2D}} = \frac{\nu}{C_0 \cdot x_0} \qquad (\nu = n, p) \tag{D.53}$$

and we scale the parameters like this:

$$\tilde{D_\nu} = \frac{D_\nu}{D_0} \quad (\nu = n, p) \tag{D.54}$$
$$\tilde{\mu_\nu} = \frac{\mu_\nu}{\frac{D_0}{\psi_0}} \quad (\nu = n, p) \tag{D.55}$$
$$\tilde{R} = \frac{R}{R_0} \tag{D.56}$$

where R is the recombination rate.

This variable scaling results in the following scaled equations:

$$0 = \lambda^2 \nabla \cdot \nabla \tilde{\phi} - (\tilde{n} - \tilde{p} - \tilde{C}) \tag{D.57}$$

$$\tilde{J}_n = \tilde{\mu}_n \tilde{n} \nabla \tilde{\phi}_c + \tilde{D}_n \nabla \tilde{n} \tag{D.58}$$

$$\tilde{J}_p = \tilde{\mu}_p \tilde{p} \nabla \tilde{\phi}_v - \tilde{D}_p \nabla \tilde{p} \tag{D.59}$$

$$\frac{\partial \tilde{n}}{\partial \tilde{t}} = \nabla \cdot \tilde{J}_n - \tilde{R}(\tilde{\phi}, \tilde{n}, \tilde{p}) \tag{D.60}$$

$$-\frac{\partial \tilde{p}}{\partial \tilde{t}} = \nabla \cdot \tilde{J}_p + \tilde{R}(\tilde{\phi}, \tilde{n}, \tilde{p}) \tag{D.61}$$

The continuity equations for the wells are very similar to Eq. (D.60) and (D.61).

Appendix E

Explanation of the structure file

Defining an epitaxial structure with its doping levels, the x and y parameters of $In_{1-x}Ga_xAs_yP_{1-y}$, the discretization of the structure, and the point types (bulk, heterobarrier, or quantum well), is very difficult to do by hand. It takes a long time even for relatively simple structures, and, especially for complicated structures, it is extremely error-prone.

An interpreter was programmed into PinSim that can read the epitaxial structure, the doping levels, and the discretization from a simple text file. The interface allows the user to easily insert or remove sections of the epitaxial structure. It is also possible to put comments into the structure file.

E.1 Commands

The # command

The character **#** in the beginning of a line causes PinSim to ignore the line entirely. The comment command is useful for either commenting out structure lines, or for adding descriptive comments. Examples of uses of **#** are shown in our sample structure file in Fig. E.1.

The `start` command

Anything that precedes the `start` commands in the structure file is ignored. The command `start` must be present in the file.

The bulk layer

A bulk layer is indicated with the keyword `bulk` in the beginning of the line. This instructs PinSim to use simple drift-diffusion equations for the transport in this region.

If one of variables `x` and `y` is equal to or greater than 3, the layer will be lattice-matched, and the value of the other variable will be used to determine the material composition. As an example, `x=3` and `y=0` will give an InP-layer. At least one of `x` and `y` must be between `0` and `1`.

Example:

```
bulk x=0.0 y=0.0 n=50 na=1.0e21 nd=1.e22 l=200e-9
```

will provide an InP bulk layer 200 nm long, p-doped to $1.0 \cdot 10^{21}$ m^{-3} and n-doped to $1.0 \cdot 10^{22}$ m^{-3}. The layer will be divided into 50 sections.

Note that each bulk layer *must* consist of at least 3 points, that is, `n=3` or greater in a `bulk` command.

The heterojunction

The keyword `hb` between two `bulk` lines indicates that the transport between the two layers should be calculated using thermionic emission.

In principle, the command `hb` should always be indicated between two `bulk` layers that have different sets of (x, y). If it is not present, the transport is calculated using simple drift and diffusion.

The quantum-well layers

A quantum well requires at least three lines of input. The first line begins with the keyword `qwb1`. This indicates the properties of the left-most barrier.[14] The next line begins with the keyword `qw` and indicates the properties of the well. Additional lines beginning with the keyword `qw` may be added in case a more complicated well structure is desired (beyond a simple barrier-well-barrier type structure). The quantum-well definition ends with a line that

[14] We use the term "left-most" simply as a reference for relative position. There is no special meaning in it being "on the left".

starts with the keyword `qwb2`. In the current version of PinSim, this layer must have the same value of (x, y) as the `qwb1` layer.

Example:

```
qwb1 x=0.21 y=0.45 n=50 na=0.e24 nd=0.0e22 l=10e-9
qw x=0.47 y=1 n=50 na=0.e24 nd=0.0e22 l=10e-9
qwb2 x=0.21 y=0.45 n=50 na=0.e24 nd=0.0e22 l=10e-9
```

will provide a quantum well with 10-nm wide $In_{0.79}Ga_{0.21}As_{0.45}P_{0.55}$ barriers and a 10-nm wide $In_{0.53}Ga_{0.47}As$ well. The layers are undoped. The number of steps is actually ignored for quantum wells. The reason is that we want a good resolution when we calculate the wavefunctions in the well. PinSim automatically uses a 0.4-nm resolution in the well layers, `qwb1`, `qw`, and `qwb2`.

Applied voltage

The DC voltage is indicated with the variable `v`. For example,

```
v=2.0
```

sets the electrostatic voltage to -2 V (when the p-contact layer comes before the n-contact in the structure file!). To find the corresponding applied voltage, the built-in voltage must be added. Example: For a built-in voltage of 1.3 V, and with `v=2.0`, the applied bias is -0.7 V. The unit for `v` is volts.

Time steps

The time step is indicated using the variable `tstep`. As an example,

```
tstep=0.1e-12
```

will set the time step to 100 fs. The unit is seconds.

Total time

The total time to step through is indicated using the variable `ttot`. Example:

```
ttot=100e-12
```

will advance to 100 ps (in time steps given by `tstep`). The unit is seconds.

Time ramping

It is often desirable to increase the time step from a certain point, for instance after a short optical excitation that requires a finer resolution. If `ramp` is positive, this value will be used as the time offset for a ramping process

during which the time step `tstep` (originally set as explained above) is gradually increased by 100 fs for each time step. This ramping continues until an additional 100 fs would increase the time step beyond the value of the variable `t_ramp`. At this point `tstep` is set to `t_ramp`. Example:

```
ramp=5e-12
t_ramp=1e-12
```

will start the ramping at 5 ps, whereby the variable `tstep` is increased by 100 fs for each time step, until `tstep`=1 ps (or more, in which case `tstep` is set to 1 ps). The ramping then stops, and the calculations proceed using a time step of 1 ps.

AC voltage swing

The applied voltage can be modulated over time. A modulated applied voltage is indicated by using the variable `dv`. As an example,

```
dv=0.3
```

will provide a voltage swing of 0.3 V on both sides of the DC bias (`v`). If `v=2.0`, the bias will vary between -1.7 V and -2.3 V. The modulation is a sine-modulation, and the frequency of the modulation is given by the variable `f` explained below.

The voltage frequency

The variable `f` indicates the sinusoidal frequency of the applied AC swing (determined by the variable `dv`). For instance,

```
f=40e9
```

indicates that a 40-GHz frequency be applied. The unit is Hz.

The spectrum switch

The keyword `spec` indicates that a full absorption spectrum should be calculated. In this case, PinSim applies the desired voltage across the structure and calculates the resulting absorption spectrum. The only useful information produced in this case is the absorption spectrum and the bound states. Note that the bound states are only written if the keyword `spec` is present.

The full spectrum is always written by PinSim. The `spectrum` switch makes PinSim exit after calculating the absorption spectrum, and it increases the resolution of the absorption spectrum.

The `end` command

The command `end` indicates the end of the structure file. Anything that follows the `end` command is ignored.

E.2 Example file

```
This text is ignored
start

# ******* p-doped:
bulk x=0.0 y=0.0 n=50 na=1.e24 nd=0.0e22 l=500e-9
bulk x=0.0 y=0.0 n=10 na=1.e24 nd=0.0e22 l=50e-9
# ******* undoped:
hb
bulk x=0.456e0 y=0.8e0 n=50 na=0.e24 nd=0.0e22 l=5e-9
qwb1 x=0.456e0 y=0.8e0 n=50 na=0.e24 nd=0.0e22 l=10e-9
qw x=0.341e0 y=0.8e0 n=50 na=0.e24 nd=0.0e22 l=10e-9
qwb2 x=0.456e0 y=0.8e0 n=50 na=0.e24 nd=0.0e22 l=10e-9

qwb1 x=0.456e0 y=0.8e0 n=50 na=0.e24 nd=0.0e22 l=10e-9
qw x=0.341e0 y=0.8e0 n=50 na=0.e24 nd=0.0e22 l=10e-9
qwb2 x=0.456e0 y=0.8e0 n=50 na=0.e24 nd=0.0e22 l=10e-9
# Want to use the line below? Uncomment it!
# bulk x=0.0 y=0.0 n=50 na=0.e24 nd=0.0e22 l=5e-9
bulk x=0.456e0 y=0.8e0 n=50 na=0.e24 nd=0.0e22 l=5e-9
hb
# ******* n-doped:
bulk x=0.0 y=0.0 n=10 na=0e24 nd=1.5e24 l=50e-9
bulk x=0.0 y=0.0 n=50 na=0e24 nd=1.5e24 l=500e-9

# bias
v=-2.0
# ----- Time variables:
# time step, 200 fs:
tstep=2e-13
# stop at 7 ps:
ttot=7e-12

end
ignored line, Hello world!
```

Figure E.1: Sample structure file.

Appendix F

Input parameters

Beside the structure file, which contains the description of the epitaxial structure, other variables are required by PinSim.

Both physical parameters (such as the wavelength and the power level of the incoming light) and control parameters (that control the behavior of the numerical engine) must be given to PinSim. In the following, we explain the meaning of the various input parameters.

`E_trans` The photon energy for the optical field. Default: `E_trans`=0.8 [unit: eV].

`fownor` If set to 1, Fowler-Nordheim tunneling is included. If set to 0, it is left out. Default: `fownor=0`.

`hh` If set to 1, heavy hole well states are included in the calculations. If set to 0, they are left out. Default: `hh=1`.

`I0` The base value for the intensity that excites the structure. This is the intensity that excites the structure in steady-state calculations. See also `W_fact`. Default: `I0=0.0` [unit: W/m^{-2}].

`ionized` If set to 1, the program uses full ionization, if set to 0, it uses eqs. (4.8) and (4.9). Default: `ionized=0`.

`lh` Same as `hh`, but for light holes. Default: `lh=1`.

`lu_model` Line-up model. If set to 1, a constant 43/57 line-up is used. If set to 2, the Tersoff line-up model is used. Default: `lu_model=1`.

`n3d_min,n3d_max` Variables that keep the 3D densities from assuming unphysical values. It keeps all 3D electron and hole concentrations above `n3d_min` and below `n3d_max`. Default: `n3d_min=1.0e2, n3d_max=1.0e28` [unit: m^{-3}].

`n2d_min,n2d_max` Same as `n3d_min` and `n3d_max`, respectively, except it controls the well densities. Default: `n2d_min=1.0, n2d_max=1.0e21` [unit: m^{-2}].

`np2d` Controls how much of the most recently calculated wavefunctions and eigenenergies is mixed with those found in the previous iteration. The value should be around 0.2. A low value can prevent self-consistency in the solution, and a high value may cause numerical problems. Default: `np2d=0.2`.

`nimp` An n-impurity density used all the way through the structure. Default: `nimp=0.9e22` [unit: m^{-3}].

`no_wf` How many well states to include in the calculations. Default: `no_wf=2`.

`printtos` A debugging parameter. If set to 1, the program will write out all sorts of information to the screen. Hardly useful for people other than yours truly. Default: `printtos=0`.

`plotter` If set to 1, the program will plot the nominal banddiagrams and exit. Useful as a partial check that the structure has been coded correctly in the structure file. Default: `plotter=0`.

`philimit` This is a variable that keeps the electrostatic potential from runaway during the solution of the problem. It is usually a good idea to set it to 1 (on) when a solution must be found from scratch. However, if one is investigating other types of devices, such as transistors, it **must** be 0 (off) due to the special field distribution in those devices. Default: `philimit=0`.

`renorm` When set to 1, band gap renormalization is included as explained is Sec. 4.9. Default: `renorm=0`.

`ring` If set to 1, will make PinSim sound three consecutive beeps every time a solution has been found, either a steady-state solution or a time-step solution during a time-dependent calculation. May not work on systems other than UNIX and Linux. Default: `ring=0`.

`so_model` Which sweep-out model to use. `"te"`: Thermionic escape and thermionic recapture; `"t0"`: Thermionic escape, no recapture; `"tt"`: Uses thermionic escape, and `t_cap_e` and `t_cap_h` for the electron and hole capture times, respectively. Default: `so_model="te"`.

`STPMAX, STPFAC` Control parameters that are used to control the convergence speed. A good set of values is `STPMAX=1e3, STPFAC=1e1`. Only `STPMAX` should be changed, and a value of `STPMAX=1e2` will provide a more "safe", but slower convergence. A value higher than `1e3` for `STPMAX` often destabilizes the convergence process. Default: `STPMAX=1e2, STPFAC=1e1`.

`twodcont` A control parameter that indicates what fractions of the actual 2D carrier densities are included into the Poisson equation. Must be "1" to find the correct solution, but may be decreased in case the 2D carrier density contributions hampers convergence (I have never used it!). Default: `twodcont=1.0`.

`t_cap_e` Capture time for electrons. Only used if `so_model="tt"`. Default: `t_cap_e=10e-12` [unit: s].

`t_cap_h` Same as `t_cap_e`, but for holes. Default: `t_cap_h=10e-12` [unit: s].

`TE` If set to one, the input light is assumed to be TE-polarized. If set to 0, the input light is assumed to be TM-polarized. Default: `TE=1`.

`wfupdate` How many iterations to go through before updating the well states (that is, solve the Schrödinger equation again). A good value is 20. For very "wild" problems, a larger value may be required to begin with, such as 100. If the value is above 100, wavefunctions are not updated at all. Default: `wfupdate=5`.

`W_fact` In time-dependent calculations, the structure is always excited with a 1-ps (FWHM) long pulse. The peak intensity of the pulse is given by `W_fact*I0`. This pulse is added to a constant intensity of `I0`. See also `I0`. Default: `W_fact=1e4`.

Appendix G

Tips and troubleshooting

Here, we describe how to get the numerical engine to solve a problem. In the in-data file described in Appendix F, there are a number of parameters that can be adjusted to help the convergence process along.

With the large number of unknowns, and the complex, non-linear character of the equations we solve, there is no one set of parameters that will work for all problems.

When the control parameters are changed from their default values, the procedure is to find the solution with the modified values and to then use this solution as a first guess in a simulation where the control parameters have been put back to their default values.

Point distribution

The program does not check the distribution of points across the structure. The user must provide this information. The step size is given by the length of a layer divided by the number of points in that layer (see Fig. E.1 in Appendix E). Here are some recommendations as to how a structure should be discretized:

- Around *heterobarriers*, a step size of ≈ 1 nm is sufficient, and the step size should be the same on the two sides.
- In *bulk* regions, any step size can be used. If one expects a substantial change in any the variables (either n, p or ϕ) in a certain region, a

higher number of points will be necessary. A step size of 1 nm is often appropriate. In the highly doped regions, a value of 10 nm or even more can be used.

- In the quantum well region, a certain resolution is needed for the calculation of the bound states. In principle one can of course use a relatively coarse resolution, but the wavefunctions will then not be properly resolved. In the present version of PinSim, the resolution is set to 0.4 nm and cannot be adjusted.

How to approach a problem

When a structure has been set up using the commands described in Appendix E, the first task is to find a steady-state solution. One may be interested in the steady-state solution itself, or the steady-state solution is needed as the first step in a time-dependent calculation.

PinSim uses a certain initial guess for all problems. The initial guess can not be adjusted, but PinSim's guess has worked for all of the structures and all the conditions considered in this thesis.

Even though one may be interested in finding the steady state for some specific applied bias other than the built-in voltage, the solution for `v=0.0` should be found first. After this solution has been found, it can be used as an initial guess with the applied bias of interest.

Cannot find even `v=0.0` solution

If one is using thermionic recapture, this can very well give problems when trying to find the initial, `v=0.0` solution. This problem can usually be solved by eliminating the capture current to begin with, which is done by putting `so_model=t0`. Then, this solution is used as initial guess after having set `so_model` to the desired value. One may also try to find the solution for `v=0.2` or `v=-0.2` instead of `v=0`, still with `so_model=t0`.

Another possibility is to change `n3d_min` and `n3d_max` and/or their well equivalents, `n2d_min` and `n2d_max`. Typically, putting `n3d_min=1e16` and `n3d_max=1e25` will help. Try also `n2d_min=1e10` and `n2d_max=1e18`. Remember to adjust the values back to ensure that the real solution is found.

See also the section "There are problems when the bias is changed" below.

There are problems when the bias is changed

When a solution is found for one value of the applied bias, using this guess to find the solution to another problem for the same structure is always the best approach. However, when the bias is changed, the carrier density is depleted in one end of the structure (this is a numerical problem and not something we can control). By putting `philimit=1`, the problems associated with this effect can very often be eliminated. Remember to put `philimit=0` and use the `philimit=1` guess to ensure that the real solution is indeed found.

Another problem may be that the bias is changed to much at a time. If one solution is found for `v=0.0`, and one tries to use this solution to find the solution for `v=-3.0`, this may not work. Try finding the solution for `v=-1.0` instead, then use this to find the solution for `v=-2.0` and so on.

The iterations do not converge – they cycle around

Try using `STPMAX=1e2`. A higher value may give numerical problems. Try also using `wfupdate=50` (wavefunction update every 50 iterations) or even `wfupdate=105` (no update). Once the solution is found, `wfupdate` should be reduced to ensure that the solution found with the less frequent update of the wavefunctions is correct. With no updates of the wavefunctions, the solution will most likely be incorrect (unless the real solution was used as a first guess!).

The convergence is very slow

If the structure has many points, the iterations will be slow. The calculation time grows approximately as N^2, N being the number of variables (this is approximately 3 x *number of physical points*). There are two solutions to this problem:

1. Be patient,
2. Reduce number of physical points.

Another reason that convergence may be slow is that the step length between iterations is small. Try using `STPMAX=1e3` and `STPFAC=1e1`.

Bibliography

[1] W. Franz, "Einfluss eines elektrischen feldes auf einen optische absorptionskante," *Z. Naturforsch. A*, vol. Teil A 13, pp. 484–489, 1958.

[2] L. V. Keldysh, "The effect of a strong electric field on the optical properties of insulating crystals," *Zh. Eksp. Teor. Fiz.*, vol. 34, pp. 1138–1141, 1958.

[3] D. A. B. Miller, D. S. Chemla, T. C. Damen, A. C. Gossard, W. Wiegmann, T. H. Wood, and C. A. Burrus, "Band-Edge Electroabsorption in Quantum Well Structures: The Quantum-Confined Stark Effect," *Phys. Rev. B*, vol. 53, no. 22, pp. 2173–2176, 1984.

[4] D. A. B. Miller, D. S. Chemla, T. C. Damen, A. C. Gossard, W. Wiegmann, T. H. Wood, and C. A. Burrus, "Electric field dependence of optical absorption near the band gap of quantum-well structures," *Phys. Rev. B*, vol. 32, no. 2, pp. 1043–1060, 1985.

[5] D.A.B. Miller, D.S. Chemla, and S. Schmitt-Rink, "Relation between electroabsorption in bulk semiconductors and in quantum wells: the quantum-confined Franz-Keldysh effect," *Phys. Rev. B*, vol. 33, no. 10, pp. 6976–82, 1986.

[6] T.H. Wood, "Multiple Quantum Well (MQW) Waveguide Modulators," *J. Lightwave Technol.*, vol. 6, no. 6, pp. 743–57, 1988.

[7] A. Frova and P. Handler, "Shift of optical absorption edge by an electric field: Modulation of light in the space-charge region of a Ge p-n junction," *Appl. Phys. Lett.*, vol. 5, pp. 11–13, 1964.

[8] G. E. Stillman, C. M. Wolfe, C. O. Bozler, and A. Rossi, "Electroabsorption modulators in GaAs and its application to waveguide detectors and modulators," *Appl. Phys. Lett.*, vol. 28, pp. 544–546, 1976.

[9] T.H. Wood, C.A. Burrus, D.A.B. Miller, D.S. Chemla, T.C. Damen, A.C. Gossard, and W. Weigmann, "High-speed optical modulation with GaAs/GaAlAs quantum wells in a p-i-n diode structure," *Appl. Phys. Lett.*, vol. 44, no. 1, pp. 16–18, 1984.

[10] R. Dingle, W. Wiegmann, and C.H. Henry, "Quantum states of confined carriers in very thin $Al_xGa_{1-x}As$-GaAs-$Al_xGa_{1-x}As$ heterostructures," *Phys. Rev. Lett.*, vol. 33, no. 14, pp. 827–30, 1974.

[11] S. Nojima and K. Wakita, "Optimization of quantum well materials and structures for excitonic electroabsorption effects," *Appl. Phys. Lett.*, vol. 53, no. 20, pp. 1958–60, 1988.

[12] J. S. Weiner, D. S. Chemla, D. A. B. Miller, T. H. Wood, D. Sivco, and A. Y. Cho, "Room-temperature excitons in 1.6-μm band-gap GaInAs/AlInAs," *Appl. Phys. Lett.*, vol. 46, no. 7, pp. 619–621, 1985.

[13] J. S. Weiner, D. A. B. Miller, D. S. Chemla, T. C. Damen, C. A. Burrus, T. H. Wood, A. C. Gossard, and W. Wiegmann, "Strong polarization-sensitive electroabsorption in GaAs/AlGaAs quantum well waveguides," *Appl. Phys. Lett.*, vol. 47, no. 11, pp. 1148–1150, 1985.

[14] T. H. Wood, E. C. Carr, C. A. Burrus, R. S. Tucker, and T. H. Chiu, "High-speed waveguide optical modulator made from GaSb/AlGaSb multiple quantum wells (MQW's)," *Electron. Lett.*, vol. 23, pp. 540–542, 1987.

[15] H. Soda, K. Nakai, H. Ishikawa, and H. Imai, "High-speed GaInAsP/InP buried-heterostructure optical intensity modulator with semi-insulating InP burying layers," *Electron. Lett.*, vol. 23, pp. 1232–1234, 1987.

[16] T. H. Wood, E. C. Carr, C. A. Burrus, B. I. Miller, and U. Koren, "Large electroabsorption effect in GaInAs/InP multiple quantum well (MQW) optical modulator grown by OMVPE," *Electron. Lett.*, vol. 24, no. 14, pp. 840–841, 1988.

[17] A. J. Moseley, D. J. Robbins, A. C. Marshall, M. Q. Kearsley, and J. I. Davies, "Quantum confined Stark effect in GaInAs/InP single quantum wells grown by low pressure MOVPE," *Electron. Lett.*, vol. 24, no. 21, pp. 1301–1302, 1988.

[18] K. Wakita, I. Kotaka, H. Asai, S. Nojima, and O. Mikami, "High-efficienct electroabsorption in quarternary AlGaInAs quantum-well optical modulators," *Electron. Lett.*, vol. 24, no. 21, pp. 1324–1325, 1988.

[19] G. P. Kothiyal, S. Hong, N. Debbar, P. K. Bhattacharay, and J. Singh, "Enhancement in excitonic absorption due to overlap in heavy-hole and light-hole excitons in GaAs/InAlGaAs," *Appl. Phys. Lett.*, vol. 51, no. 14, pp. 1091–1093, 1987.

[20] Y. Kawamura, K. Wakita, Y. Itaya, Y. Yoshikuni, and H. Asahi, "Monolithic integration of InGaAsP/InP DFB lasers and InGaAs/InAlAs MQW optical modulators," *Electron. Lett.*, vol. 22, pp. 242, 1986.

[21] Y. Kawamura, K. Wakita, Y. Yoshikuni, Y. Itaya, and H. Asahi, "Monolithic integration of a DFB laser and an MQW optical modulator in the 1.5-μm wavelength range," *J. Quantum Electron.*, vol. QE-23, pp. 915, 1987.

[22] M. Suzuki, M. Noda, Y. Tanaka, S. Akiba, Y. Kushiro, and H. Isshiki, "Monolithic integration of InGaAsP/InP ditributed feedback laser and electroabsorption modulator by vapor phase expitaxy," *J. Lightwave Technol.*, vol. LT-5, pp. 1277–1285, 1987.

[23] T.H. Wood, J.Z. Pastalan, C.A. Burrus, Jr., B.C. Johnson, B.I. Miller, J.L. deMiguel, U. Koren, and M.G. Young, "Electric field screening by photogenerated holes in multiple quantum wells: A new mechanism for absorption saturation," *Appl. Phys. Lett.*, vol. 57, no. 11, pp. 1081–3, 1990.

[24] M. Suzuki, H. Tanaka, and Y. Matsushima, "10 Gbit/s optical demultiplexing and switching by sinusoidally driven InGaAsP electroabsorption modulators," *Electron. Lett.*, vol. 28, no. 10, pp. 934–935, 1992.

[25] M. Suzuki, H. Tanaka, and Y. Matsushima, "InGaAsP Electroabsorption Modulator for High-Bit-Rate EDFA System," *IEEE J. Photon. Technol. Lett.*, vol. 4, no. 6, pp. 586–8, 1992.

[26] M. Suzuki, H. Tanaka, N. Edagawa, and Y. Matsushima, "New Applications of a Sinusoidally Driven InGaAsP Electroabsorption Modulators to In-Line Optical Gates with ASE Noise Reduction Effect," *Electron. Lett.*, vol. 28, no. 10, pp. 934–935, 1992.

[27] M. Aoki, M. Suzuki, M. Takahashi, H. Sano, T. Ido, T. Kawano, and A. Takai, "High-speed (10 Gbit/s) and low-drive-voltage (1 V peak to peak) InGaAs/InGaAsP MQW electroabsorption-modulator integrated DFB laser with semi-insulating buried heterostructure," *Electron. Lett.*, vol. 28, no. 12, pp. 1157–1158, 1992.

[28] J. E. Zucker, K. L. Jones, T. H. Chiu, B. Tell, and K. Brown-Goebeler, "Strained Quantum Wells for Polarization-Independent Electrooptic Waveguide Switches," *J. Lightwave Technol.*, vol. 10, no. 12, pp. 1926–1930, 1992.

[29] K.G. Ravikumar, T. Aizawa, S. Suzaki, and R. Yamauchi, "Observation of polarization independent electric field effect in InGaAs/InP tensile strained quantum well and its proposal for optical switch," *Appl. Phys. Lett.*, vol. 61, no. 16, pp. 1904–1906, 1992.

[30] S. Chelles, R. Ferreira, P. Voisin, A. Ougazzaden, M. Allovon, and A. Carence, "Efficient polarization insensitive electroabsorption modulator using strained InGaAsP-based quantum wells," *Appl. Phys. Lett.*, vol. 64, no. 26, pp. 3530–3532, 1994.

[31] G. Mak, C. Rolland, K. E. Fox, and C. Blaauw, "High-Speed Bulk InGaAsP-InP electroabsorption Modulators with Bandwidth in Excess of 20 GHz," *IEEE J. Photon. Technol. Lett.*, vol. 2, no. 10, pp. 730–733, 1990.

[32] I. Kotaka, K. Wakita, K. Kawano, H. Asai, and M. Naganuma, "High-speed and low-driving-voltage InGaAs/InAlAs multiquantum well optical modulators," *Electron. Lett.*, vol. 27, no. 23, pp. 2162–2163, 1991.

[33] F. Devaux, E. Bigan, A. Ougazzaden, B. Pierre, F. Huet, M. Carré, and A. Carenco, "InGaAsP/InGaAsP Multiple-Quantum-Well Modulator

with Improved Saturation Intensity and Bandwidth Over 200 GHz," *IEEE J. Photon. Technol. Lett.*, vol. 4, no. 7, pp. 720 –723, 1992.

[34] F. Devaux, S. Chelles, A. Ougazzaden, A. Mircea, F. Huet, and M. Carré, "10 Gbit/s operation of polarisation insensitive, strained InGaAsP/InGaAsP MQW electroabsorption modulator," *Electron. Lett.*, vol. 29, no. 13, pp. 1201–1203, 1993.

[35] F. Devaux, F. Dorgeuille, A. Ougazzaden, F. Huet, M. Carré, A. Carenco, M. Henry, Y. Sorel, J.-F. Kerdiles, and E. Jeanney, "20 Gbit/S Operation of a High-Efficiency InGaAsP/InGaAsP MQW Electroabsorption Modulator with 1.2-V Drive Voltage," *IEEE J. Photon. Technol. Lett.*, vol. 5, no. 11, pp. 1288 –1290, 1993.

[36] F. Devaux, S. Chelles, A. Ougazzaden, A. Mircea, M. Carré, F. Huet, A. Carenco, Y. Sorel, J. F. Kerdiles, and M. Henry, "Full Polarization Insensitivity of a 20 Gb/s Strained-MQW Electroabsorptin Modulator," *IEEE J. Photon. Technol. Lett.*, vol. 6, no. 10, pp. 1203–1206, 1994.

[37] T. Ido, H. Sano, D.J. Moss, S. Tanaka, and A. Takai, "Strained InGaAs/InAlAs MQW Electroabsorption Modulators with Large Bandwidth and Low Driving Voltage," *IEEE J. Photon. Technol. Lett.*, vol. 6, no. 10, pp. 1207–1209, 1994.

[38] F. Devaux, S. Muller, A. Ougazzaden, A. Mircea, A. Ramdane, P. Krauz, J. Semo, F. Huet, M. Carré, and A. Carenco, "Zero-loss multiple-quantum-well electroabsorption modulator with very low chirp," *Appl. Phys. Lett.*, vol. 64, no. 8, pp. 954–956, 1994.

[39] D. G. Moodie, A. D. Ellis, and C. W. Ford, "Generation of 6.3 ps optical pulses at a 10 GHz repetition rate using a packaged electroabsorption modulator and dispersion compensating fibre," *Electron. Lett.*, vol. 30, no. 20, pp. 1700–1701, 1994.

[40] T. Ido, S. Tanaka, M. Suzuki, and H. Inoue, "MQW electroabsorption optical modulator for 40 Gbit/s modulation," *Electron. Lett.*, vol. 31, no. 24, pp. 2124–2125, 1995.

[41] T. Ido, S. Tanaka, M. Suzuki, M. Koizumi, H. Sano, and H. Inoue, "Ultra-High-Speed Multiple-Quantum-Well Electro-Absorption Optical Modulators with Integrated Waveguides," *J. Lightwave Technol.*, vol. 14, no. 9, pp. 2026–34, 1996.

[42] R.Y.-F. Yip, P. Desjardins, L. Isnard, A. Ait-Ouali, A. Bensaada, H. Marchand, J.L. Brebner, J.F. Currie, and R.A. Masut, "Band alignment and barrier height considerations for the quantum-confined Stark effect," *J. Vac. Sci. Technol. A*, vol. 16, no. 2, pp. 801–4, 1998.

[43] T. H. Wood, C. A. Burrus, D. A. B. Miller, D. S. Chemla, T. C. Damen, A. C. Gossard, and W. Wiegmann, "131 ps Optical Modulation in Semiconductor Multiple Quantum Wells (MQW's)," *IEEE J. Quantum Electron.*, vol. QE-21, no. 2, pp. 117–118, 1985.

[44] M. Suzuki, H. Tanaka, K. Utaka, N. Edagawa, and Y. Matsushima, "Transform-limited 14 ps optical pulse generation with 15 GHz repetition rate by InGaAsP electroabsorption modulator," *Electron. Lett.*, vol. 28, no. 11, pp. 1007–1008, 1992.

[45] K. Wakita, K. Sato, I. Kotaka, M. Yamamoto, and M. Asobe, "Transform-Limited 7-ps Optical Pulse Generation Using a Sinusoidally Driven InGaAsP/InGaAsP Strained Multiple-Quantum-Well DFB Laser/Modulator Monolithically Integrated Light Source," *IEEE J. Photon. Technol. Lett.*, vol. 5, no. 8, pp. 899–901, 1993.

[46] O. Mitomi, I. Kotaka, K. Wakita, S. Nojima, K. Kawano, Y. Kawamura, and H. Asai, "40-GHz bandwidth InGaAs/InAlAs multiple quantum well optical intensity modulator," *Appl. Optics*, vol. 31, no. 12, pp. 2030–5, 1992.

[47] F. Devaux, P. Bordes, A. Ougazzaden, M. Carré, and F. Huet, "Experimental optimisation of MQW electroabsorption modulators with up to 40 GHz bandwidths," *Electron. Lett.*, vol. 30, no. 16, pp. 1347 –1348, 1994.

[48] D. G. Moodie, P. J. Cannard, A. J. Dann, C. W. Ford, J. Reed, R. T. Moore, J. K. Lucek, and A. D. Ellis, "Low polarisation sensitivity electroabsorption modulators for 160 Gbit/s networks," *Electron. Lett.*, vol. 33, no. 24, pp. 2068–2070, 1997.

[49] A.D. Ellis, J.K. Lucek, D. Pitcher, D.G. Moodie, and D. Cotter, "Full 10 x 10 Gbit/s OTDM data generation and demultiplexing using electroabsorption modulators," *Electron. Lett.*, vol. 34, no. 18, pp. 1766–1767, 1998.

[50] I. D. Phillips, A. Gloag, D. G. Moodie, N. J. Doran, I. Bennion, and A. D. Ellis, "Simultaneous demultiplexing and clock recovery using a single electroabsorption modulator in a novel bi-directional configuration," *Opt. Commun.*, vol. 150, pp. 101–105, 1998.

[51] S. Højfeldt, S. Bischoff, and J. Mørk, "All-optical wavelength conversion and signal regeneration using an electroabsorption modulator," in *Tech. Dig. LEOS'99*, 1999.

[52] V. Kaman, A. J. Keating, S. Z. Zhang, and J. E. Bowers, "Simultaneous OTDM Demultiplexing and Detection Using an Electroabsorption Modulator," *J. Lightwave Technol.*, vol. 12, no. 6, pp. 711–713, 2000.

[53] G. Mikkelsen, B. Raybon and R.-J. Essiambre, "160 Gb/s TDM Transmission Systems," in *Proceedings of ECOC 2000*, 2000.

[54] D. T. K. Tong, Kung-Li Deng, B. Mikkelsen, G. Raybon, K. F. Dreyer, and J. E. Johnson, "160 Gbit/s clock recovery using electroabsorption modulator-based phase-locked loop," *Electron. Lett.*, vol. 36, no. 23, pp. 1951–1952, 2000.

[55] J. Yu, K. Kojima, N. Chaud, M. C. Fischer, R. Espindola, and T. G. B. Mason, "160 Gb/s single-channel unrepeatered transmission over 200 km of non-zero dispersion shifted fiber," in *Proc. ECOC'01*, Madrid, Spain, 2001, pp. 20–21.

[56] H. T. Yamada, H. Murai, A. R. Pratt, and Y. Ozeki, "Scalable 80 Gbit/s OTDM using a modular architecture based on EA modulators," in *Proceedings of ECOC 2001*, 2001, pp. 47–48.

[57] L.K. Oxenløwe, E. Hilliger, A. Tersigni, A.M. Nik, S. Højfeldt, F. Romstad, K. Yvind, P.M.W. Skovgaard, K. Hoppe, and J. Hanberg, "All-optical Demultiplexing and Wavelength Conversion in an Electroabsorption Modulator," in *Proc. ECOC'01*, Madrid, Spain, 2001, pp. 604–605.

[58] N. Edagawa, M. Suzuki, and S. Yamamoto, "Novel wavelength converter using an electroabsorption modulator: conversion experiments at up to 40 Gbit/s," in *Tech. Dig. OFC'97*, 1997, vol. 6 of *1997 Technical Digest Series*, pp. 77–78.

[59] G. Raybon, U. Koren, B. I. Miller, M. Chien, K. Dreyer, S. Chandrasekhar, R. E. Behringer, D. M. Tennant, and K. Feder, "Reconfigurable Optoelectronic Wavelength Translation Based on an Integrated Electroabsorption Modulated Laser Array," *IEEE J. Photon. Technol. Lett.*, vol. 10, no. 2, pp. 215–217, 1998.

[60] P. S. Cho, D. Mahgerefteh, and J. Goldhar, "All-Optical 2R Regeneration and Wavelength Conversion at 20 Gbit/s Using an Electroabsorption Modulator," *IEEE J. Photon. Technol. Lett.*, vol. 11, no. 12, pp. 1662–1664, 2001.

[61] H. Yokoyama, Y. Hashimoto, and H. Kurita, "Noise reduction in optical pulses and bit-error-rate improvement with a semiconductor-waveguide saturable absorber," in *Tech. Dig. CLEO'98*, 1998, vol. 6 of *1998 Technical Digest Series*, pp. 502–503.

[62] N. Edagawa, M. Suzuki, and S. Yamamoto, "Novel Wavelength Converter Using an Electroabsorption Modulator," *IEICE Trans. Electron.*, vol. E81-C, no. 8, pp. 1251–1257, 1998.

[63] T. Miyazaki, T. Otani, N. Edagawa, M. Suzuki, and S. Yamamoto, "Novel Optical-Regenerator Using Electroabsorption Modulators," *IEICE Trans. Commun.*, vol. E82-B, no. 8, pp. 1148–1153, 1999.

[64] T. Otani, T. Miyazaki, and S. Yamamoto, "40 Gbit/s signal transmission using optical 3R regenerator based on electroabsorption modulator," in *Proceedings of OFC 2000*, 2000.

[65] H. Tanaka, M. Hayashi, and T. Otani, "60 Git/s WDM-OTDM transmultiplexing using an electroabsorption modulator," in *Proceedings of OFC 2001*, 2001.

[66] M. Yamada, S. Ogita, M. Yamagishi, K. Tabata, N. Nakaya, M. Asada, and Y. Suematsu, "Polarization-dependent gain in GaAs/AlGaAs multi-quantum-well lasers: theory and experiment," *Appl. Phys. Lett.*, vol. 45, no. 4, pp. 324–5, 1984.

[67] Sugis Shim and El-Hang Lee, "Optimization of InGaAsP/InP quantum well heterostructures for enhanced excitonic electroabsorption effects at 1.55 mu m," *Appl. Phys. Lett.*, vol. 63, no. 17, pp. 2387–9, 1993.

[68] J. Micallef, E.H. Li, and B.L. Weiss, "Electroabsorption enhancement in disordered, strained InGaAs/GaAs quantum well," *Appl. Phys. Lett.*, vol. 67, no. 19, pp. 2768–70, 1995.

[69] E. M. Goldys, G. Nott, T. L. Tansley, M. Henini, M. A. Pate, and G. Hill, "Operation and Theoretical Analysis of the Multiple Asymmetric Coupled Quantum-Well Light Modulator in the n-i-n Configuration," *IEEE J. Quantum Electron.*, vol. 33, no. 7, pp. 1084–1088, 1997.

[70] Ku-ho Chung and Jong-in Shim, "A New Polarization-Insensitive 1.55-μm InGaAs(P)-InGaAsP Multiquantum-Well Electronabsorption Modulator Using a Strain-Compensating Layer," *IEEE J. Quantum Electron.*, vol. 35, no. 5, pp. 730–736, 1999.

[71] D. Meglio, P. Lugli, R. Sabella, and O. Sahén, "Analysis and Optimization of InGaAsP Electro-Absorption Modulators," *IEEE J. Quantum Electron.*, vol. 31, no. 2, pp. 261–268, 1995.

[72] A. V. Uskov, J. R. Karin, R. Nagarajan, and J. E. Bowers, "Dynamics of Carrier Heating and Sweepout in Waveguide Saturable Absorbers," *IEEE J. Sel. Top. Quantum Electron.*, vol. 1, no. 2, pp. 552–561, 1995.

[73] C. Glingener, D. Schulz, and E. Voges, "Modeling of Optical Waveguide Modulators on III-V Semiconductor," *IEEE J. Quantum Electron.*, vol. 31, no. 1, pp. 101–112, 1995.

[74] A. V. Uskov, J. R. Karin, J. E. Bowers, J. G. McInerney, J. L. Bihan, and R. Nagarajan, "Effects of Carrier Cooling and Carrier Heating in Saturation Dynamics and Pulse Propagation Through Bulk Semiconductor Absorbers," *IEEE J. Quantum Electron.*, vol. 34, no. 11, pp. 2162–2171, 1998.

[75] A. M. Fox, D. A. B. Miller, G. Livescu, J. E. Cunningham, and Jan W. Y, "Quantum Well Carrier Sweep Out: Relation to Electroabsorption and Excitonic Saturation," *IEEE J. Quantum Electron.*, vol. 27, no. 10, pp. 2281–2295, 1991.

[76] J. A. Cavaillès, D. A. B. Miller, J. E. Cunningham, P. Li Kam Wa, and A. Miller, "Simultaneous measurements of electron and hole sweep-out from quantum wells and modeling of photoinduced field screening dynamics," *IEEE J. Quantum Electron.*, vol. 28, no. 10, pp. 2486–2497, 1992.

[77] Massimo Gurioli, Juan Martinez-Pastor, Marcello Colocci, Christiane Deparis, Bruno Chastaingt, and Jean Massies, "Thermal escape of carriers out of GaAs/Al_xGa_{1-x}As quantum-well structures," *Phys. Rev. B*, vol. 46, no. 11, pp. 6922–6927, 1992.

[78] J. Nelson, M. Paxman, K.W.J. Barnham, J.S. Roberts, and C. Button, "Steady-State Carrier Escape from Single Quantum Wells," *IEEE J. Quantum Electron.*, vol. 29, no. 6, pp. 1460–8, 1993.

[79] David J. Moss, T. Ido, and H. Sano, "Calculation of Photogenerated Carrier Escape Rates from GaAs/GaAlAs Quantum wells," *IEEE J. Quantum Electron.*, vol. 30, no. 4, pp. 1015–1026, 1994.

[80] K.R. Lefebvre and A.F.M. Anwar, "Electron Escape Time from Single Quantum Wells," *IEEE J. Quantum Electron.*, vol. 33, no. 2, pp. 187–191, 1997.

[81] M. Ershov and V. Ryzhii, "Contact and distributed effects in quantum well infrared photdetectors," *Appl. Phys. Lett.*, vol. 67, no. 21, pp. 3147–3149, 1995.

[82] M. Ershov, C. Hamaguchi, and V. Ryzhii, "Device Physics and Modeling of Multiple Quantum Well Infrared Photodetectors," *Jpn. J. Appl. Phys.*, vol. 35, pp. 1395–1400, 1996.

[83] Victor Ryzhii, "High-frequency performance of single quantum well infrared photodetectors at high power densities," *IEEE J. Trans. Electron. Devices*, vol. 45, no. 8, pp. 1797–1803, 1998.

[84] Kenji Kawano, Koichi Wakita, Osamu Mitomi, Isamu Kotaka, and Mitsuru Naganuma, "Design of InGaAs-InAlAs Multiple-Quantum-Well (MQW) Optical Modulators," *IEEE J. Quantum Electron.*, vol. 28, no. 1, pp. 224–230, 1992.

[85] G.L. Li, Y. Z. Liu, R. B. Welstand, C.K. Sun, W.X. Chen, J. T. Zhu, S.A. Pappert, and P.K.L. Yu, "Harmonic Signals from Electroabsorption Modulators for Bias Control," *IEEE J. Photon. Technol. Lett.*, vol. 13, no. 10, pp. 1076–1078, 2001.

[86] G. Metzler and T. Schwander, "RF small-signal equivalent circuit of MQW InGaAs/lnAlAs electroabsorption modulator," *Electron. Lett.*, vol. 33, no. 21, pp. 1822–3, 1997.

[87] G.L. Li, P.K.L. Yu, W.S.C. Chang, K.K. Loi, C.K. Sun, and S.A. Pappert, "Concise RF equivalent circuit model for electroabsorption modulators," *Electron. Lett.*, vol. 36, no. 9, pp. 818–20, 2000.

[88] Mee K. Chin and William S. C. Chang, "Theoretical Design Optimization of Multiple-Quantum-Well Electroabsorption Waveguide Modulators," *IEEE J. Quantum Electron.*, vol. 29, no. 9, pp. 2476–2488, 1993.

[89] S. Oshiba, K. Nakamura, and H. Horikawa, "Low-Drive-Voltage MQW Electroabsorption Modulator for Optical Short-Pulse Generation," *IEEE J. Quantum Electron.*, vol. 34, no. 2, pp. 277–281, 1998.

[90] N. Tessler and G. Eisenstein, "Modelling carrier dynamics and small-signal modulation response in quantum-well lasers," *Optical and Quantum Electronics*, vol. 26, pp. S767–S787, 1994.

[91] Nir Tessler, *Dynamic Properties of Inverted Quantum Well Laser Structure*, Ph.D. thesis, Technion, Haifa, Israel, 1995.

[92] M. A. Alam, M. S. Hybertsen, R. Kent Smith, G. A. Baraff, and M. R. Pinto, "Simulation of Semiconductor Quantum Well Lasers," in *Proceedings of SPIE 1997*, 1997, vol. 2994, pp. 709–722.

[93] Matt Grupen and Karl Hess, "Simulation of Carrier Transport and Nonlinearities in Quantum-Well Laser Diodes," *IEEE J. Quantum Electron.*, vol. 34, no. 1, pp. 120–140, 1998.

[94] B. Witzigmann, A. Witzig, and W. Fichtner, "A multidimensional laser simulator for edge-emitters including quantum carrier capture," *IEEE J. Trans. Electron. Devices*, vol. 47, no. 10, pp. 1926–34, 2000.

[95] A. Ahland, D. Schulz, and E. Voges, "Modelling and Design of Electroabsorption Modulators on GaInAsP," *Int. J. Electron. Commun.*, vol. 52, no. 5, pp. 322–328, 1998.

[96] A. Ahland, D. Schulz, and E. Voges, "Nonlinear effects in blue-shift waveguide EAM's," *Optical and Quantum Electronics*, vol. 32, pp. 769–780, 2000.

[97] M. Wiedenhaus, A. Ahland, D. Schulz, and E. Voges, "Dynamical Simulation of Quantum-Well Structures," *J. Lightwave Technol.*, vol. 37, no. 5, pp. 684–690, 2001.

[98] S. Nakamura, Y. Ueno, K. Tajima, J. Sasaki, T. Sugimoto, T. Kato, T. Shimoda, M. Itoh, H. Hatakeyama, T. Tamanuki, and T. Sasaki, "168 Gb/s error-free demultiplexing with hybrid-integrated symmetric Mach-Zehnder all-optical switch," in *Proceedings of OFC 2000*, 2000.

[99] S. Diez, C. Schubert, R. Ludwig, H.-J. Ehrke, U. Feiste, C. Schmidt, and H. G. Weber, "160 Gbit/s all-optical demultiplexer using hybrid gain-transparent SOA Mach-Zehnder interferometer," *Electron. Lett.*, vol. 36, no. 17, 2000.

[100] S. Bischoff, J. Mørk, T. Franck, S. D. Brorson, M. Hofmann, K. Fröjd, L. Prip, and M. P. Sørensen, "Monolithic colliding pulse mode-locked semiconductor lasers," *Quantum Semiclass. Opt.*, vol. 9, pp. 655–674, 1997.

[101] J. Mørk and A. Mecozzi, "Theory of ultrafast optical response of active semiconductor waveguides," *J. Opt. Soc. Am. B*, vol. 13, no. 8, pp. 1803–1816, 1996.

[102] J. Mørk and J. Mark, "Time-resolved spectroscopy of semiconductor laser devices: Experiments and modelling," in *SPIE'95*, 1995, vol. 2399, pp. 146–159.

[103] P. J. Bradley, C. Rigo, and A. Stano, "Carrier Induced Transient Electric Fields in a p-i-n InP-InGaAs Multiple-Quantum-Well Modulator," *IEEE J. Quantum Electron.*, vol. 32, no. 1, pp. 43–52, 1996.

[104] H. Kurita, I. Ogura, and H. Yokoyama, "Ultrafast All-Optical Signal Processing with Mode-Locked Semiconductor Lasers," *IEICE Trans. Electron.*, vol. E81-C, no. 2, pp. 129–139, 1998.

[105] G. P. Agrawal and N. K. Dutta, *Semiconductor Lasers*, Van Nostrand Reinhold, New York, 1993.

[106] Siegfried Selberherr, *Analysis and Simulation of Semiconductor Devices*, Springer-Verlag, New York, 1994.

[107] Alan H. Marshak and Carolyn M. Van Vliet, "Electrical Current and Carrier Density in Degenerate Materials with Nonuniform Band Structure," *Proc. IEEE*, vol. 72, no. 2, pp. 148–164, 1984.

[108] M. Levinshtein, S. Rumyantsev, and M. Shur, Eds., *Volume 2: Ternary and Quarternary III-V Compounds*, Handbook Series on Semiconductor Parameters. World Scientific, Singapore, 1999.

[109] N. W. Ashcroft and N. D. Mermin, *Solid State Physics*, Holt, Rinehart and Winston, New York, 1976.

[110] H. Schneider and K. von Klitzing, "Thermionic emission and Gaussian transport of holes in a GaAs/$Al_xGa_{1-x}As$ multiple-quantum-well structure," *Phys. Rev. B*, vol. 38, no. 9, pp. 6160–6165, 1988.

[111] C. M. Wu and E. S. Yang, "Carrier transport across heterojunction interfaces," *Solid State Electron.*, vol. 22, pp. 241–248, 1979.

[112] M. Grupen, K. Hess, and G.H. Song, "Simulation of transport over heterojunctions," in *Proc. 4th International Conf. Simul. Semicon. Dev. Process.* 1991, vol. 4, pp. 303–311, IEEE Electron Devices Society.

[113] M. Lenzlinger and E.H. Snow, "Fowler-Nordheim Tunneling Into Thermally Grown SiO_2," *J. Appl. Phys.*, vol. 40, no. 1, pp. 278–83, 1969.

[114] S.N. Mohammad, G. Fiorenza, A. Acovic, J.B. Johnson, and R.L. Carter, "Fowler-Nordheim Tunneling Of Carriers in MOS Transistors: Two-Dimensional Simulation of Gate Current Employing FIELDAY," *Solid State Electron.*, vol. 38, no. 4, pp. 807–14, 1995.

[115] Dongsheng Hsu, "Effects of the Series Resistance on Fowler-Nordheim Tunneling Oscillations," *Solid State Electron.*, vol. 41, no. 3, pp. 513–14, 1997.

[116] Z.A. Weinberg, "On Tunneling in Metal-Oxide-Silicon Structures," *J. Appl. Phys.*, vol. 53, no. 7, pp. 5052–6, 1982.

[117] P.J. Price, "Resonant tunneling properties of heterostructures," *Superlatt. Microstruc.*, vol. 2, no. 6, pp. 593–6, 1986.

[118] G. Bastard, *Wave mechanics applied to semiconductor heterostructures*, Halsted Press, New York, 1988.

[119] Krister Fröjdh, *Carrier Transport Effects in Semiconductor Heterostructures for Optical Applications*, Ph.D. thesis, Royal Institute of Technology, Stockholm, Sweden, 1996.

[120] Peter J. Stevens, Mark Whitehead, Gareth Parry, and Karl Woodridge, "Computer Modeling of the Electric Field Dependent Absorption Spectrum of Multiple Quantum Well Material," *IEEE J. Quantum Electron.*, vol. 24, no. 10, pp. 2007–2016, 1988.

[121] B. Jonsson and S.T. Eng, "Solving The Schrodinger Equation in Arbitrary Quantum-Well Potential Profiles Using the Transfer Matrix Method," *IEEE J. Quantum Electron.*, vol. 26, no. 11, pp. 2025–35, 1990.

[122] T. Ikeda and H. Ishikawa, "Analysis Of the Attenuation Ratio Of MQW Optical Intensity Modulator for 1.55 μm Wavelength Taking Account of Electron Wave Function Leakage," *IEEE J. Quantum Electron.*, vol. 32, no. 2, pp. 284–292, 1996.

[123] H. Mimura, M. Hosoda, K. Tominaga, T. Watanabe, and K. Fujiwara, "Absorption saturation mechanism in short-period GaAs/AlAs superlattice self-electro-optic effect devices based on Wannier-Stark localization," *Solid State Electron.*, vol. 40, no. 1–8, pp. 171–174, 1996.

[124] J. P. Loehr and J. Singh, "Nonvariational numerical calculation of excitonic properties in quantum wells in the presence of strain, electric fields, and free carriers," *Phys. Rev. B*, vol. 42, no. 11, pp. 7154–7162, 1990.

[125] Pierluigi Debernardi and Paolo Fasano, "Quantum Confined Stark Effect in Semiconductor Quantum Wells Including Valence Band Mixing and Coulomb Effects," *IEEE J. Quantum Electron.*, vol. 29, no. 11, pp. 2741–2755, 1993.

[126] J. M. Luttinger and W Kohn, "Motion of Electrons and Holes in Perturbed Periodic Fields," *Phys. Rev.*, vol. 97, no. 4, pp. 869–883, 1955.

[127] Evan O. Kane, "Band structure of Indium Antimonide," *J. Phys. Chem. Solids.*, vol. 1, pp. 249–261, 1957.

[128] P. S. Zory, Jr., Ed., *Quantum Well Lasers*, Academic Press, Inc., San Diego, 1993.

[129] K. R. Lefebvre and A. F. M. Anwar, "Redistribution of the quantum well density of states under the influence of an electric field," *Semicond. Sci. Technol.*, vol. 12, pp. 1226–1230, 1997.

[130] Peter Blood, "On the Dimensionality of Optical Absorption, Gain, and Recombination in Quantum-Confined Structures," *IEEE J. Quantum Electron.*, vol. 36, no. 3, pp. 354–362, 2000.

[131] R. J. Elliot, "Intensity of optical absorption by excitons," *Phys. Rev.*, vol. 108, pp. 1384–1389, 1957.

[132] M. Sugawara, T. Fujii, S. Yamazaki, and K. Nakajima, "Theoretical and experimental study of the optical-absorption spectrum of exciton resonance in $In_{0.53}Ga_{0.47}As/InP$ quantum wells," *Phys. Rev. B*, vol. 42, no. 15, pp. 9587–9597, 1990.

[133] D. Campi and C. Coriasso, "Optical nonlinearities in multiple quantum wells: generalized Elliott formula," *Phys. Rev. B*, vol. 51, no. 16, pp. 10719–28, 1995.

[134] P. G. Eliseev and I. S. Tsimberova, "Nonradiative losses in InGaAsP/InP heterostructures," *Sov. J. Quantum Electron.*, vol. 19, no. 10, pp. 1334–1336, 1989.

[135] Y. Zou, J.S. Osinski, P. Grodzinski, P.D. Dapkus, W.C. Rideout, W.F. Sharfin, J. Schlafer, and F.D. Crawford, "Experimental Study Of Auger

Recombination, Gain, and Temperature Sensitivity of 1.5 μm Compressively Strained Semiconductor Lasers," *IEEE J. Quantum Electron.*, vol. 29, no. 6, pp. 1565–1575, 1993.

[136] Jasprit Singh, *Semiconductor Optoelectronics*, McGraw-Hill, Inc., USA, 1995.

[137] L. Davis, Y. Lam, D. Nichols, J. Singh, and P.K. Bhattacharya, "Auger Recombination Rates In Compressively Strained $In_xGa_{1-x}As$/InGaAsP/InP ($0.53 \leq x \leq 0.73$) Multiquantum Well Lasers," *IEEE J. Photon. Technol. Lett.*, vol. 5, no. 2, pp. 120–122, 1993.

[138] G. Fuchs, C. Schiedel, A. Hangleiter, V. Härle, and F. Scholz, "Auger recombination is strained and unstrained InGaAs/InGaAsP multiple quantum-well lasers," *Appl. Phys. Lett.*, vol. 62, no. 4, pp. 396–398, 1993.

[139] A. Ichii, Y. Tsou, and E. Garmire, "An empirical rule for band offsets between III-V alloy compounds," *J. Appl. Phys.*, vol. 74, no. 3, pp. 2112–2113, 1993.

[140] F Devaux, S Chelles, A Ougazzaden, A Mircea, and J C Harmand, "Electroabsorption modulators for high-bit-rate optical communications: A comparison of strained InGaAs/InAlAs and InGaAs/InGaAsP MQW," *Semicond. Sci. Technol.*, vol. 10, no. 7, pp. 887–902, 1995.

[141] J. Minch, S. H. Park, T. Keating, and S. L. Chuang, "Theory and Experiment of $In_{1-x}Ga_xAs_yP_{1-y}$ and $In_{1-x-y}Ga_xAl_yAs$ Long-Wavelength Strained Quantum-Well Lasers," *IEEE J. Quantum Electron.*, vol. 35, no. 5, pp. 771–782, 1999.

[142] S. L. Chuang, *Physics of Optoelectronic Devices*, Wiley, New York, 1995.

[143] J. Tersoff, "Theory of semiconductor heterojunctions: The role of quantum dipoles," *Phys. Rev. B*, vol. 30, no. 8, pp. 4874–4877, 1984.

[144] M. Beaudoin, P. Desjardins, A. Ait-Ouali, J. L. Brebner, R. Y.-F. Yip, H. Marchand, L. Isnard, and R. A. Masut, "Optical properties and heterojunction band alignment in fully coherent strain-compensated

$InGa_xP_{1-x}/Ga_yIn_{1-y}P$ multilayers on InP(001)," *J. Appl. Phys.*, vol. 87, no. 5, pp. 2320–2326, 2000.

[145] R.Y.-F. Yip, A. Ait-Ouali, A. Bensaada, P. Desjardins, B.M. Beaudoin, C.L. Isnard, J.L. Brebner, J.F. Currie, and R.A. Masut, "Strain and Relaxation Effects in InAsP/InP Multiple Quantum Well Optical Modulator Devices Grown by Metal-Organic Vapor Phase Epitaxy," *J. Appl. Phys.*, vol. 81, no. 4, pp. 1905–15, 1997.

[146] I. Vurgaftman and J. R. Meyer, "Band parameters for III-V compound semiconductors and their alloys," *J. Appl. Phys.*, vol. 89, no. 11, pp. 5815–5875, 2001.

[147] A. Mecozzi and J. Mørk, "Saturation Effects in Nondegenerate Four-Wave Mixing Between Short Optical Pulses in Semiconductor Laser Amplifiers," *IEEE J. Sel. Top. Quantum Electron.*, vol. 3, no. 5, pp. 1190 –1207, 1997.

[148] Z.-M. Li, "Physical models and numerical simulation of modern semiconductor lasers," *Proceeding of SPIE*, vol. 2994, pp. 698–708, 1997.

[149] J. Mørk, J. Mark, and C. P. Seltzer, "Carrier heating in InGaAsP laser amplifiers due to two-photon absorption," *Appl. Phys. Lett.*, vol. 64, no. 17, pp. 2206–2208, 1994.

[150] M.-R. Kim, C.-H. Kim, and B.-H. Han, "Band-gap renormalization and strain effects in semiconductor quantum wells," *Physica B*, vol. 245, pp. 45–51, 1998.

[151] D. Moss, D. Landheer, D. Conn, D. Halliday, S. Charbonneau, G. Aers, R. Barber, and F. Chatenoud, "High-Speed Photodetection in a Reverse Biased GaAs/AlGaAs GRINSCH SQW Laser Structure," *IEEE J. Photon. Technol. Lett.*, vol. 4, no. 6, pp. 609–611, 1992.

[152] L. R. Brovelli, J. Hugi, H. Jäckel, and H. Melchior, "Optical pulse mixing measurement of carrier lifetime and absorption recovery time in reverse-biased GaAs/AlGaAs single quantum well laser structures," *J. Appl. Phys.*, vol. 76, no. 12, pp. 7713–7717, 1994.

[153] G.L. Li, Y. Z. Liu, R. B. Welstand, C.K. Sun, W.X. Chen, J. T. Zhu, S.A. Pappert, and P.K.L. Yu, "Ultrahigh-speed Traveling-Wave

Electroabsorption Modulator-Design and Analysis," *IEEE Trans. Microwave Theory Tech.*, vol. 47, no. 7, pp. 1177–83, 1999.

[154] K. Yamada, H. Murai, K. Nakamura, H. Satoh, Y. Ozeki, and Y. Ogawa, "10-Gbit/s EA modulator module with a polarization dependence of less than 0.3 dB," in *OFC '95 Optical Fiber Communication. Summaries of Papers Presented at the Conference on Optical Fiber Communication*, 1995, vol. 8 of *1995 Technical Digest Series. Postconference Edition*, pp. 24–25.

[155] A. Ougazzaden and F. Devaux, "Strained InGaAsP/InGaAsP/InAsP multi-quantum well structure for polarization insensitive electrobsorption modulator with high power saturation," *J. Appl. Phys.*, vol. 69, no. 27, pp. 4131–4132, 1996.

[156] T. Ido, M. Koizumi, S. Tanaka, M. Suzuki, and H. Inoue, "Polarization and Wavelength Insensitive MQW Electroabsorption Optical Gates for WDM Switching Systems," *IEEE J. Photon. Technol. Lett.*, vol. 8, no. 6, pp. 788–90, 1996.

[157] D.G. Moodie, P.J. Cannard, A.J. Dann, D.D. Marcenac, C.W. Ford, J. Reed, R.T. Moore, J.K. Lucek, and A.D. Ellis, "Low polarization sensitivity electroabsorption modulators for 160 Gbit/s networks," *Electron. Lett.*, vol. 33, no. 24, pp. 2068–2070, 1997.

[158] R.Y.-F. Yip, P. Desjardins, L. Isnard, A. Ait-Ouali, H. Marchand, J.L. Brebner, J.F. Currie, and R.A. Masut, "Band alignment engineering for high speed, low drive field quantum-confined Stark effect devices," *J. Appl. Phys.*, vol. 83, no. 3, pp. 1758–1169, 1998.

[159] S. Morin, B. Deveaud, F. Clerot, K. Fujiwara, and K. Mitsunaga, "Capture of Photoexcited Carriers in a Single Quantum Well with Different Confinement Structures," *IEEE J. Quantum Electron.*, vol. 27, no. 6, pp. 1669–1675, 1991.

[160] B. Deveaud, J. Shah, T. C. Damen, and W. T. Tsang, "Capture of electrons and holes in quantum wells," *Appl. Phys. Lett.*, vol. 52, no. 22, pp. 1886–1888, 1988.

[161] M. Preisel and J. Mørk, "Phonon-mediated carrier capture in quantum well lasers," *J. Appl. Phys.*, vol. 76, no. 3, pp. 1691–1696, 1994.

[162] M. Preisel, J. Mørk, and H. Haug, "Calculations of Coulomb-mediated carrier-capture times," *Phys. Rev. B*, vol. 49, no. 20, pp. 14478–14485, 1994.

[163] Chin-Yi Tsai, L.F. Eastman, Yu-Hwa Lo, and Chin-Yao Tsai, "Carrier Capture and Escape in Multisubband Quantum Well Lasers," *IEEE J. Photon. Technol. Lett.*, vol. 6, no. 9, pp. 1088–90, 1994.

[164] R. Paiella, G. Hunziker, and K.J. Vahala, "Quantum-well capture and interwell transport in semiconductor active layers," *Semicond. Sci. Technol.*, vol. 14, no. 5, pp. R17–25, 1999.

[165] T. Sizer, T.K. Woodward, U. Keller, K. Sauer, T.H. Chiu, D.L. Sivco, and A.Y. Cho, "Measurement of Carrier Escape Rates, Exciton Saturation Intensity, and Saturation Density in Electrically Biased Multiple-Quantum-Well Modulators," *IEEE J. Quantum Electron.*, vol. 30, no. 2, pp. 399–407, 1994.

[166] M. Suzuki, H. Tanaka, and S. Akiba, "Effect of hole pile-up at heterointerface on modulation voltage in GaInAsP Electroabsorption modulators," *Electron. Lett.*, vol. 25, no. 2, pp. 88–89, 1989.

[167] M. K. Chin, S. Niki, H. H. Wieder, and W. S. C. Chang, "Carrier screening of electric field and electroabsorption saturation in InGaAs-GaAs quantum well structure," *Electron. Lett.*, vol. 27, no. 25, pp. 2310–2312, 1991.

[168] J. Feldmann, K.W. Goossen, D.A.B. Miller, A.M. Fox, J.E. Cunningham, and W.Y. Jan, "Fast escape of photocreated carriers out of shallow quantum wells," *Appl. Phys. Lett.*, vol. 59, no. 1, pp. 66–8, 1991.

[169] B. J. Hawdon, T. Tütken, A. Hangleiter, R. W. Glew, and J. E. A. Whiteaway, "Direct comparison of InGaAs/InGaAlAs and InGaAs/InGaAsP quantum well modulators," *Electron. Lett.*, vol. 29, no. 8, pp. 705–707, 1993.

[170] D.J. Moss and H. Sano, "Photoconductivity response times of InGaAs/InAlAs multiquantum well waveguide modulators," *Electron. Lett.*, vol. 29, no. 18, pp. 1626–8, 1993.

[171] T. Yoshida, T. Hoshida, Y. Nasu, M Kishi, and M. Tsuchiya, "Experimental investigation on carrier dynamics in SCH-MQW waveguide saturable absorber of passively mode-locked monolithic laser diode," *Optical and Quantum Electronics*, vol. 33, pp. 735–743, 2001.

[172] H. Haug and S. W. Koch, *Quantum Theory of the Optical and Electronic Properties of Semiconductors*, World Scientific Publishing Co. Pte. Ltd., Singapore, 1990.

[173] J.S. Blakemore, "Approximations for Fermi-Dirac integrals, especially the function $F_{1/2}(\eta)$ used to describe electron density in a semiconductor," *Solid State Electron.*, vol. 25, no. 11, pp. 1067–76, 1982.

[174] H. Hirayama, Y. Miyake, and M. Asada, "Analysis of Current Injection Efficiency of Separate-Confinement-Heterostructure Quantum-Film Lasers," *IEEE J. Quantum Electron.*, vol. 28, no. 1, pp. 68–74, 1992.

[175] Keith J. Williams, Ronald D. Esman, and Mario Dagenais, "Nonlinearities in P-I-N Microwave Photodetectors," *J. Lightwave Technol.*, vol. 14, no. 1, pp. 84–96, 1996.